SEARCH FOR THE LEPTON FLAVOUR VIOLATING DECAY $\tau \to e\gamma$ USING THE *BABAR* DETECTOR

Robert L. Flack

PHYSICS DEPARTMENT

ROYAL HOLLOWAY, UNIVERSITY OF LONDON

A thesis submitted to the University of London
for the Degree of Doctor of Philosophy.
December 2004.

Abstract

A search for the neutrinoless lepton flavour violating decay $\tau \to e\gamma$ was carried out at the Stanford Linear Accelerator Center (SLAC) using $124.4\,\mathrm{fb}^{-1}$ of data provided by the *BABAR* detector coupled with the PEP-II collider. The accelerator produces beams of electrons and positrons that collide to create the $\tau^+\tau^-$-pairs, approximately 111 million, used for the analysis. No evidence was found for the decay $\tau \to e\gamma$ and a preliminary upper limit on the branching ratio of 9.3×10^{-8} at 90% C.L. was obtained. This is two orders of magnitude lower than the previously published limit. The result presented here can be used to constrain certain models such as supersymmetry that predict branching ratios for the decay $\tau \to e\gamma$ that are accessible with the size of the data set available here.

Dedication

This thesis is dedicated to my five most important influences.

My late mother Lillian who from lowly beginings taught me the value of education; I still miss her.

My wife and best friend Valerie whose continued love and support has seen me through difficult times. Never saying ”no don’t” but always ”yes, have a go”, it may seem an innocent comment but when one is about to give up a career to follow a dream it was invaluable.

My children Leanne, Thomas and Charlotte who have all given me joy and happiness in their own way.

Acknowledgments

I would like to thank the following:

My supervisor Glen Cowan for his support and advice during the past three years.

Mike Green for taking a chance when I first approached him to study for a masters degree and allowing me to join the Particle Physics Group at Royal Holloway and supporting my application for a PPARC studentship.

PPARC, without their financial support this thesis would never have happened.

Fabrizio Salvatore who has guided me through the analysis and has also been a good friend.

Jenny Williams for all the hard work in generating the final version of the ntuples that were used in the analysis.

Members of the Tau/QED Analysis Working Group for their helpful discussions and suggestions.

Obviously, there are many more people who contributed in one way or the other to this thesis either by providing help or distraction:

- Jamie for the early morning trips to Cupertino to watch England win the Grand Slam and for many lifts and favours that made life in the US so much easier.
- The guys at Royal Holloway including my fellow *BABAR* students Henning, Clare and Paul.
- I had a great time at SLAC and would like to thank all the ladies in the Housing office especially Barbara without whom my stay would have been quite lonely.
- Ivo, Jong, Helmut and everybody on the EMC who helped through a tough service task.

London, 10 December 2004

Preface

This thesis describes original work undertaken by the author as part of the Tau/QED Analysis Working Group in the *BABAR* collaboration. Whilst on long term attachment to SLAC the author worked closely with a fellow member of the Group, Dr. O. Igonkina, who oversaw the early stages of the analysis.

On returning to the UK the author received help and advice from Dr. G. Cowan. and Dr. F. Salvatore. The technique for estimating the backgrounds was developed in collaboration with them.

The data set contains measurements, not all of which may be required. Therefore data analysis files are produced with a reduced set of the measurements needed for this analysis. Similarly the samples of simulated events are generated in the same format. The final version of the data analysis files used here were produced by Dr. J. Williams.

At this juncture the result reported is preliminary.

Contents

List of Figures

List of Tables

Chapter 1

Introduction

Probing deeper into the atom has radically altered our world view with the discovery of a rich structure of particles and forces expressed in the Standard Model (SM). The SM is now being challenged with evidence that supports, for example, the existence of dark matter and dark energy. Searches are also being undertaken for other particles and processes that would provide evidence of physics beyond the SM; the topic of this thesis is an example. The particle decay $\tau \to e\gamma$ is a paradigm of the neutrinoless lepton decay and processes of this type contravene one of the conservation laws of the SM and are referred to as "lepton flavour violating (LFV) decays".

The most stringent limits on the branching ratio ($\mathcal{B}$) set thus far for LFV decays are for rare μ-decays and are of the order of 10^{-12}, for example the upper limit on the $\mathcal{B}(\mu \to e\gamma)$ [1, 2]. On the other hand searches for the rare τ-decay $\mathcal{B}(\tau \to \mu\gamma)$ have set limits of the order of $< 10^{-7}$ and the most recent published limit for $\tau \to e\gamma$, by the CLEO collaboration, has been set at 2.7 x 10^{-6} [3].

A search for $\tau \to e\gamma$ was carried out at the Stanford Linear Accelerator Center (SLAC) [4] using the *BABAR* detector coupled with the PEP-II collider [5] [6]. The accelerator produces beams of electrons and positrons that collide to create the $\tau^+\tau^-$-pairs required for the analysis; this analysis uses approximately 111 million $\tau^+\tau^-$-pairs.

All members of the *BABAR* collaboration are expected to play a significant part in running the experiment. The author was tasked with being the Commissioner for the Electromagnetic Calorimeter (EMC) for all of the run three of data taking, which began in the Autumn of 2002 and ended in the summer of 2003. A full description of the duties of the Commissioner are given in appendix A.

This chapter proceeds with the definition of LFV within the context of the SM and how neutrinoless decays might occur. An overview of the analysis is presented indicating how the decay $\tau \to e\gamma$ may be discovered. The chapter concludes with a description of each of the chapters of the thesis.

1.1 The SM and searches for LFV

The SM describes Nature as having twelve fundamental particles (Table 2.1) interacting via three forces (Table 2.2). The particles are divided equally into three generations (flavours) of quarks and leptons and are all fermions. It is not known why there are only three generations and no obvious pattern to their masses. The three forces are strong, weak, electromagnetic; the electromagnetic and weak forces have been unified into one electroweak force.

In the SM conservation laws arise out of invariants or symmetries of the system, here the symmetry of interest is the conservation of lepton number. In electroweak processes each generation (flavour) of leptons has a conserved quantum number L_e, L_μ and L_τ. The violation of individual lepton numbers across all three generations, whilst preserving the overall lepton number, $L = L_e + L_\mu + L_\tau$, is called Lepton Flavour Violation (LFV). The SM has incorporated neutrino oscillations and a tree level diagram can be constructed that will allow LFV albeit with a very small branching fraction ($O < 10^{-50}$); thus LFV decays might not be forbidden but heavily suppressed.

Extensions to the SM such as supersymmetry (SUSY) predict the existence of processes that violate the conservation of lepton number and contribute to the branching fractions of LFV decays. These branching fractions can be enhanced to such a degree they may be observable with the size of the data set generated at the *BABAR* experiment. The search for the decay $\tau \to e\gamma$ is just one example of the continuing effort to search for an extension to the Standard Model which would incorporate such a violation and allow neutrinoless lepton decays.

1.2 An overview of the analysis

In the centre of mass frame (CM) $\tau^+\tau^-$-pairs are produced back to back and share the energy of the beam equally. First $\tau^+\tau^-$-pairs are identified by the topology of the event, specifically the number of charged particles; which is always even. Then two hemispheres can be defined, one hemisphere must contain evidence of a SM τ-decay, the other the electron plus the photon making the $e\gamma$-signal of the $\tau \rightarrow e\gamma$ decay.

The collider produces other types of event that will form a background to the $e\gamma$-signal and a selection process is used to reduce their number. In the τ-decay, the invariant mass and total energy of the electron plus the photon must equal the τ-mass and the energy of the beam respectively. These constraints are used to distinguish the $e\gamma$-signal from the background.

1.3 Organisation of the Thesis

The thesis proceeds in Chapter 2 by discussing the minimal SM with massless neutrinos and how it forbids LFV decays. The recent confirmation of neutrino oscillations implies that neutrinos have mass and therefore should allow mixing of neutrino flavours and non-conservation of the lepton quantum number. The phenomenon of neutrino oscillations is described in some detail and it is shown that it predicts a highly suppressed branching fraction for LFV decays. The seesaw mechanism, with the introduction of a heavy right-handed neutrino, has become the favoured method for explaining the lightness of the mass of the neutrino. It is then shown how using this mechanism and the associated neutrino mixing can enhance the branching ratio for the decay $\tau \rightarrow e\gamma$. Extensions to the SM such as supersymmetry can enhance the branching fraction for LFV decays by many orders of magnitude especially the supersymmetric seesaw mechanism; these are presented along with the proposed tree level diagrams of these processes.

Chapter 3 describes the PEP-II collider and the *BABAR* detector. The e^+e^- collisions produce quark and lepton pairs of all flavours, except the top quark, which includes the pairs of τ-leptons required for this analysis. Each event must be fully reconstructed to facilitate the discrimination between the different types; thus the detector must be capable of making very precise measurements. Each of the subsystems of the detector is described emphasising how it meets the needs of this analysis and also how they work together to collect the data. This chapter concludes with a description of the data set used for this analysis.

Chapter 4 discusses the strategy of the analysis. Using the topology of the $\tau^+\tau^-$-pairs to distinguish them from the other types of event produced by the collider has implications for the percentage of the data that can be used for the analysis. The characteristics of the $e\gamma$-signal and the two-body decay model used to simulate $\tau \rightarrow e\gamma$ is described. An overview of the method used to distinguish $\tau \rightarrow e\gamma$ from known τ-decay modes and other backgrounds, especially those that can mimic the $e\gamma$-signal, is then presented. The backgrounds that can closely simulate the $e\gamma$-signal require a set of selection criteria that have been specifically designed to remove them.

The analysis is then described and discussed in detail and begins with the reduction of the data set and the event selection. The procedure for selecting events has two stages: the first is a preselection which uses a set of general criteria to aid discrimination of $\tau^+\tau^-$-decays from other types of event; the second is a set of well defined, optimised cuts on the data. This process reduces the number of background events whilst enhancing any potential signal.

Chapter 5 describes how an accurate estimate is made of the number of background events remaining after all of the cuts have been applied. Then the statistical and systematic errors on this estimate are calculated. A blind analysis method has been followed and at this stage the full data set is inspected for any sign of signal events. No evidence was found for the neutrinoless decay $\tau \rightarrow e\gamma$ and therefore an upper limit was placed on the branching fraction.

There are a number of ways upper limits can be set and these are discussed in Chapter 6. Finally the upper limit on the branching fraction is reported and the implications of this result are discussed.

Chapter 2

Theoretical models of neutrinoless lepton decays

The minimal Standard Model has massless neutrinos and one light, neutral Higgs; in this version of the SM lepton flavour violation (LFV) is forbidden. The phenomenon of neutrino oscillation, which implies neutrinos have mass, predicts that LFV is no longer forbidden but heavily suppressed. This is true if the masses are of Dirac or Majorana type. Extensions to the minimal SM such as supersymmetry (SUSY) can increase the branching fraction ($\mathcal{B}$) for $\tau \to e\gamma$ predicted by neutrino oscillation by many orders of magnitude. Therefore the discovery of this decay mode not only exhibits new physics but could be evidence of the existence of SUSY.

This chapter begins with an overview of the Standard Model with special reference to the conservation of the lepton quantum number. The experiments at Sudbury Neutrino Observatory (SNO Collaboration) and the Super-Kamiokande Collaboration that confirmed neutrino oscillations are considered and the way this phenomenon allows LFV is explained. Then a brief outline of SUSY and how it can enhance the rate for LFV processes follows. Finally the chapter concludes with a summary of the enhanced limits.

2.1 The Standard Model

The Standard Model is a gauge theory of quarks and leptons (Table 2.1) that interact via three fundamental forces (Table 2.2) strong, electromagnetic and weak. These are described by the symmetry group $SU(3)_{\mathrm{C}} \otimes SU(2)_{\mathrm{L}} \otimes U(1)_{\mathrm{Y}}$. The group $SU(3)_{\mathrm{C}}$ describes the colour symmetry (C refers to colour), $SU(2)_{\mathrm{L}}$ the weak isospin symmetry (L refers to the left-handed component of the three weak currents) and $U(1)_{\mathrm{Y}}$ the weak hypercharge (Y refers to hypercharge). The SM does not include gravity which is very weak at the energies of high energy physics (HEP) experiments; some extensions to the SM propose the graviton as the carrier of the force but it has yet to be observed.

In the Lagrangian formalism of the field theory description of the Standard Model the Lagrangian has three parts,

$$\mathcal{L}_{\mathrm{SM}} = \mathcal{L}_{\mathrm{gauge}} + \mathcal{L}_{\mathrm{Higgs}} + \mathcal{L}_{\mathrm{Yukawa}}. \tag{2.1}$$

Here $\mathcal{L}_{\mathrm{gauge}}$ describes the gauge fields of the three forces, $\mathcal{L}_{\mathrm{Higgs}}$ is the Lagrangian for the Higgs fields and $\mathcal{L}_{\mathrm{Yukawa}}$ generates the mass terms for the quarks and fermions.

Table 2.1: The table shows the constituent particles of the SM divided into leptons and quarks in the order of the three generations. Their charges and masses [7] are given.

	Leptons		Quarks	
1st generation	e	ν_e	u	d
Mass(keV/c^2)	511	$<$ 0.003	1500 to 4000	4000 to 8000
Charge	-1	0	$+2/3$	$-1/3$
2nd generation	μ	ν_μ	c	s
Mass(MeV/c^2)	105.658	$<$ 0.19	1150 to 1350	80 to 130
Charge	-1	0	$+2/3$	$-1/3$
3rd generation	τ	ν_τ	t	b
Mass(GeV/c^2)	1.777	$<$ 0.018	174.3 $\pm$ 5.1	4.1 to 4.4
Charge	-1	0	$+2/3$	$-1/3$

The leptons can exist in isolation whereas the quarks cannot; they can only exist in colour neutral states. At the present time there is only firm observation of two types of bound state for quarks, mesons ($q\ \overline{q}$ pairs) and baryons (quark triplets); there have been searches for other bound states such as the penta-quark and glueball. For each particle there exists an antiparticle with the same mass. The electric charge carried by the antiparticles has the same magnitude as their matter counterparts but is of opposite sign.

Table 2.2: The table gives the force carriers in the SM and that proposed for gravity.

	Carrier Particle	Electric Charge	Mass (GeV/c^2
Strong	gluon	0	0
Electroweak	W^+	$+1$	80.419
	W^-	-1	80.419
	Z	0	91.188
	Photon	0	0
Gravity	Graviton	0	0

Leaving gravity to one side the carriers of the other three forces are gauge bosons. The quarks can interact with all of the other particles via all of the forces; this is not the case for the leptons. Charged leptons cannot interact via the strong force but only via the electromagnetic and weak forces (electroweak). Neutrinos, by the virtue of not being electrically charged, can only interact via the weak force. One of the peculiarities of neutrinos is that only those with left-handed helicity have been observed with the corresponding right-handed antineutrino.

In the Standard Model, mixing of the left-handed d, s and b quarks at the charged W vertex is accomplished through the Cabibbo-Kobayashi-Maskawa (CKM) matrix [8] [9]. In the minimal SM with massless neutrinos there is no analogous flavour mixing amongst the leptons; the mass eigenstates of the charged leptons can be obtained by a rotation of the whole lepton doublet ($\nu_{\rm L}$, $e_{\rm L}$). Therefore lepton numbers (L_e, L_μ and L_τ) can be defined separately for each generation and are conserved; the values of L_e, L_μ and L_τ for each lepton are $+1$ and for each antilepton -1.

The Standard Model has successfully encompassed neutrino oscillations and the implication that the neutrinos have mass. This is the first step away from the minimal SM and will be discussed in the next section followed by a brief overview of a more radical extension by supersymmetry.

2.2 LFV via neutrino oscillation

Evidence for neutrino oscillation comes from two types of experiment: measurements of the flux of solar neutrinos and measurements on the relative fluxes of atmospheric electron and muon neutrinos. The solar neutrino problem gave the first indication that neutrinos may oscillate between their different flavours on their journey to Earth from the interior of the Sun. The fusion process operating in the Sun produces electron neutrinos. Measurements of the flux of the solar neutrinos has shown a discrepancy with the rate predicted by the standard solar model [10]. An experiment at SNO [11] has shown that the deficit in the number of solar neutrinos could be accounted for by converting some of the electron neutrinos to muon and tau neutrinos. The theory of neutrino oscillations can explain the conversion of neutrinos between different flavours.

The relative number of neutrinos generated by the interaction of cosmic rays with the atmosphere at short and large distances from the detector have been measured at Super-Kamiokande [12]. A difference between the number of muon neutrinos arriving from the far side of the Earth compared to those originating from the atmosphere overhead has been reported and is consistent with the idea of neutrino oscillation; specifically the oscillation of muon neutrinos to tau neutrinos.

Currently the three generations of left-handed neutrinos are considered to have a corresponding set of three right-handed antineutrinos. One of the preferred solutions to the problem of neutrino mixing is to extend the neutrino sector and include neutrinos that behave like a Majorana particle. As the neutrinos, by definition, do not carry charge raises the interesting question whether it has an antiparticle and is therefore a Dirac particle or is its own antiparticle, a Majorana particle. For example an electron is negatively charged and can have both left and right helicities, whereas the positron is positively charged with the same mass and can also have left and right helicities. The helicity is defined as the direction of the spin of the particle along its line of motion. The neutrino could be similar to the electron (Dirac particle) having left and right helicities and unique separate antiparticles, or on the other hand it could have only a left-handed helicity state and what is at present referred to as an antineutrino with a right-handed helicity state is in fact a just right-handed neutrino (Majorana particle); this is illustrated in Table 2.3. In the Lagrangian formalism, a typical Dirac term would be $m_{\mathrm{D}}\bar{\phi}\phi$ where

$\phi = (e^-,\, e^+) = (e^c,\, e),\; c =$ charge conjugation and corresponds to two particles. On the other hand a typical Majorana term would be $\frac{M}{2}\bar{\phi}\phi$ where $\phi = (\bar{\nu},\, \nu)$, $\bar{\phi} = \phi^{\mathrm{T}} C = \exp^{i\psi}$, $C =$ the charge conjugation operation and ψ is an arbitrary phase.

Table 2.3: Summary of the difference between a Dirac and a Majorana particle using the electron and the neutrino as examples.

Dirac		Majorana	
$\mathrm{e}_{\mathrm{L}}^{-}$	$\mathrm{e}_{\mathrm{R}}^{-}$		
$\mathrm{e}_{\mathrm{L}}^{+}$	$\mathrm{e}_{\mathrm{R}}^{+}$		
ν_{L}	ν_{R}	ν_{L}	
$\overline{\nu}_{\mathrm{L}}$	$\overline{\nu}_{\mathrm{R}}$		ν_{R}

One of the consequences of neutrino oscillations is the introduction of neutrino masses and the proposal of neutrino flavour mixing. Let the flavour eigenstates be ν_{e_i}, $i = 1,\, 2,\, 3$, where $\nu_{e_1} = \nu_e$, $\nu_{e_2} = \nu_\mu$ and $\nu_{e_3} = \nu_\tau$. Correspondingly let the mass eigenstates be ν_h, $h = 1,\, 2,\, 3$. A unitary transformation rotates the flavour states into the mass states thus,

$$\nu_{e_i} = U_{ih}\nu_h, \tag{2.2}$$

and

$$\bar{\nu}_{e_i} = U^*_{ih}\bar{\nu}_h \tag{2.3}$$

(2.4)

where U_{ih} is called the Pontecorvo, Maki, Nakagawa, Sakata (PMNS) matrix [13] or the neutrino mixing matrix. The time evolution of the ν_i state vector [14] is then described by,

$$e^{iHt}\nu_i = U_{ih}e^{iE_h}\nu_h \tag{2.5}$$

where the energy E_h is given by,

$$E_h = \sqrt{p^2 + m_h^2} \approx p + \frac{m_h^2}{2E}. \tag{2.6}$$

Here p is the momentum and m_h is the mass of the neutrino.

The standard parameterisation of U_{ih} [15] is,

$$U = \begin{pmatrix} \cos\theta_{12} & \sin\theta_{12} & 0 \\ -\sin\theta_{12} & \cos\theta_{12} & 0 \\ 0 & 0 & 1 \end{pmatrix} \begin{pmatrix} \cos\theta_{13} & 0 & \sin\theta_{13} e^{-i\delta} \\ 0 & 1 & 0 \\ -\sin\theta_{13} e^{-i\delta} & 0 & \cos\theta_{13} \end{pmatrix} \begin{pmatrix} 1 & 0 & 0 \\ 0 & \cos\theta_{23} & \sin\theta_{23} \\ 0 & -\sin\theta_{23} & \cos\theta_{23} \end{pmatrix} \tag{2.7}$$

where $0 < \theta_{12}\,\theta_{13}\,\theta_{23} < \pi/2$ and $0 < \delta < 2\pi$. The data from neutrino experiments [12] [11] [16] [17] [18] [19] indicate that $\theta_{23} < 45°$, $\theta_{12} < 35°$ and $\theta_{13} < 10°$.

In the simplest case [20] where,

$$\nu_e = \nu_1 \cos\theta + \nu_2 \sin\theta \tag{2.8}$$

and

$$\nu_\mu = -\nu_1 \sin\theta + \nu_2 \cos\theta \tag{2.9}$$

then

$$P(\nu_e \to \nu_\mu) = \sin^2 2\theta \sin^2 \frac{\Delta m^2 L}{4E} \tag{2.10}$$

Therefore the probability of the transformation from one neutrino flavour to another depends on θ and Δm^2. It should be noted that this does not give information about the absolute values of the neutrino masses but only about their differences. This leads to three possibilities that the masses follow (i) hierarchy of the charged leptons $m_1 < m_2 << m_3$, (ii) they are inverted $m_2 = m_1 >> m_3$ or (iii) they are degenerate $m_1 = m_2 = m_3$.

The favoured method for explaining the lightness of the neutrino masses is through the seesaw mechanism [21] [22]. The seesaw mechanism relates the light neutrino masses to a heavy right-handed Majorana neutrino M by adding a term $\mathcal{L}_{\nu\text{mass}}$ [23] to equation 2.1, which contains two distinct types of neutrino mass terms m_{D} (Dirac) and M_{R} (Majorana),

$$\mathcal{L}_{\nu\mathrm{mass}} = -\frac{1}{2}\nu_{\mathrm{R}}^{c} M_{\mathrm{R}} \nu_{\mathrm{R}} - \bar{\nu}_{\mathrm{L}} m_{\mathrm{D}} \nu_{\mathrm{R}} + \text{h.c.} \tag{2.11}$$

Here in general $\nu^c = -\nu^{\mathrm{T}} C^{-1}$ (C is the charge-conjugation matrix), T is transpose and L and R denote left and right respectively.

$\mathcal{L}_{\nu\mathrm{mass}}$ can be shown to become [24],

$$\mathcal{L}_{\nu\mathrm{mass}} = -\frac{1}{2}\begin{pmatrix} \bar{\nu}_{\mathrm{L}} & \nu_{\mathrm{R}}^{c} \end{pmatrix} \mathcal{M} \begin{pmatrix} \nu_{\mathrm{L}} \\ \nu_{\mathrm{R}} \end{pmatrix} + \text{h.c.} \tag{2.12}$$

where,

$$\mathcal{M} = \begin{pmatrix} 0 & m_{\mathrm{D}}^{\mathrm{T}} \\ m_{\mathrm{D}} & M_{\mathrm{R}} \end{pmatrix} \tag{2.13}$$

The seesaw matrix can be diagonalised by the unitary transformation,

$$\begin{pmatrix} V & R \\ S & U \end{pmatrix}^{\dagger} \begin{pmatrix} 0 & m_{\mathrm{D}}^{\mathrm{T}} \\ m_{\mathrm{D}} & M_{\mathrm{R}} \end{pmatrix} \begin{pmatrix} V & R \\ S & U \end{pmatrix}^{*} = \begin{pmatrix} m_{\nu\mathrm{mass}} & 0 \\ 0 & M_{\mathrm{Rmass}} \end{pmatrix} \tag{2.14}$$

where $m_{\nu\mathrm{mass}}$ and M_{Rmass} are the diagonalised 3×3 mass matrices with the eigenvalues m_i and M_i respectively. The matrix U is defined in equation 2.7 and the matrix V is defined as,

$$V = U \begin{pmatrix} e^{i\alpha} & 0 & 0 \\ 0 & e^{i\beta} & 0 \\ 0 & 0 & 1 \end{pmatrix} \tag{2.15}$$

where α and β are phases. When the Majorana mass scale is much larger than the Dirac mass scale (mass hierarchy) then the matrices R and S are of the order $m_{\mathrm{D}}/M_{\mathrm{R}}$ [20]. Then equation 2.14 reduces to,

$$V m_{\nu\mathrm{mass}} V^{\mathrm{T}} \approx m_{\mathrm{D}}^{\mathrm{T}} (M_{\mathrm{R}})^{-1} m_{\mathrm{D}}. \tag{2.16}$$

and

$$U M_{\mathrm{Rmass}} U^{\mathrm{T}} \approx M_{\mathrm{R}}. \tag{2.17}$$

The three light and three heavy neutrino masses are:

$$m_1^2/M_1,\ m_2^2/M_2,\ m_3^2/M_3,\ M_1,\ M_2,\ M_3. \tag{2.18}$$

As an example of how this gives the mass of the three light neutrinos assume the values of the elements of M_{R} and m_{D} are of the order of $O(10^{15})$ GeV and $O(10^2)$ GeV respectively. Then the ratios $m_1^2/M_1, m_2^2/M_2, m_3^2/M_3$ will be of the order of $O(10^{-2})$ eV.

The transformation of the seesaw matrix can be completely defined with nine free parameters: the three mixing angles $\theta_{12},\ \theta_{13},\ \theta_{23}$ and phase δ in defining the matrix U, two phases α and β in defining the matrix V and three phases from the charge conjugation $\psi_1,\ \psi_2,\ \psi_3$.

Diagonalisation of the charged lepton and neutrino mass matrices induces lepton flavour mixing in the charged weak current interaction in a similar way to quarks. Using the first two generations as an example the terms in the mixing matrix for quarks are $\sin\theta$ and $\cos\theta$ where θ is approximately 13° [25]. For neutrino mixing the situation is more complex and the mixing angle θ^{lept} has three components, as can be seen in the PNMS matrix. and can be written in the form,

$$\theta^{\mathrm{lept}} = \theta_{\mathrm{L}}^{\mathrm{D}} - \theta_{\mathrm{L}}^{l} + \theta_{\mathrm{ss}}. \tag{2.19}$$

The first two terms on the right-hand side are the direct analogies of the mixing angle in the quark sector. The first, $\theta_{\mathrm{L}}^{\mathrm{D}}$ is the angle of rotation of the left-handed neutrino components ν_{L} and diagonalises the Dirac mass matrix m_{D}. The second, θ_{L}^{l} is the angle of rotation of the left-handed charged lepton components and diagonalises the mass matrix of charged leptons. The third term of the right-hand side θ_{ss} is the additional angle, the seesaw angle, that specifies the effect of the seesaw mechanism. If $\theta_{\mathrm{L}}^{\mathrm{D}} - \theta^{l}$ is of a similar order to the Cabibbo angle then it can be shown that θ_{ss} may be close to 45° [23] as indicated by the data.

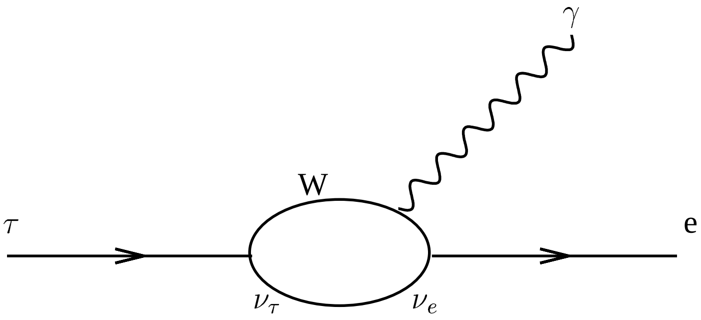

Figure 2.1: A neutrinoless decay due to the mechanism of neutrino oscillation. In the decay mode $\tau \to e\gamma$ the τ-vertex has a τ-neutrino and a W-Boson, the τ-neutrino oscillates to an electron-neutrino and the W-Boson radiates a photon. The electron-neutrino and the W-Boson form a second vertex to create an electron without any neutrinos. The W-Boson has to radiate a photon so that the invariant mass of the electron and the photon will equal the τ-mass.

Once neutrino mixing is allowed then it is possible to draw Feynman diagrams such as Fig. 4.1 which shows how LFV may come about. In the decay mode $\tau \to e\gamma$ the τ-vertex has a τ-neutrino and a W-Boson, the τ-neutrino oscillates to an electron-neutrino and the W-Boson radiates a photon. The electron-neutrino and the W-Boson form a second vertex to create an electron without any neutrinos. The W-Boson has to radiate a photon so that the invariant mass of the electron and the photon will equal the τ-mass. The predicted branching ratio for LFV processes of this type assuming small neutrino masses and mixing is given by [26] [27]

$$\mathcal{B}(\tau \to e\gamma) = \frac{3\alpha}{32\pi} | \sum_i (V_{PMNS})^*_{\tau i} (V_{PMNS})_{ei} \frac{m^2_{\nu_i}}{m^2_W} |^2. \tag{2.20}$$

This is dominated by the term $(m_\nu/m_{\rm W})^4$, where m_ν the neutrino mass, and $m_{\rm W}$ is the mass of the W. The branching ratio for this kind of process is estimated to be of the order of $< 10^{-47}$ [24] which is far below the level observable by any conceivable experiment.

If the mass matrix is of the seesaw type and includes Dirac and a heavy Majorana neutrinos, then the suppression factor $(m_\nu/m_{\rm W})^4$ is replaced with a factor of the order of $O(m_\nu/M_{\rm R})$ [28] where $M_{\rm R}$ is the mass of the heavy Majorana neutrino. If m_ν is of the order $< 1\,eV$ as before, and $M_{\rm R}$ is of the order of $O(10^{10}\,{\rm GeV})$ then the branching ratio is now many orders of magnitude higher at $O(10^{-40})$.

Although neutrino oscillations and lepton mixing predict the existence of LFV processes the resulting branching ratios are much smaller than can be observed. Extending the SM to include supersymmetry can produce flavour violating processes amongst the superparticles and can enhance the branching ratios. This will be discussed next.

2.3 LFV via supersymmetry

A new symmetry of nature called supersymmetry proposes that every elementary particle has a supersymmetric partner which are the same except for their spin, i.e. a symmetry between fermions and bosons where each fermion of the Standard Model would have a SUSY partner, a boson, and vice-versa. The most commonly quoted version is called the “Minimal SuperSymmetric Model” (MSSM). A summary of the particles and their SUSY partners for the MSSM are given in Table 2.3. The superpartners for the quarks and leptons are called squarks and sleptons, respectively. The superpartner of the gauge boson is a gauge fermion, a gaugino, and for the Higgs a Higgsino. The superpartners of the gluon, $SU(2)$ and $U(1)$ gauge bosons are the gluino , the wino and the bino respectively. After electroweak symmetry breaking, the wino, bino and the Higgsino mix with each other and form two charged Dirac fermions called charginos, $\chi^{\pm}_{1,2}$ and four Majorana fermions called neutralinos, $\chi^{0}_{1,2,3,4}$ [29]. The Higgs sector is increased to five physical Higgs plus their super-partners the Higgsinos. The five new Higgs particles are:

- 2 scalar (CP even) particles h^0, H^0;
- 1 pseudo-scalar (CP odd) neutral A^0;
- 2 charged scalars H^+, H^-.

SUSY particles have not been observed at the low mass scales therefore it is thought they must be in the unexplored regions at higher mass scales. If this is the case the symmetry cannot be exact as their masses are thus different from those of their SM partners.

Extensions to the Standard Model such as SUSY can enhance the branching fractions of LFV decays only when the neutrinos have mass. Indeed supersymmetric models with massless neutrinos lead to similar predictions as to those found for the SM with massive (Majorana or Dirac) neutrinos [30] [31] [32].

Table 2.4: The particles prescribed by the SM and their supersymmetric partners in the MSSM.

particle	spin	sparticle	symbol	spin
quark	$1/2$	squark	$\tilde{q}$	0
lepton	$1/2$	slepton	$\tilde{l}$	0
photon	1	photino	$\tilde{\gamma}$	$1/2$
gluon	1	gluino	$\tilde{\gamma}$	$1/2$
$W^{\pm}$	1	wino	$\tilde{W}^{\pm}$	$1/2$
Z^0	1	zino	$\tilde{Z}^0$	$1/2$

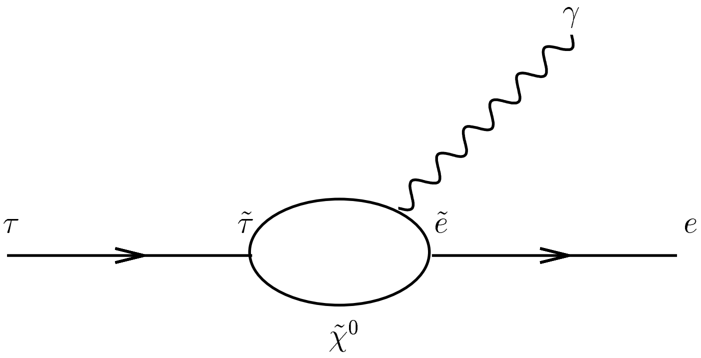

Figure 2.2: An example of a LFV supersymmetric decay induced by charged slepton flavour mixing. A tau-lepton decaying via a chargino and mixing charged sleptons.

In the SUSY models there is a new source of flavour mixing in the mass matrices of the SUSY partners for leptons and quarks; i.e. sleptons and squarks. This will induce LFV processes for the charged leptons such as $\tau^+(\tau^-) \rightarrow \tilde{l}^+(\tilde{l}^-) \rightarrow e^+\tilde{\chi}_1^0(e^-\tilde{\chi}_1^0)$ (Fig.2.2) [24]. If sneutrinos can oscillate as their SM partners then another possibility is given in Fig. 2.3. The branching ratios depend on the flavour mixing in the slepton mass matrix. The predictions for the $\mathcal{B}(\tau \rightarrow e\gamma)$ and similar decays such as $\mu \rightarrow e\gamma$ are only one or two orders of magnitude lower than the present experimental limits presented in the introduction to this chapter [33–35].

When the seesaw mechanism is extended by supersymmetry [36] the lepton term in the superpotential has an extra term added that describes the heavy neutrinos. Therefore there are now two Yukawa couplings, one for the extended lepton sector which now includes the sleptons and the second for the heavy neutrinos. As a consequence of SUSY doubling the number of particles in the lepton sector the mixing matrix now requires 18

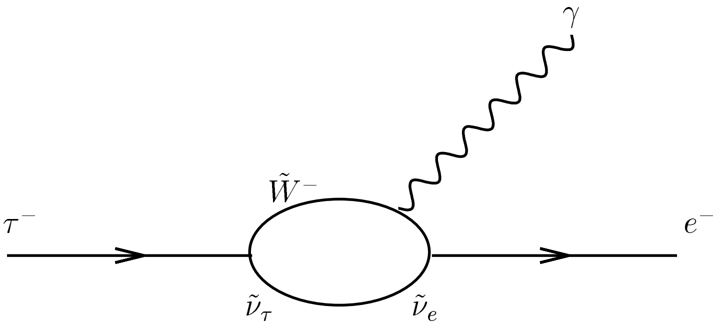

Figure 2.3: An example of a supersymmetric decay that violates lepton number conservation. A tau-lepton decaying via a charged wino and mixing sneutrinos.

free parameters instead of the previous nine needed for the light neutrino mixing. Therefore nine additional degrees of freedom are required to fully parameterise the seesaw mechanism in the MSSM.

J. Ellis et al. [37] have presented a model where an extra Hermitian matrix H is added to the seesaw matrix $\mathcal{M}$ defined in equation 2.13. Therefore the seesaw sector is now characterised by two matrices, whose diagonal terms are real and positive. The Hermitian matrix is defined as,

$$H = Y_\nu^2 log \frac{M_G}{M_R} \tag{2.21}$$

where Y_ν is the heavy-singlet neutrino Dirac Yukawa coupling and M_G is the GUT scale. The matrix H has nine parameters which, combined with the nine from the light neutrino seesaw matrix, makes up the 18 required to completely parametrise the supersymmetric extended seesaw matrix. The parameters to calculate the the branching ratio $\mathcal{B}(\tau \to e\gamma)$ are determined assuming either a normal or inverted hierarchy for the light neutrino mass spectrum, a range of stau masses from zero to 1 TeV, a gaugino mass of 200 GeV, $A_0 = 0$ and $\tan\beta = 10$ and 30. The branching ratios reported are of the order of $O(10^{-4})$ and $O(10^{-5})$ for tan$\beta = 30$ and 10 respectively which is a significant enhancement on the $\mathcal{B}(\tau \to e\gamma)$ calculated using other models. As these have already been constrained by existing experimental limits lower values of $\tan\beta$ will have to be used for further reduction.

The branching ratio scales as $tan^2\beta$. Therefore this implies that for a limit of $O(10^{-6})$, the present experimental limit set by the CLEO collaboration, the value of $\tan\beta$ is lowered to approximately three.

Therefore using the neutrino masses and mixing indicated by the atmospheric and solar neutrinos in combination with the seesaw mechanism and supersymmetry could make LFV decay modes observable with the *BABAR* data set.

2.4 Summary

Models have been presented that enhance the branching ratio for LFV τ-decays relative to those calculated for the SM. The amount of enhancement depends on the model. The highest predicted rates from the model of J. Ellis et al are already in conflict with existing measurements. A summary of the predicted branching ratios for LFV decays for various theoretical models is given in Table 2.4.

Table 2.5: A summary of the order of magnitudes of the branching ratios for rare LFV decays predicted by the observed phenomenon of neutrino oscillation and for various theoretical models.

Model	Branching Fraction	Reference
Neutrino Oscillation	$< 10^{-47}$	[24]
Seesaw model	$< 10^{-40}$	[24]
MSSM	$10^{-8} \rightarrow 10^{-10}$	[33, 34, 38]
Ellis et al	$< 10^{-4}$ ($< 10^{-5}$)	[37]

The enhancements in the rate of $\tau \rightarrow e\gamma$ predicted by theories beyond the SM make discovery of this decay possible with the size of the data set made available by the combination of the PEP-II collider and the *BABAR* detector. This will be discussed in the next chapter.

Chapter 3

The *BABAR* experiment at the PEP-II collider

The main purpose of the *BABAR* experiment is the study of CP violation and measurement of elements in the CKM matrix such as $|V_{ub}|$and $|V_{cb}|$; other studies are also carried out and the search for LFV processes is but one example. To separate all of the generated events into the various categories required by the diverse set of researchers within the *BABAR* collaboration demands a highly complex, flexible detector and a large data set. The multi-component high precision *BABAR* detector [39] [40] (Fig. 3.1) coupled with the large integrated luminosity provided by the PEP-II Collider (Fig. 3.2) were designed to satisfy these criteria.

3.1 The PEP-II collider

PEP-II operates at the Stanford Linear Accelerator Center (SLAC) and is principally a high luminosity B Factory, bringing electron and positron beams into collision at the $\Upsilon(4S)$ resonance (10.58 GeV), in the centre of mass frame (CM), for the production of B^- B^+ and B^0 $\overline{B}^0$ pairs (Fig. 3.3); simultaneously τ-pairs and other processes are also produced.

Measurement of the CP violation parameters requires the energy of the beams be asymmetric and the electrons and positrons are accelerated to 9.0 GeV and 3.1 GeV respectively resulting in a Lorentz boost to the $\Upsilon(4S)$ resonance of $\beta\gamma =$ 0.56. To illustrate the need for the asymmetry consider the decay of the $\Upsilon(4S)$ resonance to a pair of neu-

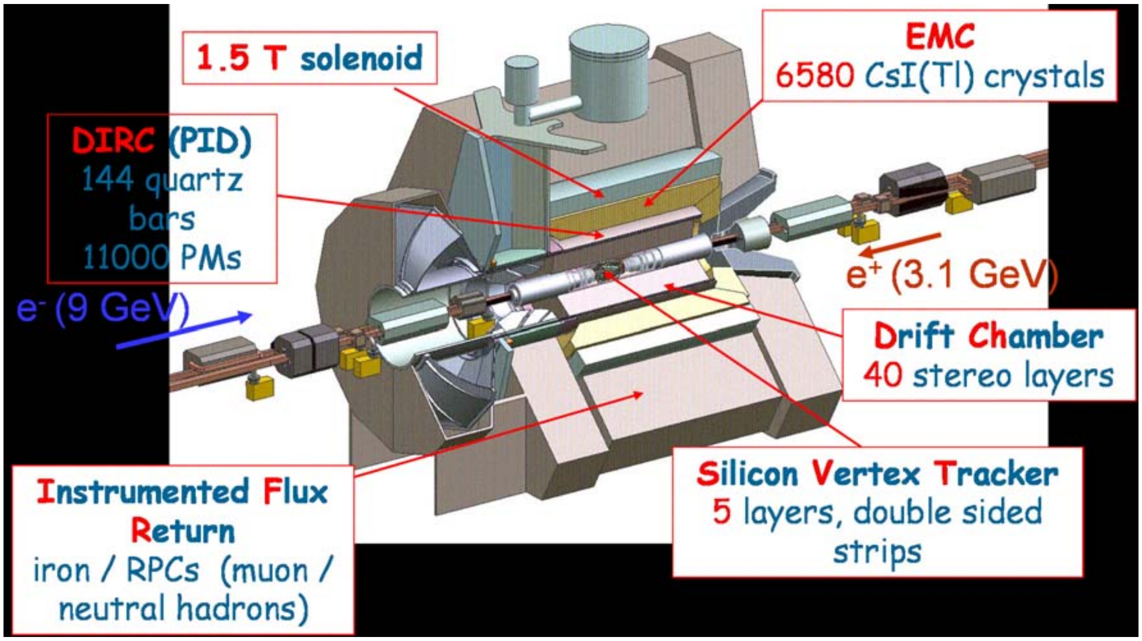

Figure 3.1: A cutaway three dimensional overview of the *BABAR* detector showing all of its subsystems and their relative positions with respect to the point of interaction between the electron and positron beams.

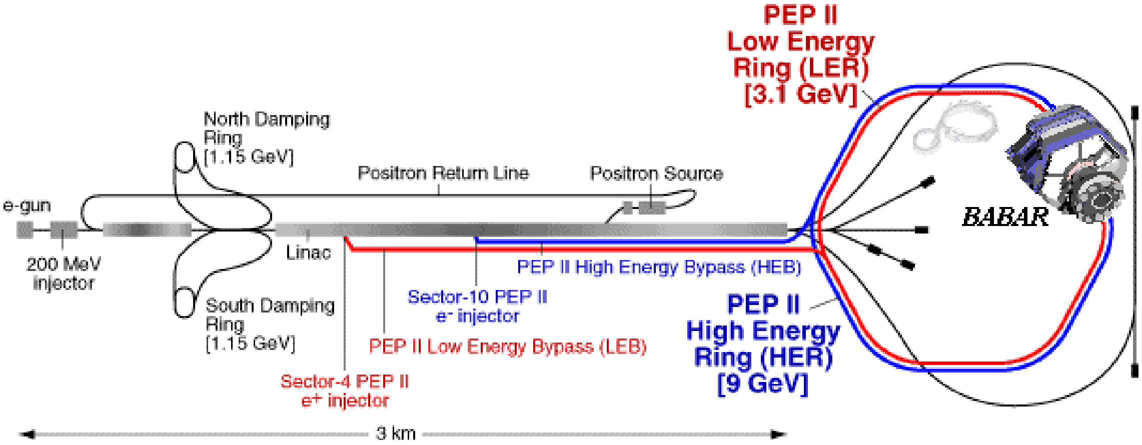

Figure 3.2: The PEP-II collider [5]

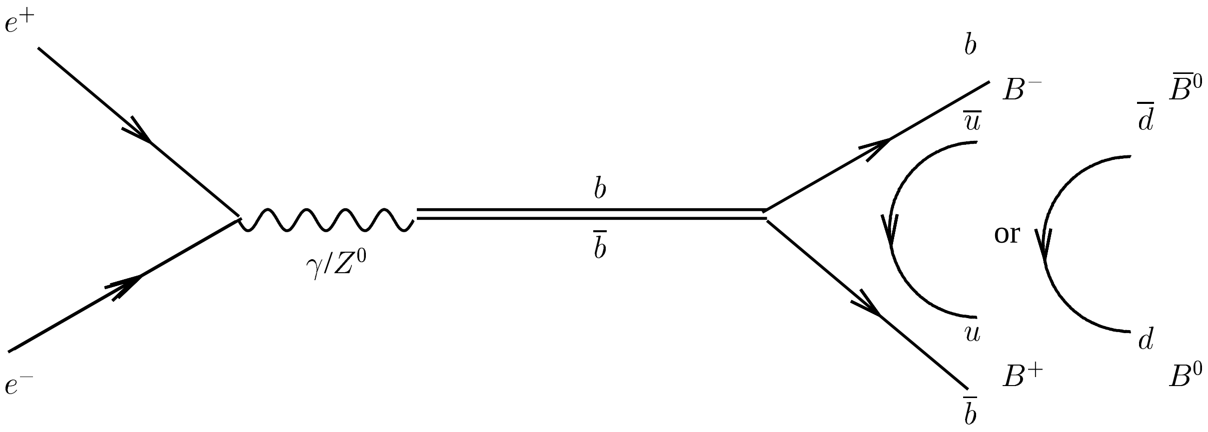

Figure 3.3: A typical production event of B^-, B^+ and $\overline{B}^0$, B^0 pairs at the $\Upsilon(4S)$ resonance.

tral B-mesons. These will decay at different times and therefore their respective decay vertices will be displaced from the IP by differing amounts. The key variable is the time between the two decays and this is proportional to the distance, Δz, between the vertices measured along the z-axis. If the energies of the beams were symmetric then the position of the IP would need to be known very precisely (Fig. 3.4a) to be able to measure $\Delta z = |z_1 - z_2|$. An asymmetric configuration allows Δz to be measured directly without reference to the IP (Fig. 3.4b).

The beams are held in two storage rings, the high energy (HER) and the low energy (LER) before being brought to a collision at the interaction point (IP) in the *BABAR* detector. The parameters of the PEP-II storage rings are given in Table 3.1 showing the values of the original design and those achieved in the first and fourth year of operation. In the fourth year the number of bunches of beam particles stored in the rings at any one time was raised. Another improvement was the introduction of trickle injection. Data taking had to stop when new bunches of beam particles were injected into the storage rings; this was referred to as topping-off. The method of trickle injection allows new bunches to be introduced into the rings continuously at a rate of up to 10 bunches per second without the need to interrupt data taking. These upgrades have radically increased the luminosity.

PEP-II operations carries out fast monitoring of the relative luminosity by measuring radiative Bhabha scattering. The absolute luminosity is derived by the *BABAR* experiment offline by using other QED processes, primarily e^+e^- and $\mu^+\mu^-$ pairs, whose rates of production are consistent and stable as a function of time. For a data sample of $1\,\mathrm{fb}^{-1}$, the statistical error is less than 1%. The systematic uncertainty on the relative changes

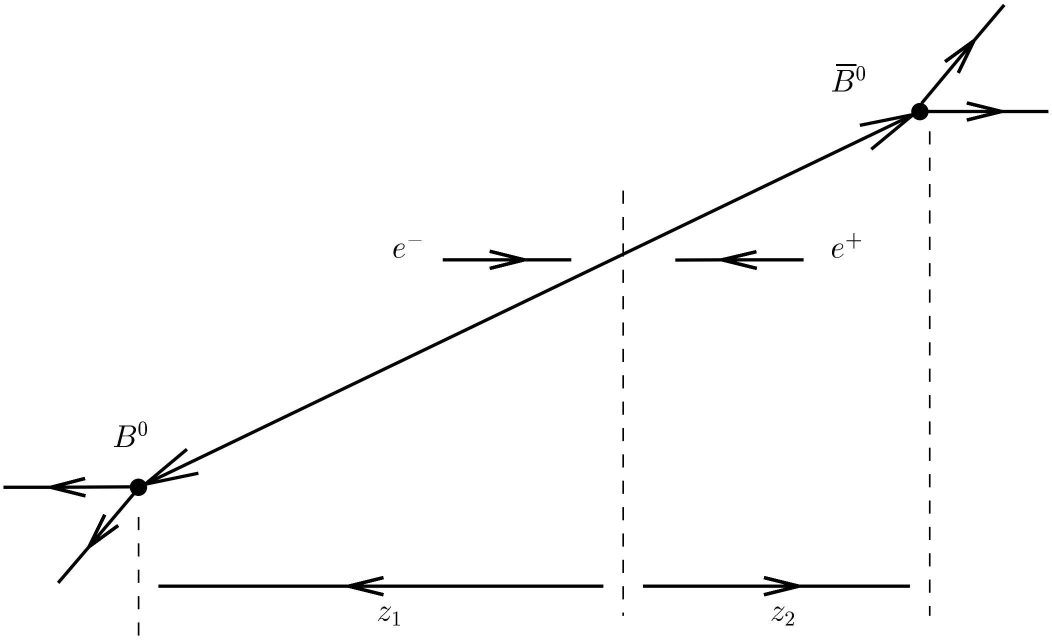

(a) symmetric configuration

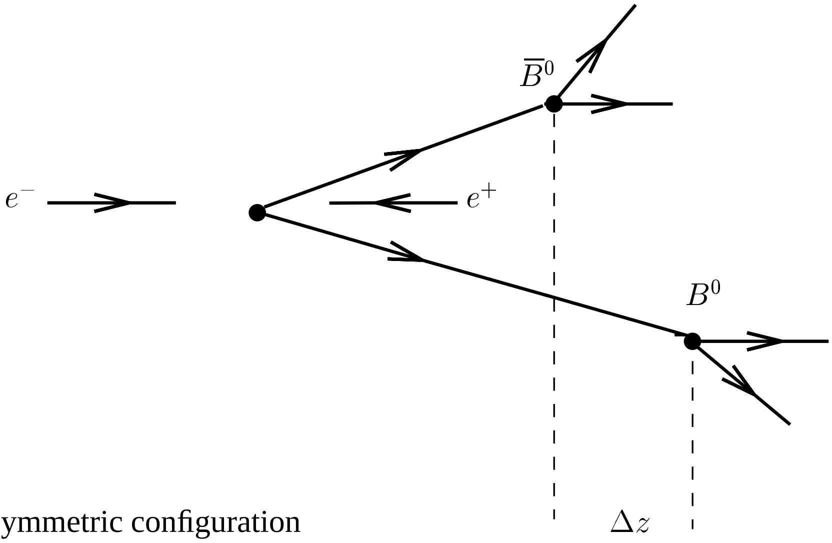

(b) asymmetric configuration

Figure 3.4: (a) In a symmetric configuration $\Delta z = |z_1 - z_2|$ which would require an accurate determination of the IP as well as the positions of the decay vertices. (b) In an asymmetric configuration Δz can be measured directly by only knowing the positions of the decay vertices.

of the luminosity is less than 0.5%. The systematic error on the absolute value of the luminosity is estimated to be 1.2%. This error is dominated by uncertainties in the samples of simulated events and the simulation of the detector.

Table 3.1: The parameters for the PEP-II storage rings are given for the original design and the improvements in the fourth year when the number of bunches were raised. The method of trickle injection for introducing new bunches into the rings was also introduced. All of these upgrades have radically increased the luminosity.

Parameters	Typical (1st year)	Typical (4th year)
Energy HER (GeV)	9.0	9.0
Energy LER (GeV)	3.1	3.1
Current HER (A)	0.7	1.55
Current LER (A)	1.3	2.45
Number of bunches	553-829	1588
Luminosity ($10^{33}\mathrm{cm}^{-2}\mathrm{s}^{-1}$)	2.5	9.213

3.2 The *BABAR* detector

The design of the *BABAR* detector was determined by the needs of the B-physics community to be able to fully reconstruct the decay of the B-mesons. The detector is a cylindrical, multi-component device that completely surrounds the IP of the colliding beams. To maximise the geometric acceptance for the boosted $\Upsilon(4S)$ decays the whole detector is offset relative to the IP by 0.37 m in the direction of the low energy beam. The inner most part is the silicon vertex tracker (SVT) surrounded by a multi-wire drift chamber (DCH) for reconstructing the charged tracks; information from the DCH is also used for particle identification. This is surrounded by a ring-imaging internal reflecting Čerenkov light detector (DIRC) for particle identification. Around these is an electromagnetic calorimeter (EMC) composed of 6580 thallium-doped CsI crystals for detecting electromagnetic showers produced by electrons and photons. All of these subsystems are inside a solenoidal, super-conducting magnet with a layered steel flux return (IFR). Between the layers of the IFR resistive plate chambers (RPC) are inserted for detecting muons and neutral hadrons. The asymmetry of the beams with the resulting boost in the forward direction means that increased angular coverage is only required at this end of the detector.

The collision of the beam particles produces many unwanted events and a trigger system enables only those that are of interest to be recorded. The trigger system was originally conceived to have three levels but the second level was found to be unnecessary although it is still kept in reserve in case a more flexible set of criteria is required; the two remaining levels are called one and three. As well as the trigger there is a comprehensive electronic system for data acquisition, monitoring and storage of the high volumes of data and control of the detector.

A right-handed coordinate system is employed with the z-axis pointing along the longitudinal axis of the drift chamber. The y-axis points upwards and the x-axis horizontally away from the centre of the PEP-II ring. The detector is rotated by an angle of 20 mrad with respect to the beam axis in order to minimise orbit distortions of the beams due to the solenoidal field; thus the z-axis is also orientated by the same angle with respect to the beam axis and has to be taken into account when boosting from the laboratory (LAB) frame to the centre-of-mass (CM) frame.

The demands on the *BABAR* detector to be able to distinguish the decay $\tau \rightarrow e\gamma$ from all of the potential backgrounds are summarised as follows:

- τ-decays are identified by their topology which is characterised by the number of charged tracks; therefore the detector needs to be able to reconstruct the trajectory of all of the charged tracks in the event;

- an accurate measurement of the momentum of the charged particles is essential as it is used for the calculation of the invariant mass of the $e\gamma$-signal; the measurement of momentum by the tracking detectors are used together with the particle identification information to calculate the four vector of a charged particle;

- the electron in the $e\gamma$-signal needs to be identified with a very high degree of probability; to help identify charged particles the detector measures a number of factors such as the charge of the particle its momentum and ionisation losses for d$E/$dx information;

- the energy of the electron and the photon in the $e\gamma$-signal have to be measured to a high precision.

The detector has several subsystems to satisfy these differing requirements and these are fully integrated to produce a complete reconstruction of each event.

A detailed scale drawing of the detector is given in Fig. 3.5 showing the sub-detectors, the magnet, the support structures and the orientation of the coordinate system. The sub-detectors and the super-conducting magnet are described in detail in the following sub-sections as well as the trigger, data acquisition and online control systems.

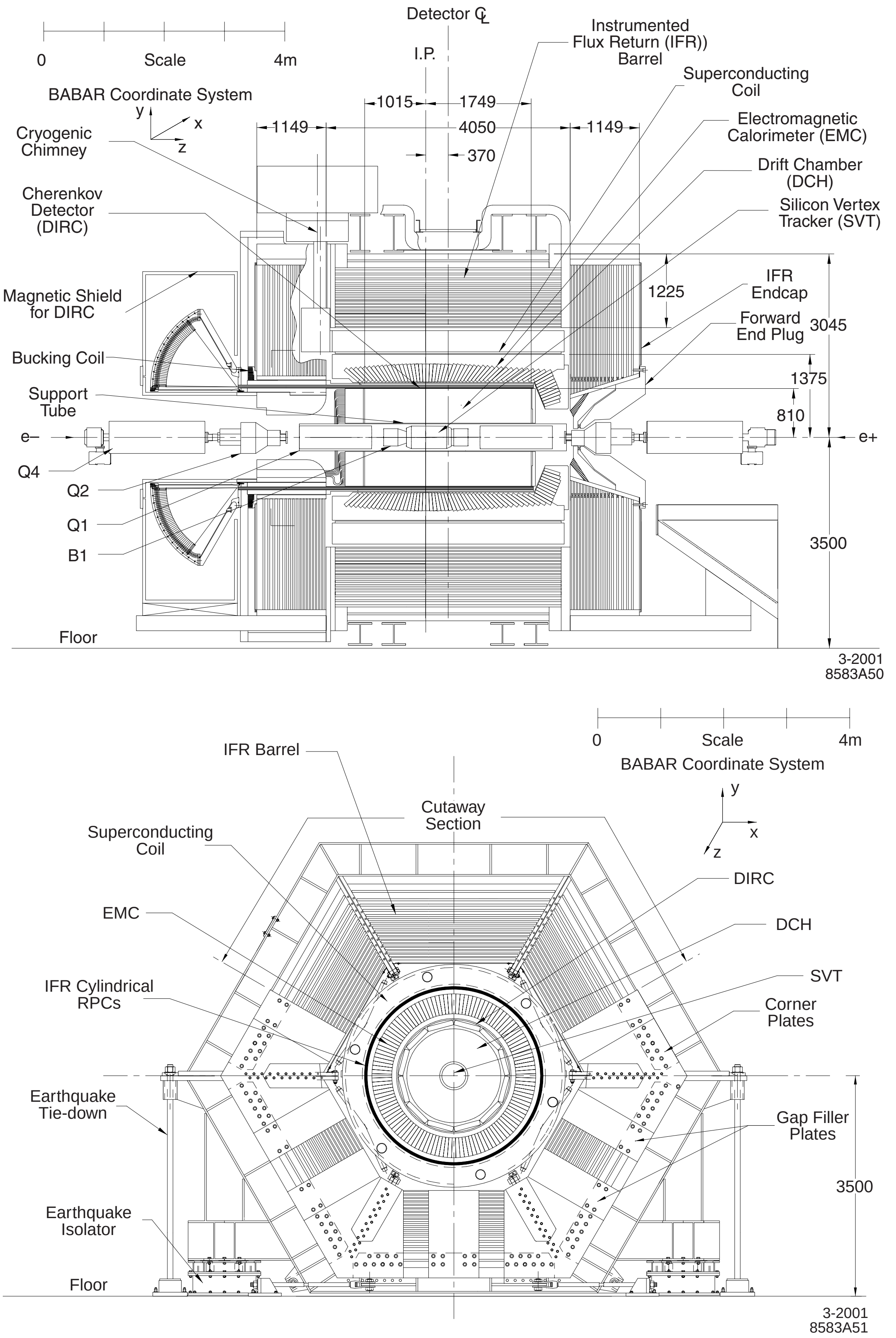

Figure 3.5: A detailed scale drawing of the the *BABAR* detector [39]. The top diagram shows a section through the front elevation. The bottom diagram shows the end elevation. The exact positions of all of the sub-detectors, magnet, support structures and the coordinate system can be clearly seen.

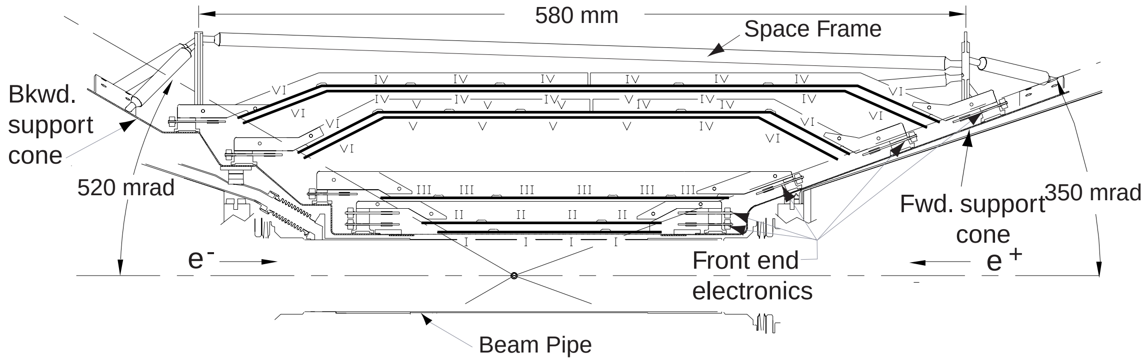

Figure 3.6: Longitudinal section of the SVT.

3.2.1 The silicon vertex tracker

The SVT is the subsystem closest to the beam pipe and surrounds the IP. It has five layers of double sided silicon strip detectors built in modules. The readout electronics is situated at the end of each module minimising the amount of material inside the active detector volume. The modules of the three inner layers are straight while the two outer layers are curved in order to maximise the solid angle coverage (Fig. 3.6).

All five layers are composed of modules that are constructed with double sided silicon microstrips with radii varying from 3.2 - 14.4 cm (Fig. 3.7). The strips on opposite sides of each sensor are orthogonal to each other with the ϕ-strips running parallel to the beam on the outer sides and the z-strips perpendicular to the beam axis on the inner sides. In order to ensure full coverage in ϕ, the inner modules are slightly tilted allowing an overlap region between neighbouring modules. The outer two layers are divided into two sublayers (4a,b and 5a,b) placed at slightly different radii to have the same effect. The coverage of the SVT is 90% of the solid angle, from 0.35 rad in the forward direction to 2.62 rad in the backward direction in θ and 2π rad in ϕ.

The hit reconstruction efficiency is measured using di-muon events and is calculated by comparing the number of tracks crossing the active area of each half module with the number of associated hits in that module. A probability of 97% is measured for a particle passing through an active module to leave a signal in both ϕ and z-strips. The spatial resolution is determined by measuring the distance from the hit to the track. The resolution in the z-direction varies between 15 and 50 μm and the resolution in ϕ is 10 to 35 μm, depending on polar angle and layer. In addition, the ionisation rate, $\mathrm{d}E/\mathrm{d}x$, is

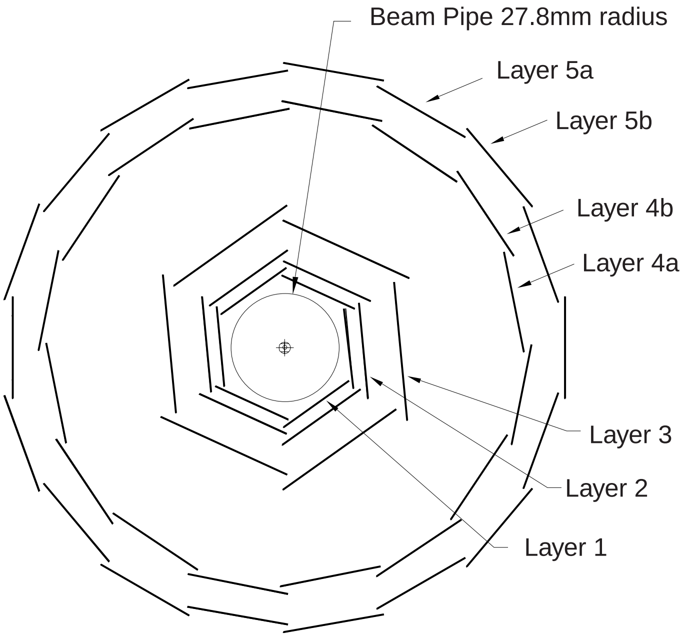

Figure 3.7: Vertical section of the SVT.

measured and used for particle identification, resulting in a 2σ separation between pions and kaons for momenta up to 500 MeV/c and between kaons and protons beyond 1 GeV/c (Fig. 3.10).

The inner three layers are used to reconstruct the trajectories of the charged tracks and decay vertices. The outer two layers provide information to match these tracks with those observed in the DCH, giving a continuous extrapolation of the tracks from the SVT to the DCH.

3.2.2 The drift chamber

The purpose of the DCH is to detect charged particles efficiently and measure their momenta and angles of their tracks precisely. It complements the measurements of the directions of the charged tracks by the SVT. The DCH also provides $\mathrm{d}E/\mathrm{d}x$ for particle identification of low momentum particles up to 700 MeV/c and information for the trigger.

The DCH is constructed of 7104, hexagonally shaped, drift cells. The cells are arranged in ten cylindrical super-layers (SL) (Fig. 3.8); each SL has four sub-layers making a total of 40. This provides a maximum of 40 spatial and ionisation loss measurements

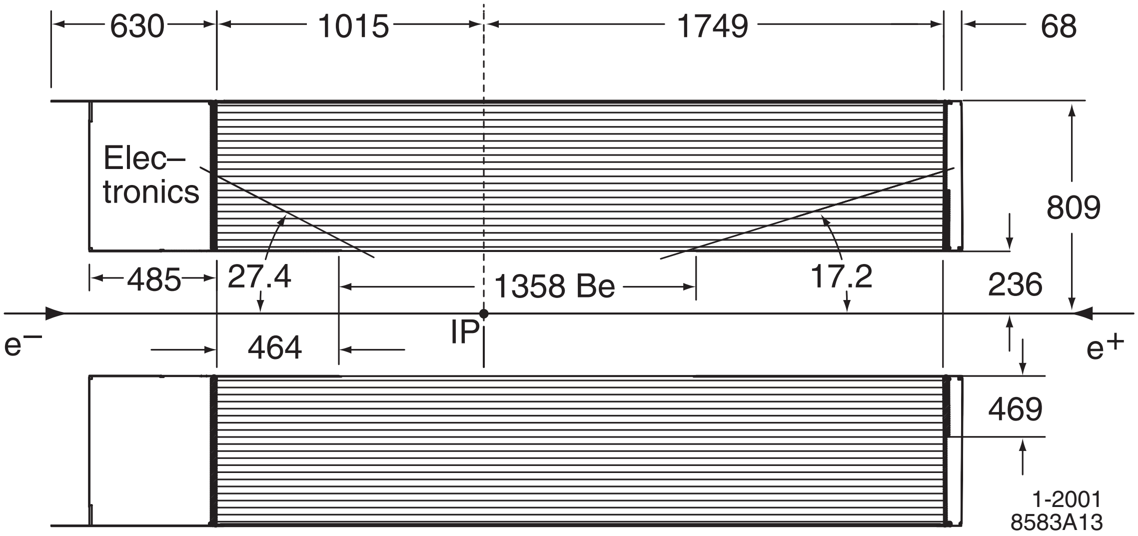

Figure 3.8: Longitudinal section of the DCH (dimensions in mm) [39].

for particles with transverse momentum $p_\mathrm{t} > 180\ \mathrm{MeV}/c$. The volume of the chamber is 5.2 m^3; it is filled with a helium:isobutane mix in the ratio 80:20 at a constant pressure of 4 mbar measured by two independent pressure gauges.

The longitudinal position of the tracks is determined by orientating wires in 24 out of the 40 layers at small angles in relation to the z-axis (stereo layers). The layout of the drift cells for the four innermost superlayers is shown in Fig. 3.9. The sense wires, operated at a voltage between 1900 V and 1960 V, are surrounded by six grounded field wires. Sense wires are made of gold plated tungsten-rhenium; field, guard and clearing wires are made of gold plated aluminium and in combination with the helium-based gas mix helps keep multiple scattering to a minimum. The inner cylindrical wall is kept as thin as possible to minimise its affect on the trajectories of electrons via coulomb interactions and reduce the incidence of photon conversions.

The total charge deposited in each drift cell is used to measure the specific energy loss $\mathrm{d}E/\mathrm{d}x$ for particles traversing the DCH. The distribution of $\mathrm{d}E/\mathrm{d}x$ measurements as a function of track momenta is shown in Fig. 3.10 and is used to aid particle identification. The superimposed Bethe-Bloch predictions for particles of different masses have been determined from selected control samples. This is complementary to measurements of $\mathrm{d}E/\mathrm{d}x$ made by the SVT in the barrel region. In the extreme forward and backward regions the DCH is the only subsystem providing some discrimination between particles

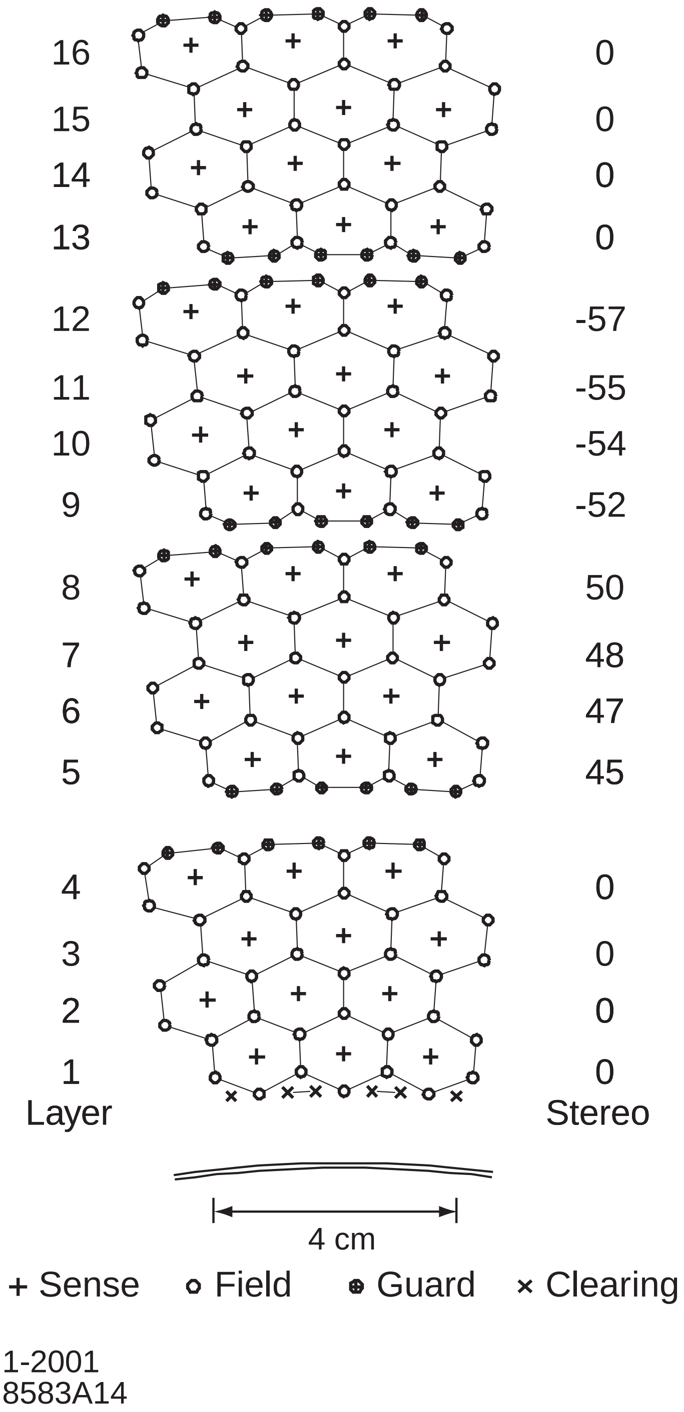

Figure 3.9: Schematic layout of the drift cells for the four innermost superlayers. Lines have been drawn between the field wires to help visualising the cell boundaries. The numbers on the right give the stereo angles (mrad) of the sense wires in each layer. The 1 mm-thick beryllium wall which separates the DCH from the SVT is shown at the bottom [39].

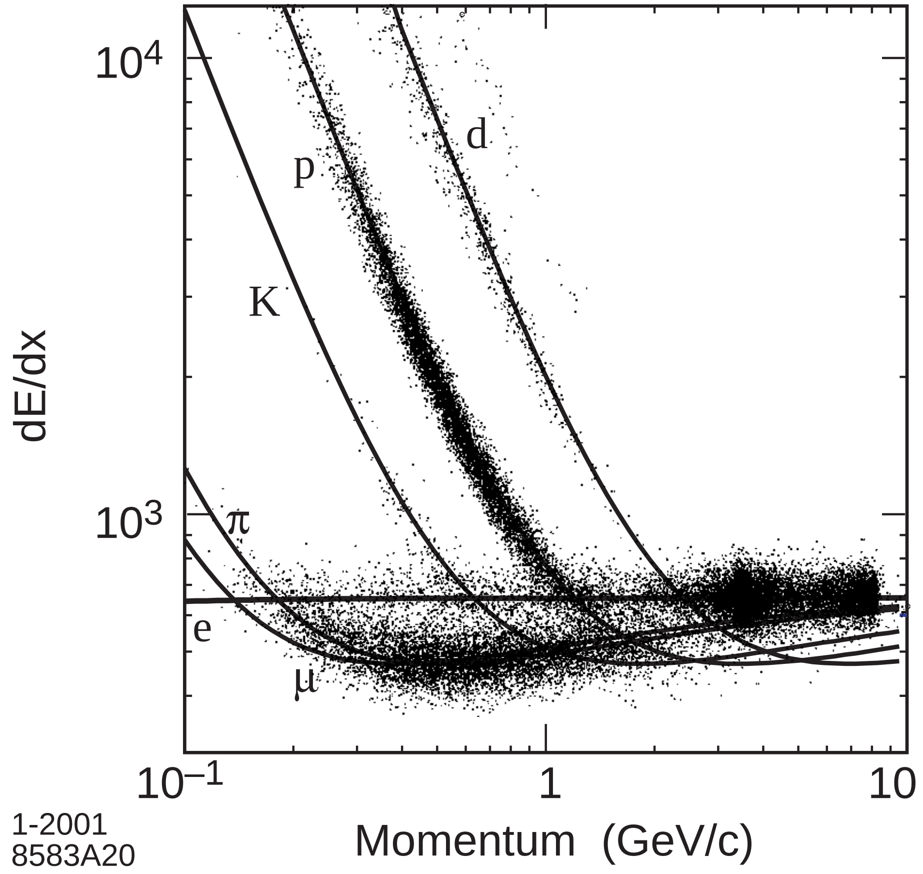

Figure 3.10: Measurement of $\mathrm{d}E/\mathrm{d}x$ as a function of track momenta. The data includes large samples of beam backgrounds, as evident from the large number of protons. The curves show the Bethe-Bloch predictions derived from selected control samples of particles of different masses: electrons, muons, pions, kaons, protons and deuterons.

of different masses. Identification of electrons uses $\mathrm{d}E/\mathrm{d}x$ information.

The reconstruction of charged particle tracks relies on combining the information from both SVT and DCH. The overall efficiency for reconstructing tracks in the DCH is determined as the ratio of the number of tracks in the DCH to the number detected in the SVT. At the design voltage of 1960 V for tracks greater than 200 MeV and polar angle $\theta > 500\,\mathrm{mrad}$ the efficiency is measured to be $98 \pm 1\%$, reducing by 5% for data recorded at 1900 V. The SVT dominates the measurement of the position and angle of the track but the DCH contributes mainly to the measurement of the transverse momentum p_{t}. The resolution in the transverse momentum is derived from cosmic muons and the data is well represented by the linear function,

$$\sigma_{p_{\mathrm{t}}}/p_{\mathrm{t}} = (0.13 \pm 0.01)\% \cdot p_{\mathrm{t}} + (0.45 \pm 0.03)\% \tag{3.1}$$

where p_{t} is measured in GeV [39].

3.2.3 The ring imaging Čerenkov detector

The system for particle identification at momenta above 700 MeV is a ring-imaging Čerenkov detector called the DIRC (detector of internally reflected Čerenkov light) and as the name implies it makes use of the Čerenkov effect. When a charged particle passes through a dispersive medium of refractive index n it excites and polarises atoms. If the particle's velocity, $\beta = p/E$, where p is the momentum and E the energy, is greater than the speed of light in that medium, i.e. if $\beta > 1/n$, then part of the excitation energy reappears as coherent radiation. Furthermore, the light is emitted in a cone at a characteristic angle θ_C to the line of motion. The speed of the particle can thus be determined using the relationship $\cos\theta_C = 1/\beta n$ and combined with the track angle and momentum from the DCH, the mass of the particle can be determined.

Using total internal reflection at a flat surface the light emitted by the particle passes along a synthetic fused silica bar to the backward end of the detector; light emitted towards the forward end is reflected by a mirror. Throughout this process the opening angle of the cone is preserved. At the backward end the light enters a standoff box filled with purified water with refractive index close to that of the quartz bars, thus reducing internal reflection at the interface. The photons are then detected by photomultiplier tubes (PMT) mounted on the standoff box. The Čerenkov light pattern on the PMT surface is a conic section, with the opening angle modified by the refraction on exiting the bar. The lower schematic in Fig. 3.11 illustrates the operation of the DIRC.

As the DIRC is inside the EMC it has to be thin and uniform to minimise the degradation of the calorimeter energy resolution. It consists of 144 synthetic fused silica bars with refractive index n=1.473, each 17 mm thick, 35 mm wide and 4.9 m long that are arranged in a 12-sided polygonal barrel. Including the support structure the DIRC occupies 80 mm radial space, corresponding to 17% of a radiation length at normal incidence. At the backward end the bars enter the standoff box where the 10752 densely packed photomultiplier tubes of 28.8 mm diameter are mounted. The layout of the DIRC is shown in the upper schematic in Fig. 3.11.

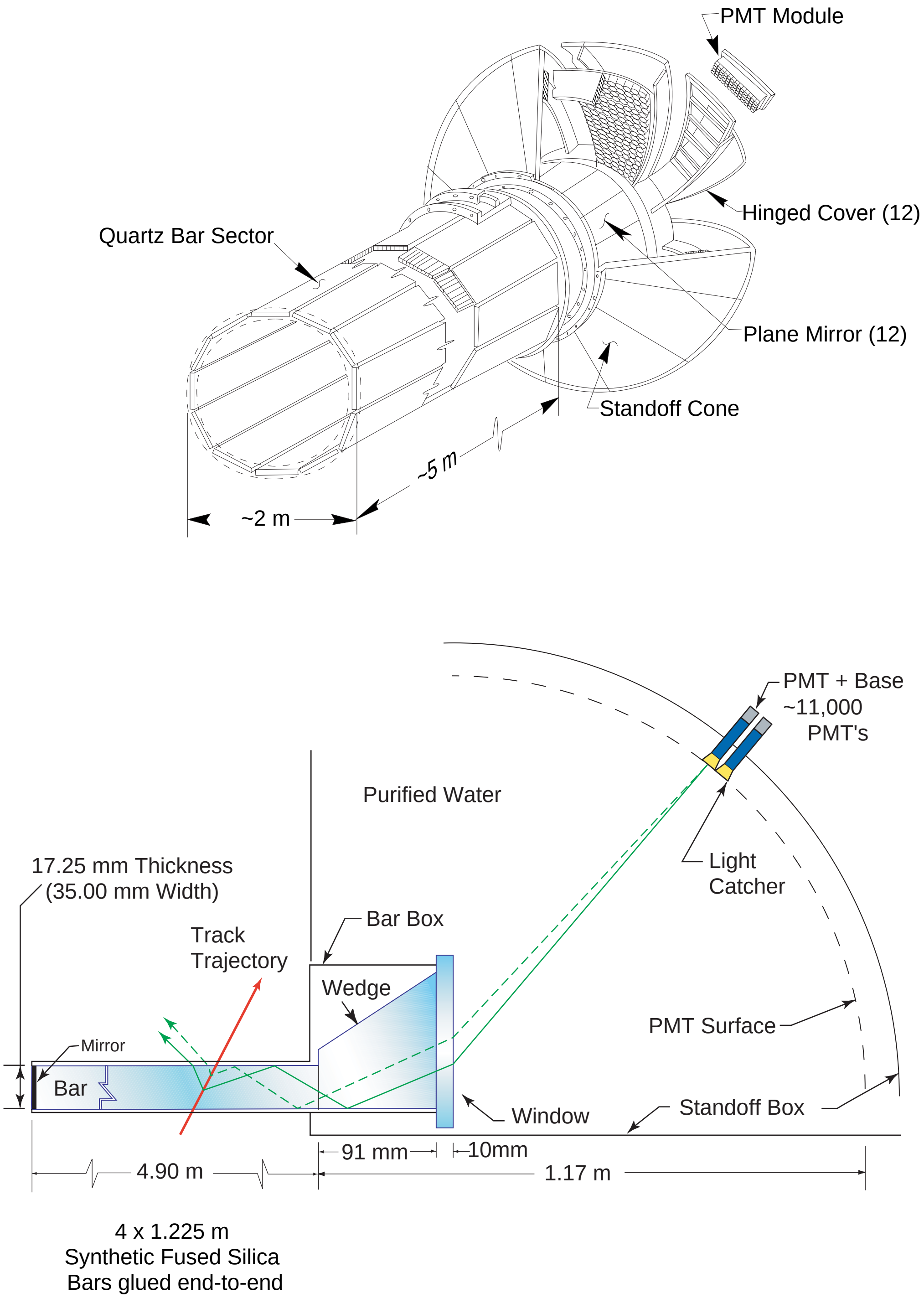

Figure 3.11: Upper: the layout of the DIRC [40]. Lower: schematic showing the basic operating principle of the DIRC [39].

3.2.4 The electromagnetic calorimeter

The purpose of the EMC is to measure the energy deposited by electromagnetic showers from charged particles and photons (with excellent efficiency and angular resolution), and is therefore a critical element of the detector. The design energy range is 20 MeV to 9 GeV.

The detecting elements are thallium-doped CsI crystals [41] whose properties are listed in Table 3.2. In total there are 6580 crystals arranged in a cylindrical barrel (containing 5760) and a conically shaped endcap at the forward end (Fig. 3.12). The barrel provides full azimuthal coverage and combined with the endcap provides polar angle coverage from 15.8° to 141.8°, which corresponds to 90$\%$ of the solid angle in the centre of mass.

Table 3.2: Properties of CsI(Tl).

Parameter	Values
Radiation length	1.85 cm
Moliere radius	3.8 cm
Density	4.53 g/cm^3
Light yield	50 000$\gamma/\,\mathrm{MeV}$
Light yield temp. coeff.	0.28$\%$/°C
Peak emission λ_{max}	565 nm
Refractive index	1.80
Signal decay time	680 ns (64$\%$)
	3.34 μs (36$\%$)

The crystals have a tapered trapezoidal cross-section with dimensions varying across the 56 rings to provide hermetic coverage. CsI is deliquescent and it is most important that the calorimeter is airtight to prevent water from the air entering. A sophisticated cooling system is used to keep the EMC at a temperature of 20$\pm$1°C. The constant temperature is maintained for three reasons: the leakage current of the photodiodes rises exponentially with temperature; the large number of epoxy joints between the diodes and the crystals could experience stress due to differential thermal expansion; the light yield of CsI(Tl) is weakly dependent on temperature.

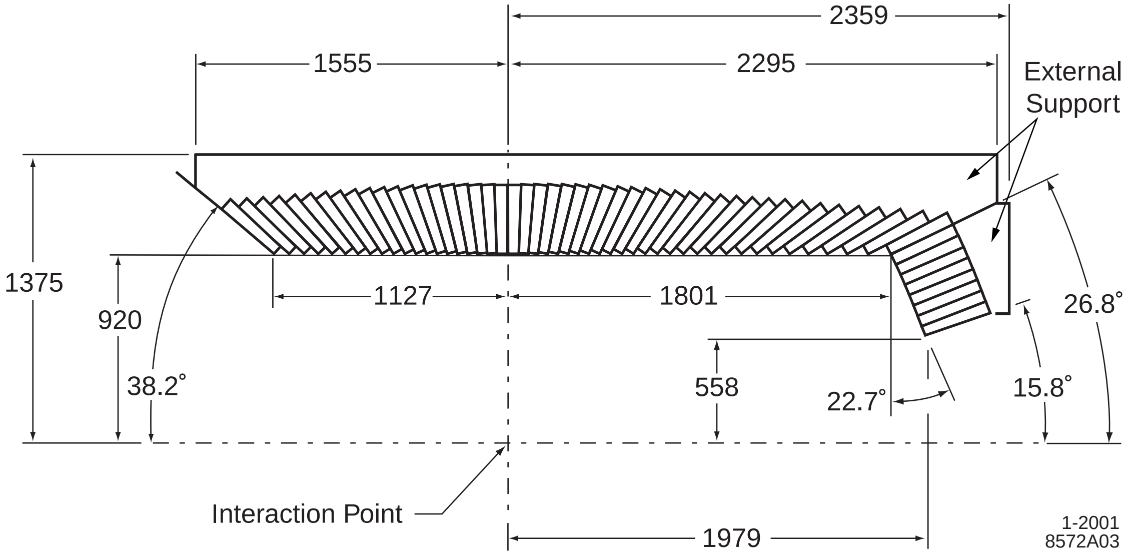

Figure 3.12: Longitudinal section through the top half of the EMC showing the arrangement of the 56 crystal rings. The EMC is axially symmetric around the z-axis. The dimensions are in mm [39].

As well as being a total-absorbing scintillating medium the crystals act as light guides for the photodiodes on the back surface. Although most of the light is internally reflected some light is transmitted at the side surfaces and therefore the crystal is wrapped in a white reflective material to recover some of it. Each crystal is further wrapped in aluminium and electrically connected to the metal housing to create a Faraday shield.

The two photodiodes used as light detectors are silicon PIN diodes and are glued to a polystyrene substrate which itself is glued to the rear surface of the crystal; two diodes are used for redundancy. If both are operating normally an average of the signals from each is used. If one malfunctions it can be isolated and the other used on its own. Each diode has a low-noise pre-amplifier that is mounted near to the crystal to form a complete unit. A diagram showing how each crystal is wrapped and the electronics is mounted is shown in Fig. 3.13.

The crystals are mounted in modules that are supported individually from an aluminium frame. The frame is constructed in three sections, the barrel and two semi-circular structures for the endcap (Fig. 3.14).

The separate outputs from the photodiodes are in analogue form and are preamplified, shaped and digitised. The signal is then amplified in four ranges: x1, x4, x32 and x256. The highest of the four resulting amplified signals that has not saturated the amplifier is

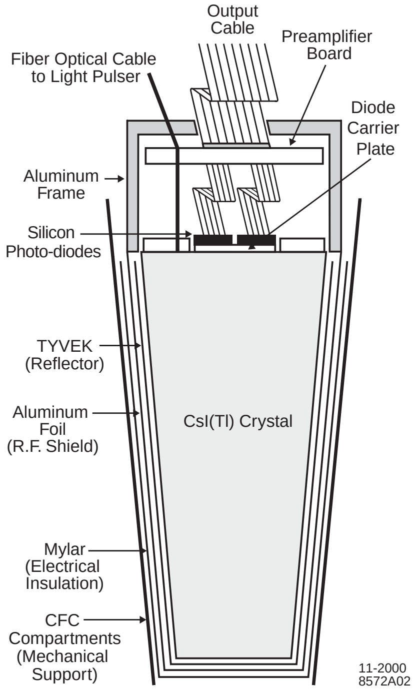

Figure 3.13: A wrapped CsI(Tl) crystal including the front-end readout package on the rear face. It also shows the tapered trapezoidal CFC compartment which is open at the front [39].

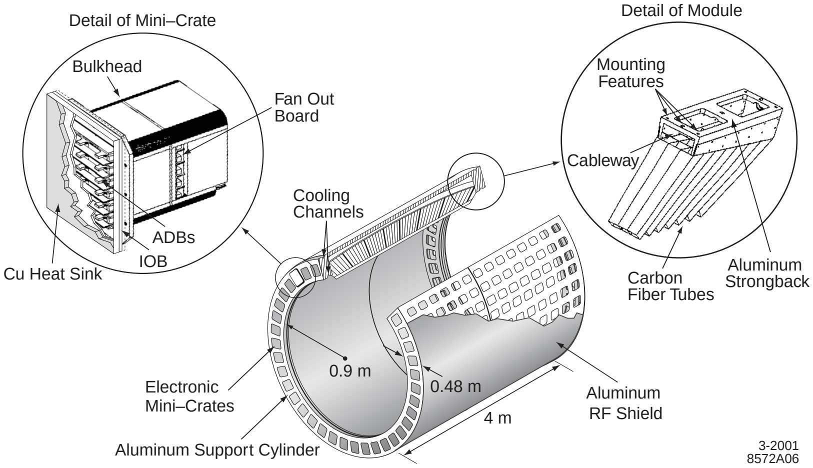

Figure 3.14: Diagram of the barrel of the EMC [39].

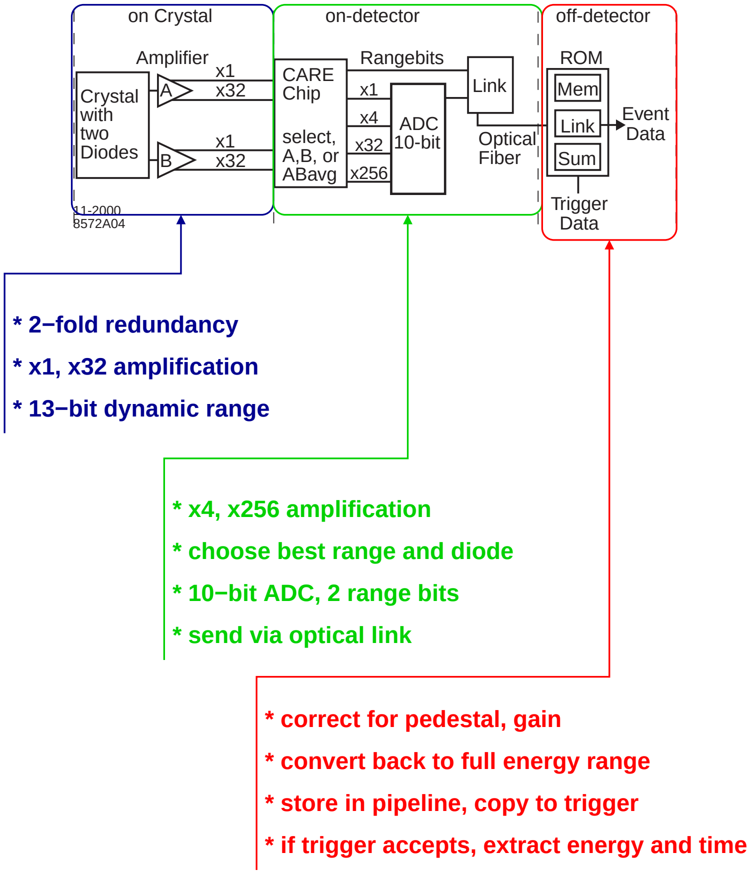

* 2−fold redundancy
* x1, x32 amplification
* 13−bit dynamic range

* x4, x256 amplification
* choose best range and diode
* 10−bit ADC, 2 range bits
* send via optical link

* correct for pedestal, gain
* convert back to full energy range
* store in pipeline, copy to trigger
* if trigger accepts, extract energy and time

Figure 3.15: Schematic of the stages from the raw analog signal to the digitised, calibrated signal suitable for inclusion in the event data [39].

selected and digitised to form a 10 bit word. A further two bits are used to record which of the four ranges of amplification it originated from. The amplification and digitising process takes place on the detector (Fig. 3.15). If the event is accepted by the first level of the trigger the signal is then passed, via a fibre optic link, to the readout module (ROM) which is situated in the electronics hut approximately 20 m away from the detector. A concrete wall (the radiation wall) separates the electronics hut from the detector. An optical link is used for speed of transfer because of the needs of the third level of the trigger.

Data is stored in the pipeline in the ROM awaiting a decision from the level three of the trigger to accept or reject the event. If the event is accepted then the signal from the EMC is output and integrated with signals from the other subsystems (Fig. 3.16).

The calibration and monitoring system sets the energy scale and provides information

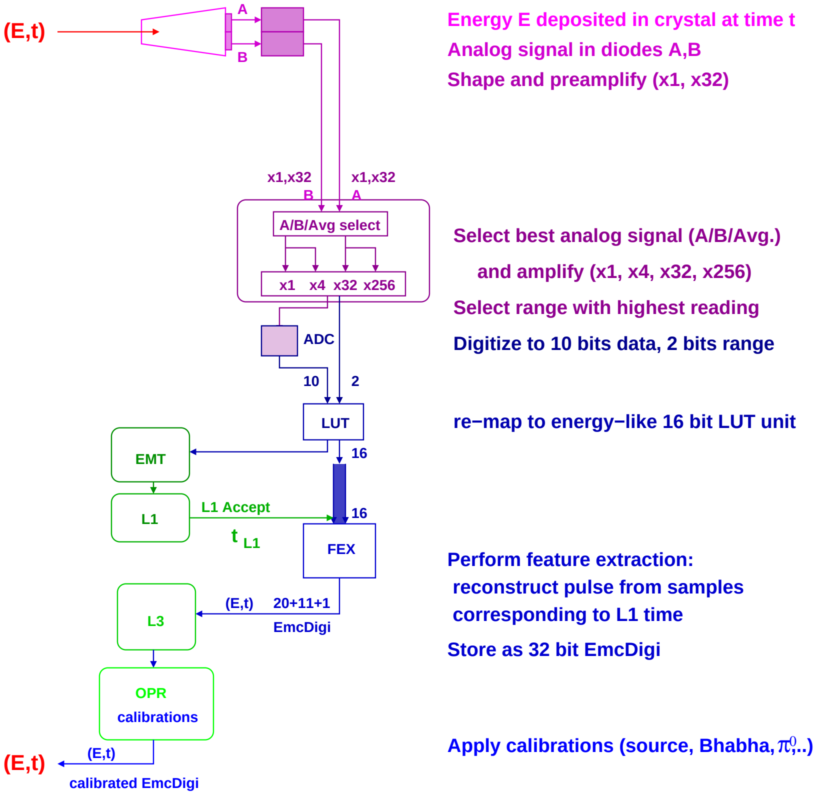

Figure 3.16: Schematic of the readout electronics which converts the raw analog output from the crystal to a digital signal called an EmcDigi [39].

concerning the condition of the detector and any changes in its response. As the life-time of the experiment is possibly ten years or more it is important to monitor any degradation in the crystals as these would be very difficult to replace. The system has four separate parts:

- Charge injection to the electronics calibration to produce a linear response better than 0.1$\%$;

- 6.13 MeV photons used to set the energy scale for individual crystals to better than 0.5$\%$. The photons are produced by flourinert molecules being excited by a neutron source via the reaction $F^{19} + n \rightarrow N^{16} + \alpha, N^{16} \rightarrow O^{16*} + \beta, O^{16*} \rightarrow O^{16} + \gamma$;

- a light pulser system, using a xenon lamp, to monitor short term changes to better than 0.5$\%$;

- physics processes, such as Bhabha events, are used to determine the energy scale to better than 0.5$\%$ for each crystal and 0.25$\%$ for clusters; calibration of low energy clusters uses π^0 decays and for higher energies corrections are derived from single

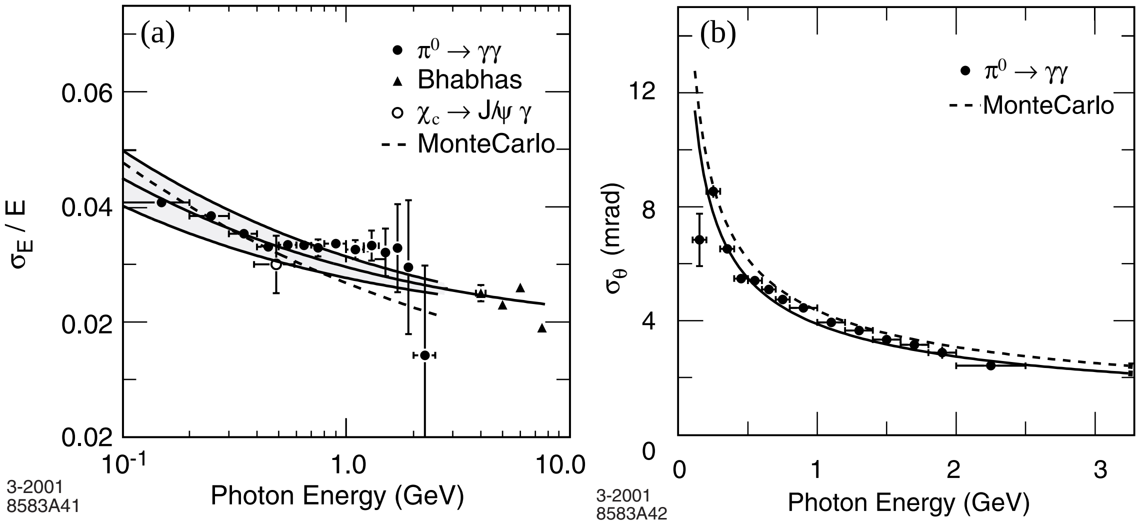

Figure 3.17: (a) Energy resolution of the EMC as measured from several processes. The middle solid line is a fit to the data and the area bounded by the upper and lower solid lines indicates the error (Eq. 3.2). (b) Angular resolution for photons from π^0 decays as a function of the photon energy together with a fit to a parameterisation of the form of Eq. 3.3 [39].

photon Monte Carlo and radiative Bhabha events. Corrections to cluster energies are typically of the order of 5%. The energy and angular resolution of the EMC measured from a variety of processes is presented in Fig. 3.17.

The resulting energy resolution of the EMC is [39]

$$\frac{\sigma_E}{E} = \frac{(2.3 \pm 0.3)\%}{\sqrt[4]{E(\,\mathrm{GeV})}} \oplus (1.9 \pm 0.1)\% \tag{3.2}$$

and for the angular resolution a value of

$$\sigma_\theta = \sigma_\phi = \frac{(3.9 \pm 0.1)\mathrm{mrad}}{\sqrt{\mathrm{E}(\,\mathrm{GeV})}} + (0.0 \pm 0.04)\mathrm{mrad} \tag{3.3}$$

is found.

The four momentum of the photons is entirely determined from the EMC measurements. The particle identification algorithm used to identify a track as an electron uses information from the EMC. Therefore reliable and accurate determinations of the energy of particles and the angles of their trajectories are essential for this analysis.

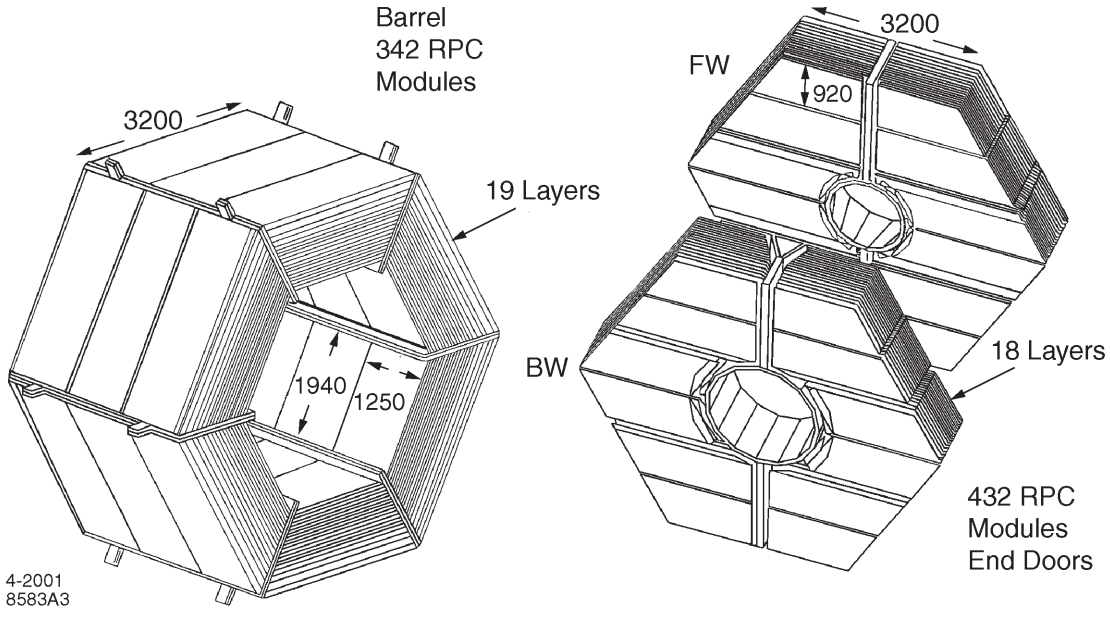

Figure 3.18: Barrel and endcaps of the IFR indicating the RPC module structure [39].

3.2.5 The instrumented flux return

The instrumented flux return (IFR) is the outermost subsystem of the *BABAR* detector. Its primary purpose is the detection of muons and neutral hadrons, but it is also the flux return for the 1.5T superconducting magnet and the principal supporting structure for the rest of the subsystems of the detector. It is constructed with segmented layers of iron and between the layers resistive plate chambers (RPCs) provide the active part of the subsystem. The IFR comprises a barrel and two endcaps for close to 4π solid angle coverage (Fig. 3.18). The plates are segmented into eighteen pieces varying from 2 cm for the innermost plates to 10 cm for the outermost.

There are 21 active elements to the IFR, with a double-layered RPC around the EMC, a planar layer of RPCs between the coils of the solenoid and the iron, 17 layers in the gaps formed by the segmentation and a single layer on the outside. The RPCs are filled with a mixture of gases of approximately equal amounts of argon and freon 134A ($\mathrm{C_2H_2F_4}$) plus a small percentage of isobutane. Particles passing through the RPC cause ionisation of the gas; the resulting streamers are sensed by external capacitive readout strips made of aluminmium on a mylar substrate. Muons and neutral hadrons are identified by looking at the transverse and longitudinal interaction patterns.

Muons produced by cosmic rays are used to calibrate the IFR and calculate its efficiency. In the first year of operation 75% of the RPC modules had an efficiency exceeding 90%. However, due to overheating, gas flow problems and other reasons that are not fully understood the performance of a large fraction of RPCs has deteriorated, resulting in an average efficiency of around 60%. The IFR has had other problems due to the larger than normal backgrounds experienced during run 3. This has not had a major impact on the analysis presented here since the signal being searched for does not contain muons or neutral hadrons.

3.2.6 The solenoid magnet

The *BABAR* magnet system consists of a superconducting solenoidal magnet, a segmented flux return, as described above, and a field compensating or bucking coil. This system provides the 1.5 T magnetic field which enables the measurement of the momentum of the charged particles passing through the DCH. The magnet is positioned between the EMC and the IFR and the combination of the magnet and the flux return also provides a structure to support the other components of the detector (Fig. 3.5).

A solenoidal magnetic field of 1.5 T was specified in order to achieve the desired momentum resolution for charged particles. The topology of the magnet was designed such that the magnitude of the field inside the tracking volume is uniform to allow tracks to be found and fitted quickly.

The magnets that control the beams inside the detector are by necessity inside the solenoid. Thus a second requirement of the design of the magnet was to minimise any disturbance of the operation of the beams magnets and hence the perturbation of the beam. A summary of some of the parameters of the magnet and the bucking coil is presented in Table 3.3.

3.2.7 The trigger system

The purpose of the trigger system is to discriminate events of physics interest from other processes, such as beam gas interactions, and to initiate recording and readout of the former whilst rejecting the latter.

The trigger is a two stage system: levels one (L1) and three (L3) [42]. L1 has to be very fast and differentiates between potential physics events and beam induced back-

Table 3.3: A few of the parameters for the solenoidal magnet and the bucking coil.

Field parameters		
Central field	1.5	T
Max. radial field	< 0.25	T
Leakage into PEP-II	< 0.01	T
Stored energy	27	MJ
Operating current		
Main coil	4596	A
Bucking coil	200	A

grounds. For speed of operation it is hardwired and situated on the detector but as a consequence is only able to make decisions based on a simple set of data. L3 is exterior to the detector, slower as it is software-based and has the ability to be more sophisticated and discerning in its decision making process.

As the number of signal channels exceeds 200,000 the trigger has to make decisions on a reduced set of data primarily for requirements of speed. Both parts of the trigger use inputs from the DCH, EMC and IFR to produce reduced representations of the data such as simple reconstruction of track segments and clusters of adjacent crystals. The level 3 trigger has access to the complete event data including timing information and filters on key event parameters like track parameters, cluster energies and event topologies. These can be combined to form more complex selection criteria for specific physics processes. L1 is designed to reduce the event rate to less than 2 kHz so that the slower L3 has enough time to carry out a more detailed analysis of each event. The final output rate is of the order of 100 Hz.

The trigger system identifies $\tau^+\tau^-$ events with 90% efficiency, $B\overline{B}$ events with an efficiency exceeding 99% and continuum events with at least 95%. It was designed to operate under conditions of ten times the expected background rate and to contribute less than 1% to dead time. This last criterion has proved very important as the background rate has increased with the increasing luminosity of PEP-II.

3.2.8 Data aquisition and online computing

The data aquisition and online computing system is responsible for moving the data from the electronics on the detector to the final recording of the reconstructed events. It also provides the operator with a graphical interface to control and monitor the detector while it is running and taking data.

Online data flow software (ODF) connects, controls and monitors the passage of the data from the detector. ODF is divided into two parts: the first part of the code is embedded in the processors in the ROMs where the data is readout from the detector; the second part is software in a farm of dedicated computer processors where the data is stored before reconstruction.

Online event processing (OEP) receives the data from ODF and orchestrates the following tasks: applying the L3 trigger algorithms; fast monitoring to assure data quality; merging the multiple output streams and logging them to disk storage.

Online prompt reconstruction (OPR) links the online and offline systems. It reads the raw data stored to disk by OEP and, selecting physics events, performs the final complete reconstruction whilst applying the rolling calibration. The rolling calibration is the set of constants generated during data-taking that reflect the condition of the detector in that period. An example is when a faulty channel in one of the subsystems has been isolated while waiting for an opportunity to make a repair as it would be impracticable to continually open the detector for servicing.

Online detector control (ODC) and the online run control (ORC) provide the operator with all the information required to run the detector efficiently and safely. They allow communication with the PEP-II control room for online information about the status of the beams and the magnet control system. The operator can run the detector in different configurations, such as when taking comic ray data for the calibration of the IFR, and these are stored in the configurations data base.

3.3 Data used for the analysis

The data set is divided into runs, each run starting after the summer shutdown and continuing through to the following summer. The analysis described in this thesis uses data taken from 1999 to mid-2003, referred to as runs 1, 2 and 3 (Fig. 3.19). The total amount

2004/03/30 09.20

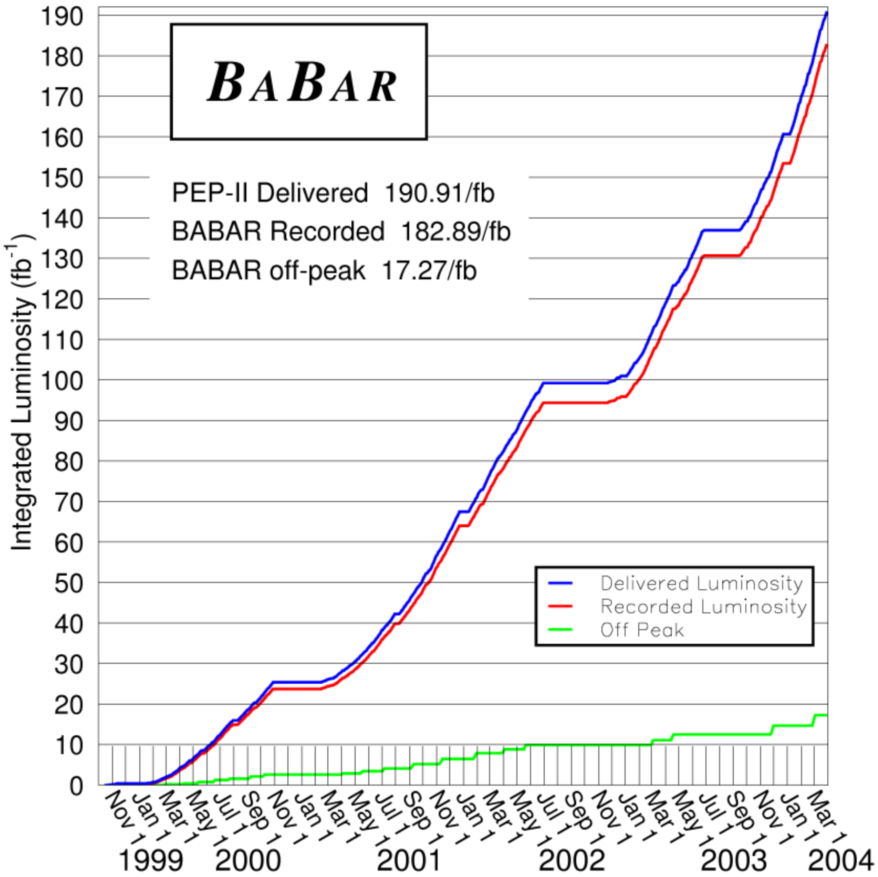

Figure 3.19: The total on and off peak data recorded by the *BABAR* detector between 1999 and mid-2004. This analysis used data taken up to mid-2003.

of data taken during this period was 124.4 fb^{-1}; 112.5 fb^{-1} was collected on-peak, at the $\Upsilon(4S)$ mass whilst the remainder was collected off-peak, at a centre-of-mass energy 40 MeV below the resonance. This resulted in a data set of approximately a 111 million τ pairs for the analysis. The data were processed using standard *BABAR* software.

The quality and size of the data set generated by the *BABAR* detector in conjunction with the PEP-II collider is sufficient to carry out a search for the rare decay $\tau \to e\gamma$. The analysis is described in detail in the remainder of the thesis.

Chapter 4

Event selection

The high luminosity provided by the *BABAR* detector, coupled with a 0.89 $\mathrm{nb}\ \tau^+\tau^-$ cross-section near the operating energy 10.58 GeV in the CM, provides a large data set that can be used to search for rare τ-decays. The collider produces many types of event that form a background to the signal; all of these various processes with their respective cross-sections calculated at $\sqrt{s} = M(\Upsilon(4S))$ are given in Table 4.1.

Table 4.1: Cross-sections for all the various processes produced by the PEP-II collider at the interaction point of the *BABAR* detector calculated at $\sqrt{s} = M(\Upsilon(4S))$ [43]. The cross-section for the Bhabha events was calculated for the acceptance of the EMC.

$e^+e^- \rightarrow$	Cross-section (nb)
$\tau^+\tau^-$	0.89
$u\bar{u}, d\bar{d}, s\bar{s}$	$1.39, 0.35, 0.35$
$c\bar{c}$	1.30
Bhabha	5.10
$\mu^+\mu^-$	1.16
Two-photon	1.00
B^+B^-	0.535
$B^0\overline{B}^0$	0.535

The objective of this part of the analysis is to find discriminating variables that can be used to select signal events and remove unwanted backgrounds. Cutting away the backgrounds may simultaneously reduce the signal, and therefore a balance has to be struck between the competing needs of reducing the backgrounds whilst minimising the effect on the efficiency of detecting potential signal events.

The process of selecting events has two stages, a preselection followed by a set of more stringent cuts. The preselection allows the data sample to be reduced to a manageable level by rejecting mainly Bhabha and multihadron events. Due to its high cross-section Bhabha events ($e^+ e^- \rightarrow e^+ e^-$) are a major background and their removal is an important aspect of the analysis. The preselection is a set of requirements placed on the data to exclude Bhabha events and identify τ-decays with a particular topology. Identification of the electron in the $e\gamma$-system is also carried out at this stage. All events are passed through a set of standard *BABAR* filters to separate the data into events of different types. One of these filters is dedicated to identifying τ-decays. Identification of electrons is also carried out by a standard *BABAR* algorithm. Both the τ-filter and the algorithm for electron identification are described in sections 4.6.4 and 4.6.3 respectively. All other cuts used are non-standard *BABAR*.

The chapter proceeds with a description of the topology and structure of the decay products of a typical τ-pair, how potential signal events can be identified and the model used to simulate $\tau \rightarrow e\gamma$. Then the backgrounds that can mimic the signal and the method of selecting events are discussed. This is followed by a summary of the strategy of the analysis. Finally a comprehensive description of the preselection and the selection cuts is presented.

4.1 τ-decays

τ-decays are characterised by the number of charged particles produced which in turn dictates the topology of the event; in particular the number of charged particles is always odd. 85.35±0.07$\%$ of all τ-decays have a single charged particle, commonly referred to as 1-prong, 14.57±0.07$\%$ decay to 3-prongs, 1.0±0.06x$10^{-3}\%$ decay to 5-prong and $<$ 2.4x$10^{-6}\%$ 7-prong [7]. Therefore in 72.84$\%$ of τ-pairs both decay with a single charged particle, commonly referred to as a 1-1 topology, 12.43$\%$ have a 1-3, 2.12$\%$ have a 3-3; other topologies are negligible. Only τ-decays with a 1-1 topology have been used in the analysis because of their high probability of occurrence and simple identification. To use events with a 1-3 topology would require a separate analysis as the backgrounds are

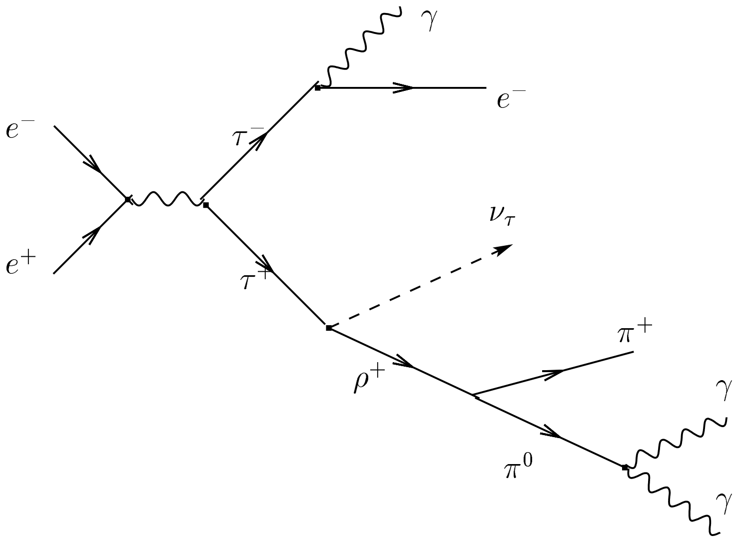

Figure 4.1: A possible signal event, with one τ decaying to $e\gamma$ and the other decaying hadronically. The electron and charged pion correspond to the two charged particles of the 1-1 topology.

different.

Hence in this analysis the search is for the decay of a pair of τ-leptons, one decaying into the selected signal mode ($\tau^\pm \to e^\pm\gamma$), the other decaying via all of the known Standard Model τ-decays given in Table 4.1 that have one charged particle. An example is shown in Fig. 4.1.

4.2 Characteristics of signal events

At this stage of the analysis, in the signal events that will be considered, there are two sets of decay products each containing one charged particle. To separate them it is convenient to divide the event into two halves (hemispheres) by using the thrust axis (Fig. 4.2).

The thrust T of an event is defined as

$$T = \frac{\sum_i |\vec{P_i} \cdot \hat{n}|}{\sum_i |\vec{P_i}|}, \tag{4.1}$$

where $\vec{P_i}$ is the three momentum of particle i and $\hat{n}$ is the unit vector for which T is a maximum. The sums are over all of the charged particles and photons in the event. The plane perpendicular to the thrust axis divides the event into two hemispheres and only

Table 4.2: Branching fractions for all of the known τ^--decay modes used in the generation of samples of simulated $\tau \to e\gamma$ signal and SM τ events. The values were taken from the PDG 2004 [7]. The table has been divided into one, three and five prong modes.

Decay channel	BF (%)
1 prong	
$\tau^- \to e^-\overline{\nu}_e\nu_\tau$	17.865 ± 0.06
$\tau^- \to \mu^-\overline{\nu}_\mu\nu_\tau$	17.355 ± 0.06
$\tau^- \to \pi^-\nu_\tau$	11.084 ± 0.11
$\tau^- \to \pi^-\pi^0\nu_\tau$	25.375 ± 0.14
$\tau^- \to \pi^-2\pi^0\nu_\tau$	9.15 ± 0.14
$\tau^- \to K^-\nu_\tau$	$0.695\times10^{-3}\pm0.23$
$\tau^- \to K^-\pi^0\nu_\tau$	$0.52\times10^{-3}\pm0.30$
$\tau^- \to K^0\pi^-\nu_\tau$	$0.83\times10^{-3}\pm0.04$
$\tau^- \to 3\pi^0\pi^-\nu_\tau$	1.262 ± 0.10
$\tau^- \to K^0\pi^-\overline{K}^0\nu_\tau$	$1.67\times10^{-3}\pm0.01$
$\tau^- \to K^-K^0\pi^0\nu_\tau$	$1.54\times10^{-3}\pm0.02$
$\tau^- \to K^-\pi^0\pi^0\nu_\tau$	$0.58\times10^{-3}\pm0.02$
$\tau^- \to \pi^-\overline{K}^0\pi^0\nu_\tau$	$3.77\times10^{-3}\pm0.04$
$\tau^- \to \pi^-\pi^0\gamma\nu_\tau$	0.080 ± 0.02
$\tau^- \to K^-K^0\nu_\tau$	$1.54\times10^{-3}\pm0.16$
$\tau^- \to \eta\pi^-\pi^0\nu_\tau$	$1.74\times10^{-3}\pm0.24$
3 prong	
$\tau^- \to 2\pi^-\pi^+\nu_\tau$	9.23 ± 0.10
$\tau^- \to 2\pi^-\pi^+\pi^0\nu_\tau$	4.365 ± 0.09
$\tau^- \to 2\pi^-\pi^+2\pi^0\nu_\tau$	$5.01\times10^{-3}\pm0.04$
$\tau^- \to 2\pi^-\pi^+3\pi^0\nu_\tau$	$0.25\times10^{-3}\pm0.08$
$\tau^- \to K^-\pi^-\pi^+\nu_\tau$	$3.01\times10^{-3}\pm0.04$
$\tau^- \to K^-\pi^-K^+\nu_\tau$	$1.59\times10^{-3}\pm0.07$
5 prong	
$\tau^- \to 3\pi^-2\pi^+\nu_\tau$	$8.2\times10^{-4}\pm0.06$
$\tau^- \to 3\pi^-2\pi^+2\pi^0\nu_\tau$	$1.8\times10^{-4}\pm0.27$

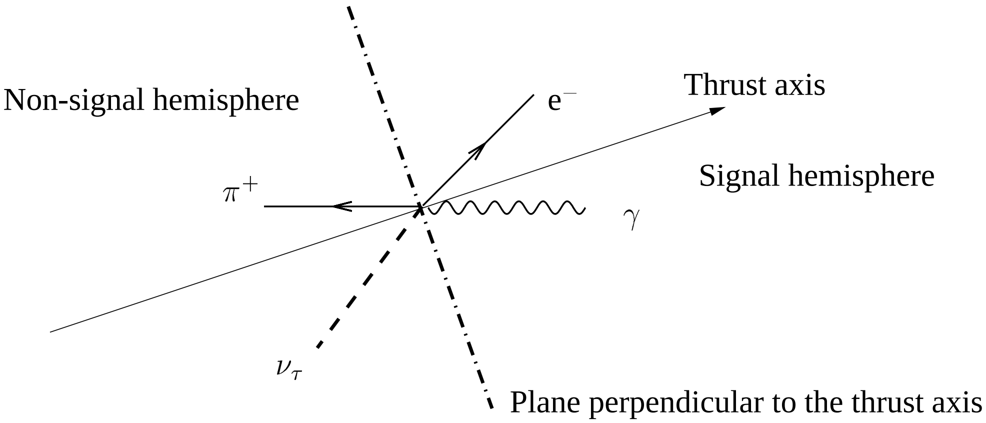

Figure 4.2: A signal event. The signal hemisphere has to have an electron and a photon with the invariant mass of the $e\gamma$-signal being equal to the τ-mass and its total energy equal to the energy of the beam.

events with one charged particle per hemisphere are accepted.

As the search is for a neutrinoless decay, there cannot be any missing energy on the signal side, unlike the non-signal side which has to have missing energy. The invariant mass and total energy of the $e\gamma$-signal must be equal to the τ-mass M_τ, i.e. 1.777 GeV, and the energy of the beams in the CM frame E_{beam}, i.e. 5.28 GeV. It is convenient to represent these two variables on a two dimensional plane of invariant mass and energy as shown in Fig. 4.3. The signal should be concentrated in a region about the point (M_τ, E_{beam}), although there are tails either side where the $e\gamma$-signal has a lower or greater invariant mass and energy. These tails originate from two sources. First, initial state radiation leads to events where the invariant mass of the $\tau^+\tau^-$-system is reduced relative to the centre-of-mass energy. Therefore some will be produced with the $e\gamma$-system having a total energy less than 5.28 GeV. Secondly some events may not be reconstructed precisely due to measurement errors and the $e\gamma$-system may have its total energy and invariant mass greater or less than E_{beam} or M_τ respectively.

4.3 The signal model

Some assumptions have to be made when constructing the model for use in generating a sample of simulated signal events. Specifically, it is assumed that in the rest frame of the τ-lepton the electron and photon of the $e\gamma$-signal are produced istropically. Due to the small mass of the electron, the electron-photon pair will share the energy of the τ-lepton

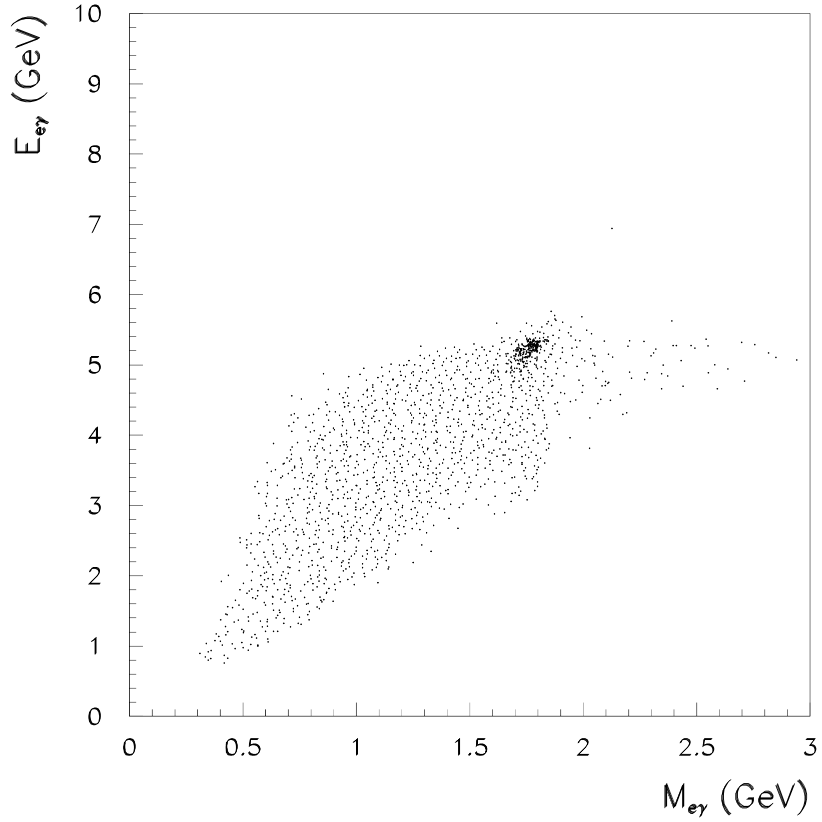

Figure 4.3: Distribution of the invariant mass ($M_{e\gamma}$) and total energy ($E_{e\gamma}$) for simulated signal events that have been fully reconstructed. The $e\gamma$-signal is concentrated about the point ($M_{e\gamma} = M_\tau$, $E_{e\gamma} = E_{\text{beam}}$). The tails on either side of the signal region are due to initial state radiation and/or measurement error.

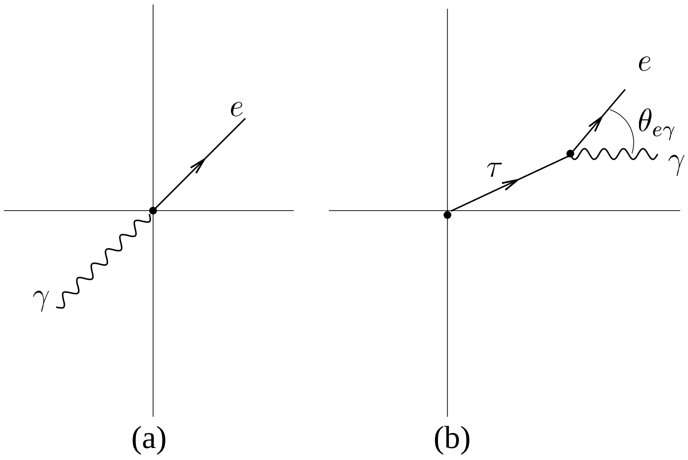

Figure 4.4: The electron-photon pair produced in (a) the τ-rest frame isotropically and (b) the CM frame.

equally and will be emitted back to back (Fig. 4.4). Boosting from the τ-rest frame to the centre-of-mass frame of the e^+e^--reaction means that the angle between the electron and the photon $\theta_{e\gamma}$ is no longer a constant π-radians but varies between $0 \rightarrow 2\pi$ radians (Fig. 4.4).

The distribution of cos$\theta_{e\gamma}$ in the CM frame is given in Fig. 4.5 and it can be seen that it has a peak around cos$\theta_{e\gamma} = 0.7$ and is flat near cos$\theta_{e\gamma} = 1.0$. The variable cos$\theta_{e\gamma}$ will be one of several used to discriminate between signal and backgrounds because the distributions for some of the important backgrounds are the reverse with a peak near cos$\theta_{e\gamma} = 1.0$ and flat in the region around cos$\theta_{e\gamma} = 0.7$ (Fig. 4.14).

A check is made on the angle θ^* between the boost direction to the rest frame of the τ-lepton and the track of the electron produced in the decay. The distribution of cosθ^* is found to be flat (Fig. 4.6) corresponding to an isotropic two-body decay.

The $\tau \rightarrow e\gamma$ mode was added to the other SM τ-decays in the generator `KK2f` and decayed with `TAUOLA` [44].

4.4 Backgrounds

The sources of background events are listed in Table 4.5 along with their cross-section for the *BABAR* detector and the amount of simulated events used to investigate the effectiveness of the cuts in removing them. The efficiency of the cuts in removing all of the background events is presented in Tables 4.6 and 4.7. Of the types of background event

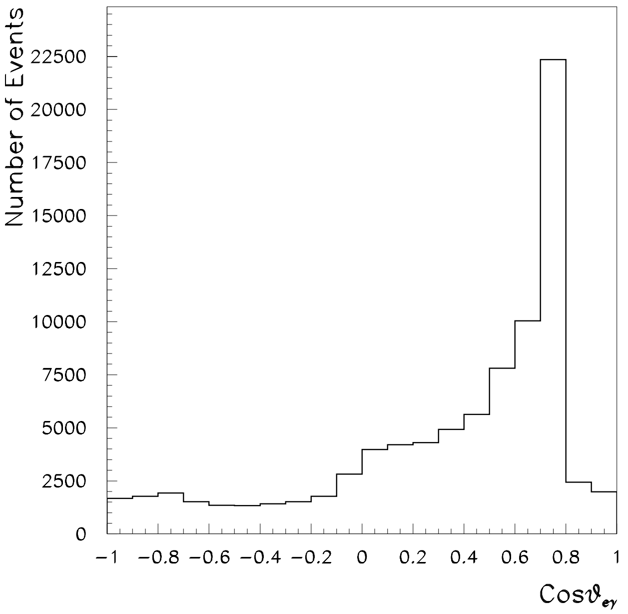

Figure 4.5: The distribution of cos$\theta_{e\gamma}$ in the CM frame.

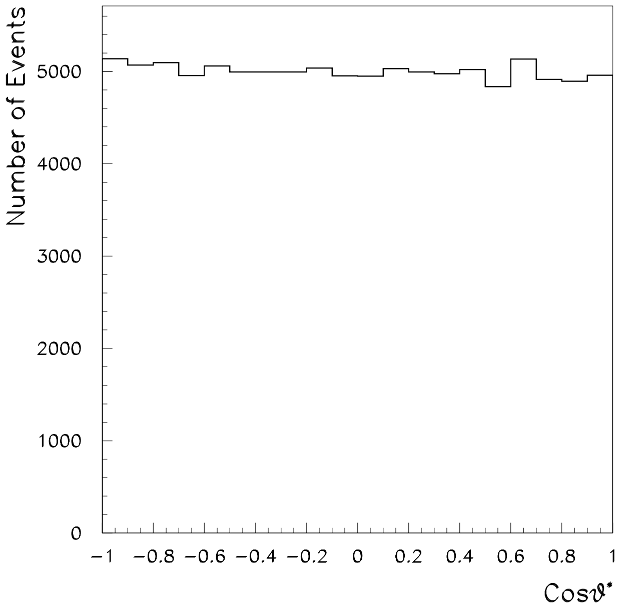

Figure 4.6: The distribution of the decay angle cosθ^{*}.

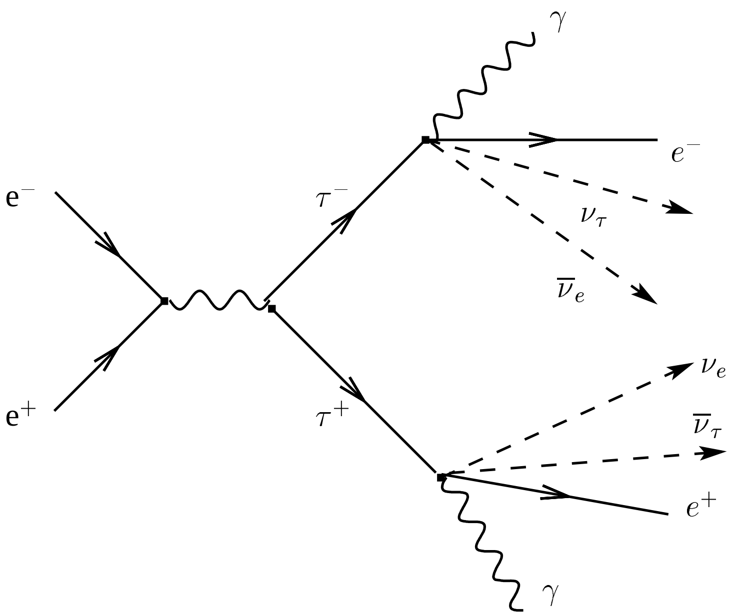

Figure 4.7: A decay of a τ-pair, each decaying leptonically to $\tau^- \to e^-\ \nu_\tau\ \overline{\nu}_e$ and $\tau^+ \to e^+\ \overline{\nu}_\tau\ \nu_e$. If the τ-decays include photons, as shown, then they are potential backgrounds to the $e\gamma$-system.

considered three can closely mimic the signal: SM τ-decays that include an electron, two-photon events and radiative Bhabha events. These three sources of background event are described in detail.

One of the decay channels for τ-leptons includes an electron, i.e. $\tau^- \to e^-\ \nu_\tau\ \overline{\nu}_e$ and $\tau^+ \to e^+\ \overline{\nu}_\tau\ \nu_e$ (Fig. 4.7). If the electron radiates a photon it can be mistaken as an $e\gamma$-signal event should the neutrinos have very low momentum.

The tree-level diagram for the two-photon background in which a pair of leptons, e^+e^-, $\mu^+\mu^-$ or $\tau^+\tau^-$, are produced is shown in Fig. 4.8. In the case of e^+e^- if one of them radiates a photon and the other is not reconstructed, e.g. if it has gone into part of the detector where it cannot be seen, then this event could mimic the $e\gamma$-signal. Both $\mu^+\mu^-$ and $\tau^+\tau^-$ can decay via a modes that include an electron or positron, one of which may radiate a photon and again may simulate the $e\gamma$-signal. This process has a cross-section of 1 nb.

The collider produces copious numbers of Bhabha ($e^+e^- \to e^+e^-$) events and those that also radiate a photon can mimic the $e\gamma$-signal (4.9). The cross-section for Bhabha events is approximately 5.1 nb (Table 4.1) which is very large when compared to 0.89 nb for the production of τ-pairs. For these reasons Bhabha events are a difficult background to remove.

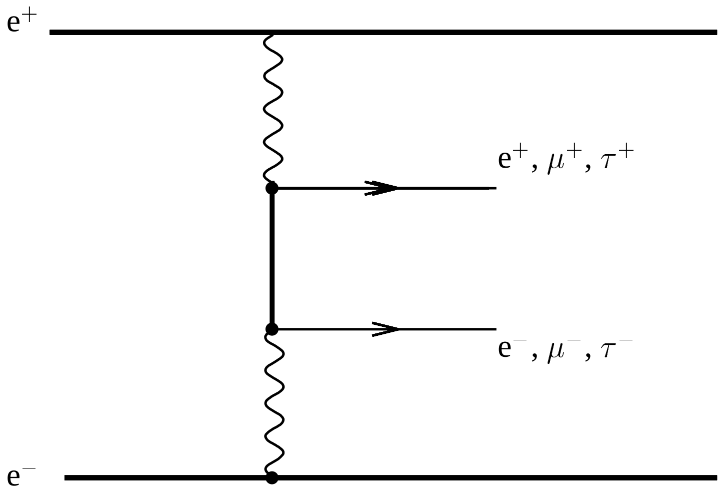

Figure 4.8: Feynman diagram for two-photon event producing pairs of leptons.

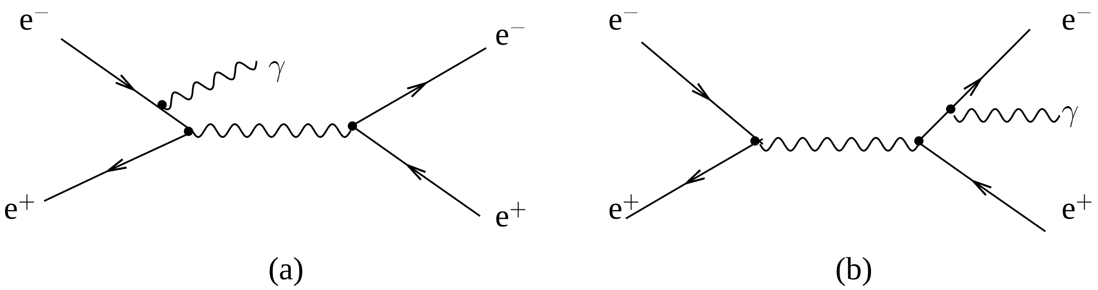

Figure 4.9: Two Feynman diagrams for radiative Bhabhas: (a) is referred to as initial state radiation; (b) as final state radiation.

4.5 Outline of event selection

The method of selecting events begins with a comparison of the samples of simulated background events and a sample of simulated signal events. From the comparison, cuts are defined and applied to both the simulated backgrounds and signal with the objective to reduce the backgrounds to a minimum whilst simulataneously maximising the signal. Once all of the cuts have been made, the events that remain are used to estimate the signal efficiency ϵ and the number of expected background events b.

The *BABAR* detector has an acceptance in θ between 20^{o} and 142^{o}, in the LAB frame. The cross-section for the production of Bhabha events within this region is $5.1\,\mathrm{nb}$ at the $\Upsilon(4S)$ resonance (Table 4.5), i.e. a factor of about six greater than the cross-section of $0.89\,\mathrm{nb}$ for τ-pair production. In principle a sample of simulated Bhabha events significantly larger than the size of the data set is required so that the statistical error on the sample of simulated events is less than the statistical error on the data. This is impracticable with the computing resources available and a different approach is required.

The sample of simulated signal events is compared with a sample of real data (“data control sample”) instead of the samples of simulated backgrounds; 17% of the total data set is used for the data control sample. In establishing the general analysis technique, the following considerations were made:

- distributions of variables upon which cuts are made must exhibit discrimination between background and signal, thus minimising the loss of potential signal events;
- a blind analysis method [45] is followed for the remaining 83% of the experimental data and the two data samples are added together, thus making maximum use of the full data set;
- the behaviour of the backgrounds is mapped with an interpolating function from which an estimate of the expected number of background events in the signal region b is made;
- the efficiency ϵ for detecting signal events is determined from the simulated signal sample.

Although samples of simulated backgrounds are not used to provide the estimate for the expected number of background events b they are still an important source of information. They are used in the analysis to aid exploration of each cut and show which particular background it is targeting. Since the number of simulated Bhabhas available is still insufficient even for this limited role a sample of Bhabhas is obtained from the data. An estimate for b can be obtained by applying the entire analysis to the set of samples of simulated backgrounds plus the sample of Bhabhas to act as a cross-check on the estimate determined from the data. The samples of simulated events analysed were SM $e^+e^- \to \tau^+\tau^-$ events, di-muon $e^+e^- \to \mu^+\mu^-$ events, $e^+e^- \to h^+h^-$ events (h = u, d, s, b, c) and two-photon events (Table 4.5). For completeness $B\overline{B}$ decays were also considered but none survive the preselection.

The SM τ-events studied were generated with `KK2f` and decayed with `TAUOLA` [44]. The QED radiative corrections are modelled with the software package PHOTOS [46]. The simulation of the *BABAR* detector was carried out by using GEANT4 [47].

Table 4.3: Production cross-sections at $\sqrt{s} = M(\Upsilon(4S))$ for samples of simulated backgrounds used in $\tau \to e\gamma$ analysis. Studies were carried out using samples of simulated backgrounds generated for use with the data that included all three runs as described in chapter 3. The SM τ events studied were generated with `KK2f` decayed with `TAUOLA` and the radiative corrections modelled with PHOTOS.

$e^+e^- \to$	cross-section (nb)	Number of events	Effective integrated luminosity (fb^{-1})
$\tau^+\tau^-$	0.89	157×10^6	176
$u\bar{u}, d\bar{d}, s\bar{s}$	1.39, 0.35, 0.35	300×10^6	143
$c\bar{c}$	1.30	186×10^6	143
Bhabha: $e^+e^- \to e^+e^-(20 - 142^\circ)$	5.1	5×10^6	25.5
$\mu^+\mu^-$	1.16	97×10^6	83
Two-photon	1.0	5×10^6	5.0
B^+B^-	0.535	220×10^6	412
$B^0\overline{B}^0$	0.535	246×10^6	459

Once the overall strategy has been decided the next step is to carry out a process of selecting events in such a way that maximises the chance of finding signal events whilst suppressing all the possible backgrounds especially those that might mimic the signal. The first stage of the event selection process, the preselection, is described next.

4.6 Preselection

The preselection has three steps and each is discussed individually and summarised at the conclusion of this section. The first step is to decide on the criteria to use to identify good charged tracks as this is vital for finding events with a 1-1 topology. Similarly to be able to select signal events it is neccessary to be able to select neutrals and identify electrons. The second step in the preselection is to identify τ-decays and seperate them from all the other events produced in the detector, especially Bhabhas. The third step is demanding that only one of the charged tracks in the event is idenfied as an electron as this will make up one part of the $e\gamma$-signal and also suppress Bhabha events.

4.6.1 Charged tracks

The number of charged tracks is the key to identifying τ-decays, therefore a decision about the quality of the charged tracks [48] is made early in the analysis. The quality of each track is graded using four criteria:

- The angle, θ, of the charged track with respect to the beam line is required to be in the range $0.41 < \theta < 2.54$ radians, these two angles are used to make sure the track falls within the bounds of the EMC;
- The magnitude of the momentum vector of each track $|\vec{P}| < 10$ GeV in the LAB frame, due to the constraints of the energy of the beams there can not be any charged particle with momemtum higher than this;
- The distance between the origin of the track and the IP in the XY-plane must be < 1.5 cm;
- The absolute value of the distance between the origin of the track and the IP along the z-axis must be < 10 cm. The position of the IP can not be known exactly but only events where the tracks begin within a reasonable distance of the IP in all three axes are accepted;.

A typical signal event has to have two charged particles (1-1 topology) of opposite charge. Therefore each event has to have two and only two charged tracks satisfying the above criteria and the sum of their charges must equal zero.

4.6.2 Neutral Particle Selection

Neutral selection begins by searching for local maxima of energy depositions, called clusters, in the EMC which are not matched with a track. These clusters typically consist of several neighbouring crystals in which energy has been deposited. As they are assumed to come from photons originating from the beam spot, angles and momenta are assigned accordingly. However, a large fraction of the low energy EMC clusters arises from beam backgrounds and hadronic interactions. These can be reduced by requiring specific criteria on the cluster shape to be fulfilled. A very useful variable in this respect is the lateral moment LAT of a shower, which is defined as

$$LAT = \frac{\sum_{i=3}^{N} E_i r_i^2}{\sum_{i=3}^{N} E_i r_i^2 + E_1 r_0^2 + E_2 r_0^2}. \tag{4.2}$$

Here N is the number of crystals belonging to the cluster, E_i are the corresponding energies in descending order, the r_i are the distances of crystal i to the cluster centre and r_0 is the average distance between two crystals, approximately 5 cm for the *BABAR* calorimeter. The lateral moment has low values for electromagnetic showers as most of the energy of a particle is deposited in a few crystals. In contrast, hadronic showers tend to deposit their energy in a larger number of crystals, thereby resulting in higher values. This effect is enhanced by omitting the two crystals with the highest energy deposits in the numerator and by multiplying with the squared distances from the shower centre. Photons stemming from beam background are mainly eliminated by requiring a minimum energy for the cluster.

To account for inefficiencies in the track-cluster matching algorithm, clusters which are close to a charged track but not matched to it are removed to avoid double counting of energies. For this purpose the variable $\Delta\alpha = \sqrt{\Delta\phi^2 + \Delta\theta^2}$ is introduced, where $\Delta\phi$ and $\Delta\theta$ are the differences in azimuthal and polar angle between the cluster candidate and the nearest charged track in the laboratory frame, respectively. All clusters have to be fully contained within the acceptance of the EMC, therefore only clusters within a restricted polar angle θ range are considered.

After all these considerations the following selection criteria for neutral clusters are applied:

- minimum raw energy, $E_{\mathrm{raw}} > 0.05\ \mathrm{GeV}$;

- number of crystals, $N_{\rm cry} > 2$;
- angular acceptance, $0.320\ {\rm rad} < \theta < 2.444\ {\rm rad}$;
- lateral moment, $LAT < 0.5$;
- track-cluster separation, $\Delta\alpha > 0.2\ {\rm rad}$.

4.6.3 Identification of electrons

One of the most important aspects of the analysis is to identify one of the charged particles as an electron with very high probability. To this end the standard *BABAR* electron particle identification algorithm (PID) [49] is used. To identify the signal track as an electron it has to satisfy the following criteria:

- dE/dx is within 500 and 1000 (measured in arbitrary units (Fig. 3.10));
- at least 3 crystals in the EMC are illuminated;
- the ratio E/p should be between 0.75 and 1.0 (because the electron produces an electromagnetic shower it should deposit all of its energy into the EMC; therefore E/p ought to be of the order unity);
- lateral moment: $LAT < 0.6$.

Conversely the other charged track in the event needs to be identified as not an electron. Therefore it does not meet this criteria (electron veto).

There is a difference between the data and the simulated events for the efficiency of the electron identification algorithm; for the simulated events the efficiency is at the level of 99.0±0.01$\%$, with a systematic error of 1.0 $\%$. In this analysis only a sample of simulated signal events is used for setting the cuts and estimating the signal efficiency. Therefore this very small inefficiency of the electron identification algorithm has to be taken into account.

4.6.4 Background filter for selecting τ-decays

All data events produced by the collider have to pass the criteria of both levels of the trigger (L1 and L3) before being recorded. The data is then divided into six categories by using a set of six software filters. Each event is tagged if it meets the criteria set by one or more of the filters. One filter is designed to specifically select τ-decays [42] with a 1-1 topology whilst simultaneously reducing the number of Bhabha events. The criteria used by this filter are as follows:

- There must be at least two or good tracks in the event, although there can be more than two. Events with a higher number of charged tracks are not rejected, so 1-3 and 1-5 topologies are not excluded at this early stage and the option is open to use them in the analysis. The efficiency of the τ-filter for selecting events with a 1-3 topology is very low (0.23%) as the filter is designed for selecting events with a 1-1 topology. To improve the efficiency another filter would have to be used to find events with the required number of charged tracks. This filter is designed for seeking hadronic events with three or more charged tracks and would greatly increase the number of hadronic background events. This would require a totally separate analysis. Therefore it was decided not to include these events and they were discarded by accepting events with only two charged tracks.

- In a typical Bhabha event the electron will have most if not all of the available momentum. Therefore the sum of the magnitudes of the momenta of the two charged particles in the CM frame is restricted by requiring

$$|\vec{P}_1| + |\vec{P}_2| < 9\,\text{GeV}. \tag{4.3}$$

- In a typical τ-decay there is missing energy and photons as well as the charged particles. Therefore the energy of one of the charged particles should have roughly half the available energy whereas in a Bhabha event the charged particle will carry almost all of it. Thus the sum of the energies of the two particles is restricted, i.e.

$$|E_1| + |E_2| < 5\,\text{GeV}. \tag{4.4}$$

- For an electron, the ratio of its energy deposited in the EMC to the magnitude of its momentum should be approximately unity. This ratio is calculated for each of the charged particles in the event and one has to be greater than 0.8 and the other less than 0.8 to help reduce the number of Bhabha events.

- The tracks of the two electrons in the majority of the Bhabha events produced will be close to being back to back. Therefore the modulus of the transverse component of the vector sum of the momenta of the two electrons will be small compared with the available energy from the beam. Thus the minimum of the ratio is restricted, i.e.

$$\frac{|\vec{P}_1 + \vec{P}_2|_T}{E_{\mathrm{beam}} - |\vec{P}_1| - |\vec{P}_2|} < 0.7. \tag{4.5}$$

These criteria make up what is referred to as the τ-filter and represents the first step in separating τ-decays from other types of event and to reduce the number of Bhabha events in the data set used for this analysis.

4.6.5 Summary of the preselection

The preselection is the cumulative affect of the trigger, the τ-filter, only allowing events with two charged tracks whose charges sum to zero and one track being identified as an electron. These cuts had the combined effect of reducing the size of the data control sample to 593,401 events.

The effect of the preselection on the sample of simulated signal events and the samples of simulated backgrounds is summarised in Tables 4.4 and 4.5. The cuts are applied sequentially and the table shows the cumulative reduction in each sample. The backgrounds due to $B\overline{B}$ decays did not survive the preselection cuts. Therefore the preselection has reduced the data set to mostly τ-decays and it has been very successful in minimising the number of Bhabhas. A further set of cuts are described and discussed in the next section.

4.7 Selection cuts

Further selection cuts are imposed to reduce the backgrounds to an acceptable level. The cuts are applied to seven variables that fall into two categories; those relating to the whole event and those relating to the the signal side only. The placement of each each cut is set by maximising the ratio of the number of signal events to the square root of the number of signal plus background events. It is found that the value of this ratio does not depend very sensitively on the value of the cut. Distributions are shown for each variable upon

Table 4.4: The effect of the preselection on $e\gamma$-signal and leptonic and two-photon backgrounds. The cuts are applied sequentially and the table shows the cumulative reduction in each sample.

Sample	$e\gamma$-signal(%)	$\tau\tau$-All (%)	$\mu^+\mu^-$ (%)	two-photon (%)	Bhabha (%)
Trigger	89.56	84.46	74.98	83.52	33.44
τ-filter	33.24	37.00	6.05	1.4	2.47
2 tracks +zero charge	32.10	34.83	5.85	1.1	2.17
e-PID/veto	18.73	10.81	0.03	0.01	0.11

Table 4.5: The effect of the preselection on the hadronic backgrounds.

Sample	$B\overline{B}$ (%)	$c\bar{c}$ (%)	uds (%)
Trigger	99.92	98.92	95.68
τ-filter	0.23	1.16	2.92
2 tracks+zero charge	0.12	0.72	1.2
e-pid/veto	0.00	0.05	0.02

which cuts are made for four different samples: (a) simulated signal, (b) data control sample, (c) Bhabha sample and (d) a luminosity-weighted mixture of backgrounds. The value of each cut is shown by a dashed line and the region containing the events being retained is indicated by one or more arrows. At this stage there is no restriction on the number of photons in the event. The last three cuts are designed to reduce the number of photons is the signal hemisphere to one so that when the invariant mass of the $e\gamma$-system is calculated there is only one possible electron-photon pair.

A description and value of each cut follows:

- In Section 4.2 the magnitude of the thrust T is defined for each event. The distribution of T for the signal shows a peak between 0.85 and 0.96 (Fig. 4.10(a)). A clear asymmetry can be observed between the distributions of the signal and the data at high values of the thrust magnitude (Fig. 4.10(b)). The data has a peak at values close to 1.0 which is confirmed by the Bhabha control sample (Fig. 4.10(a)). Therefore cuts are made at $0.85 < T < 0.96$.

- In a typical signal event the missing energy will only be present in the non-signal

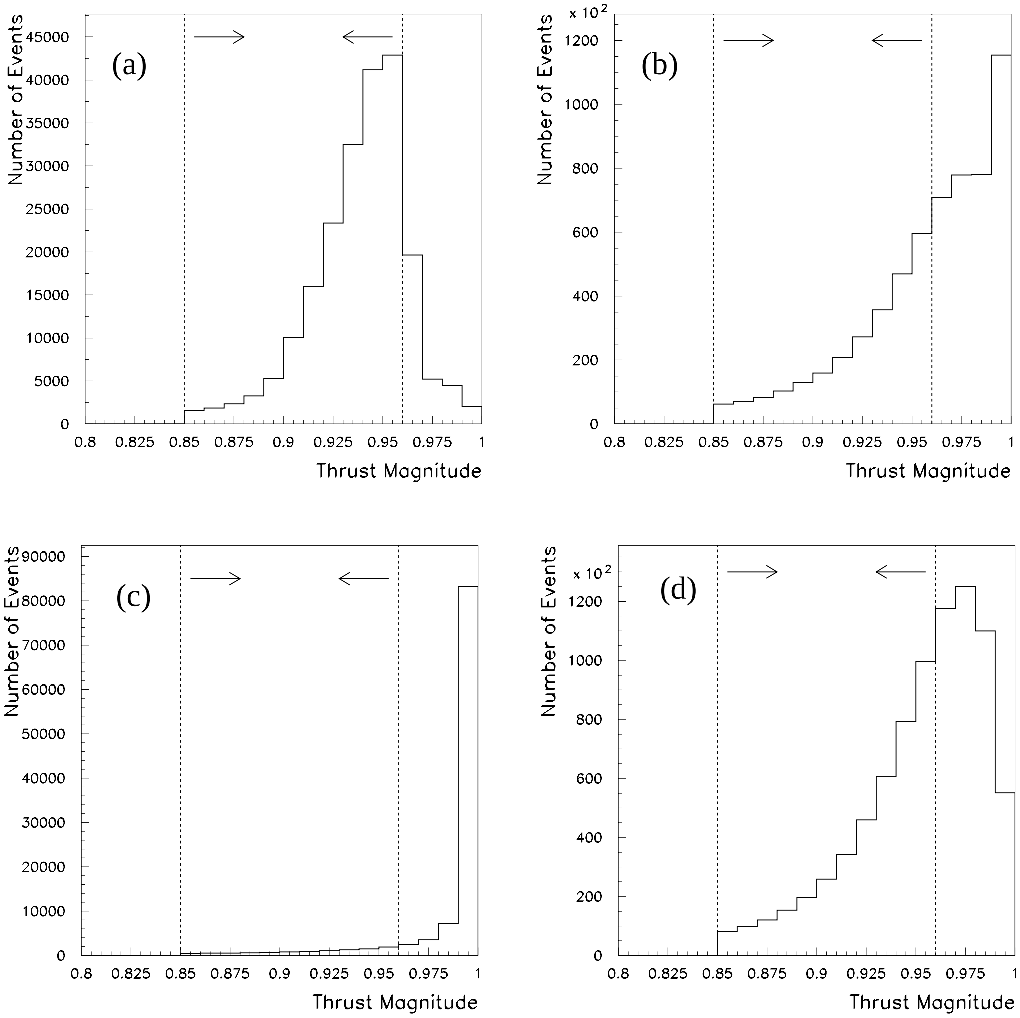

Figure 4.10: Distributions of the thrust magnitude for (a) sample of simulated signal, (b) data control sample, (c) Bhabha control sample and (d) samples of simulated background events, not including Bhabhas. The background is dominated by SM τ-decays and Bhabha events. The events retained are indicated by the arrows in the region $0.85 < T < 0.96$ between the dashed lines, where T is the magnitude of the thrust.

hemisphere, due to the emission of neutrinos. Conversely in a typical SM τ-event there will be missing energy on both sides, resulting in a much higher missing energy (Fig. 4.11(d)). Therefore a cut is applied at $E_{\rm miss} < 5$ GeV, where $E_{\rm miss}$ is the missing energy in the event (Fig. 4.11).

- In a typical signal event the track on the non-signal side and the missing momentum vector ought to be within the same hemisphere. Therefore there ought to be a clear asymmetry in the distribution of the cosine of the angle between the missing momentum vector and the non-signal track, $\cos\theta_{\rm miss}$, for the $e\gamma$-signal weighted towards angles of less than 90^o (Fig. 4.12(a)). On the converse the data has a peak at angles greater than 90^o (Fig. 4.12(b)), which is due mainly to SM τ-decays (Fig. 4.12(d)). There is also a small peak close to 90^o which is due to Bhabha events (Fig. 4.12(c)). Therefore we require $0.4 < \cos\theta_{\rm miss} < 0.988$, where $\theta_{\rm miss}$ is the angle between the non-signal track and the missing momentum vector. The lower cut is aimed at SM τ-decays and the upper cut is aimed at Bhabha events.

- Many Bhabha events are characterised by the particle tracks having a low transverse momentum, (Fig. 4.13(c)), and this can be clearly seen in the data, (Fig. 4.13(b)). Therefore the cut $P_T > 0.5$ GeV is introduced, where P_T is the total transverse momentum, (Fig. 4.13).

- The angle between the signal track and the photon $\theta_{e\gamma}$ is required to satisfy $0.3 < \cos\theta_{e\gamma} < 0.8$. Due to the kinematics of the signal event (two-body decay (Section 4.3)), $\cos\theta_{e\gamma}$ cannot be greater than 0.8. Therefore the events with larger values shown in the sample of simulated signal plot are due to excess photons, (Fig. 4.14(a)). The lower cut at 0.3 is meant to eliminate photons produced by bremsstrahlung radiation from the signal particle, (Fig. 4.14). both cuts are aimed at Bhabha events and SM τ-decays (Fig. 4.14(c) and (d)).

- The response of the EMC is less reliably modelled for low photon energies. Therefore a cut is introduced $E_\gamma > 0.4$ GeV, where E_γ is the energy of the photons in the signal hemisphere, (Fig. 4.15). the cut is aimed equally at Bhabha and SM τ-decays, (Fig. 4.15(c) and (d)), although the main purpose is to reduce the number of photons in the signal hemisphere.

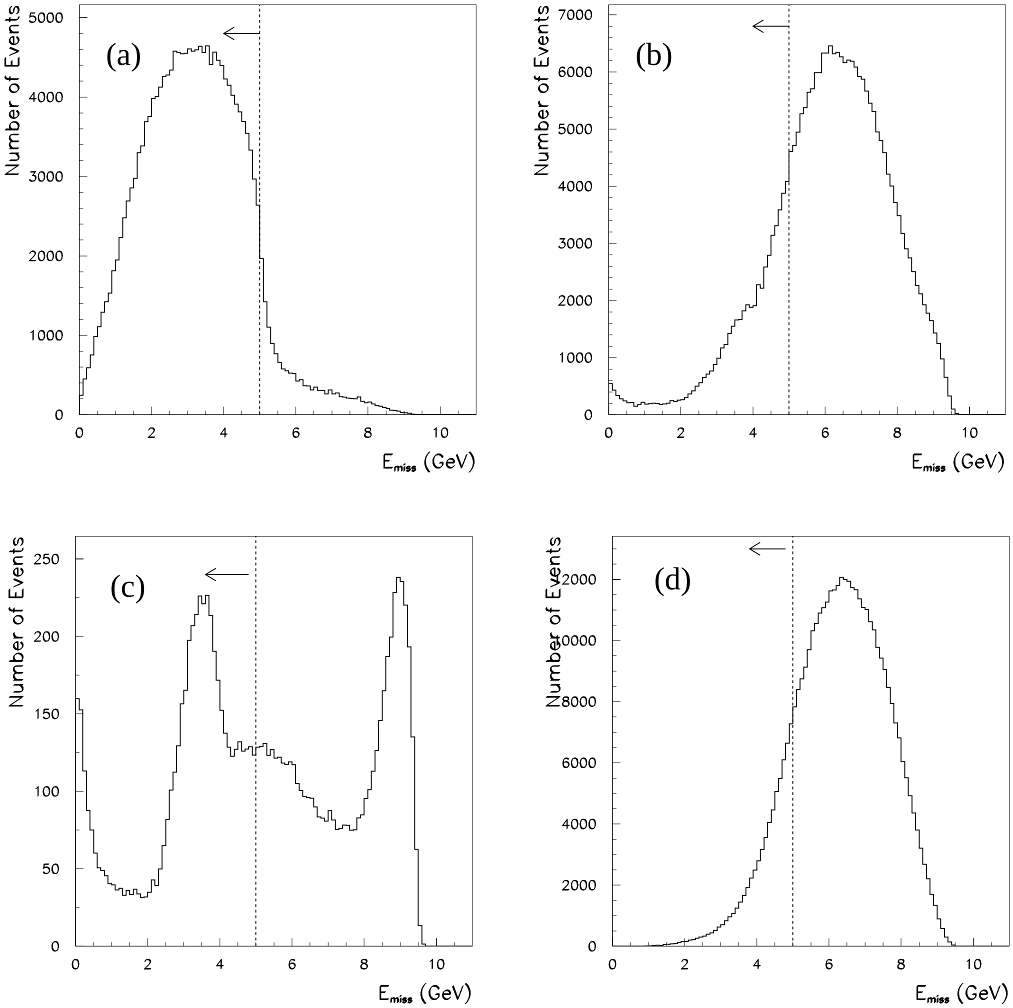

Figure 4.11: Missing energy distributions for (a) sample of simulated signal, (b) data control sample, (c) Bhabha control sample and (d) samples of simulated background events, not including Bhabhas. The background is dominated by SM τ-decays and bhabhas. The events retained are indicated by the arrow in the region $E_{\rm miss} < 5$ GeV to the left of the dashed line, where $E_{\rm miss}$ is the missing energy in the event.

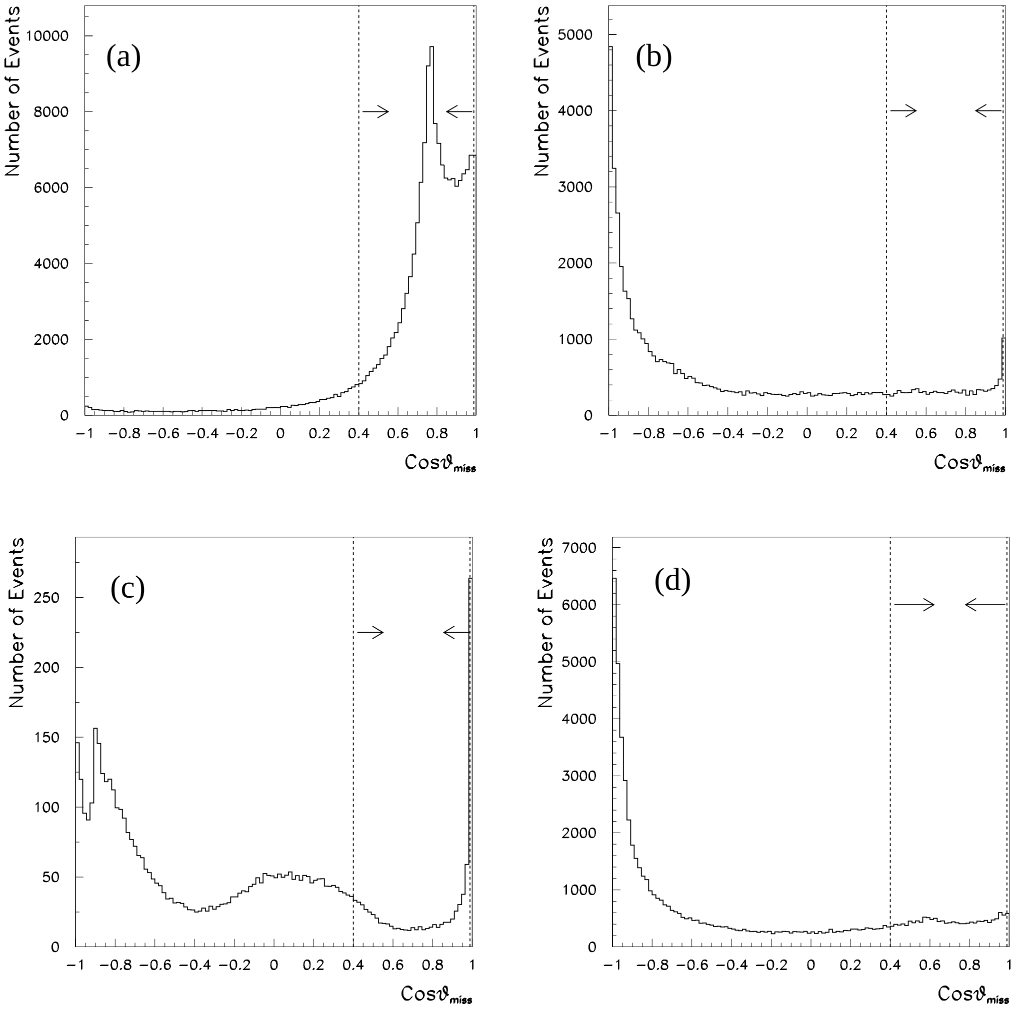

Figure 4.12: Distributions of the cosine of the angle between the missing momentum vector and the non-signal track for (a) sample of simulated signal, (b) data control sample, (c) Bhabha control sample and (d) samples of simulated background events, not including Bhabhas. The background is dominated by SM τ-decays and Bhabha events. The events retained are indicated by the arrows in the region $0.4 < \cos\theta_{\rm miss} < 0.988$ between the dashed lines, where $\theta_{\rm miss}$ is the angle between the non-signal track and the missing momentum vector.

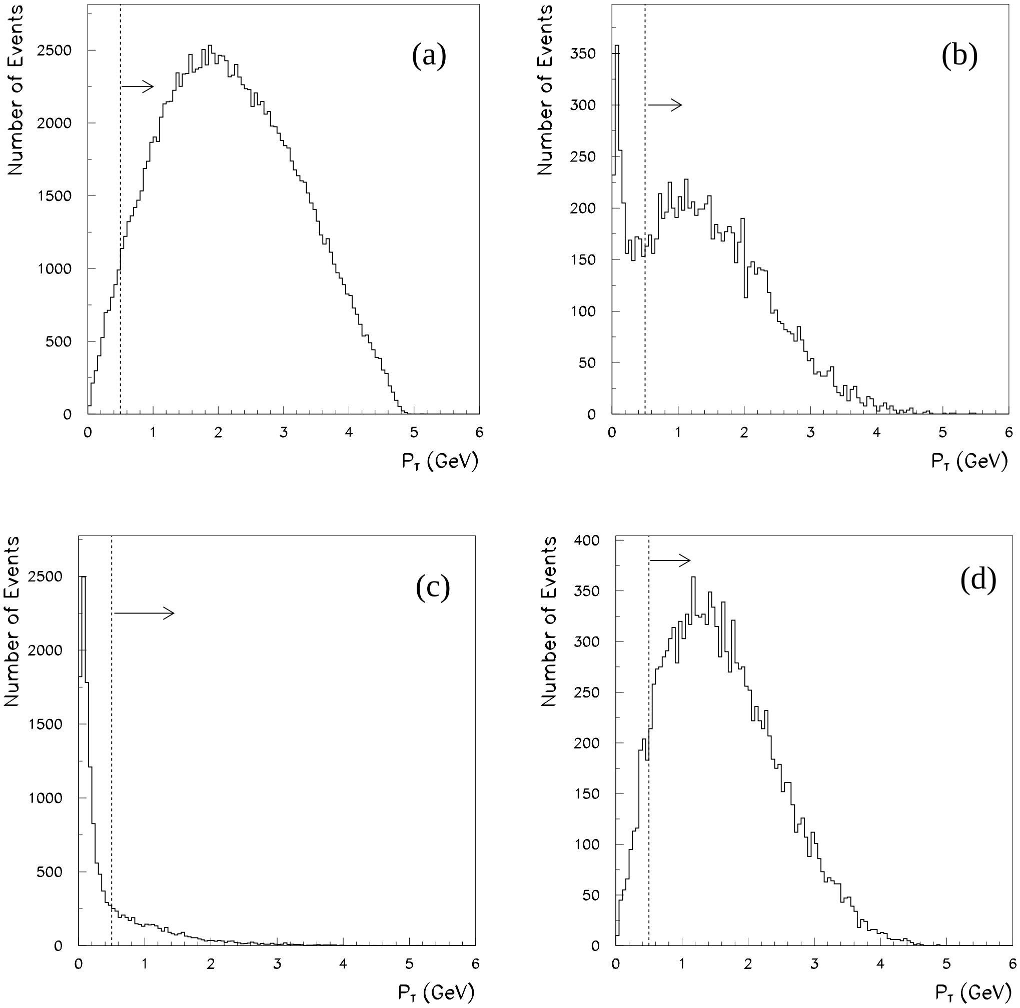

Figure 4.13: Distributions of the total transverse momentum for (a) sample of simulated signal, (b) data control sample, (c) Bhabha control sample and (d) samples of simulated background events, not including Bhabhas. The background is dominated by SM τ-decays and Bhabha events and all other backgrounds have been removed.. The events retained are indicated by the arrow in the region $P_T > 0.5$ GeV to the right of the dashed line, where P_T is the total transverse momentum.

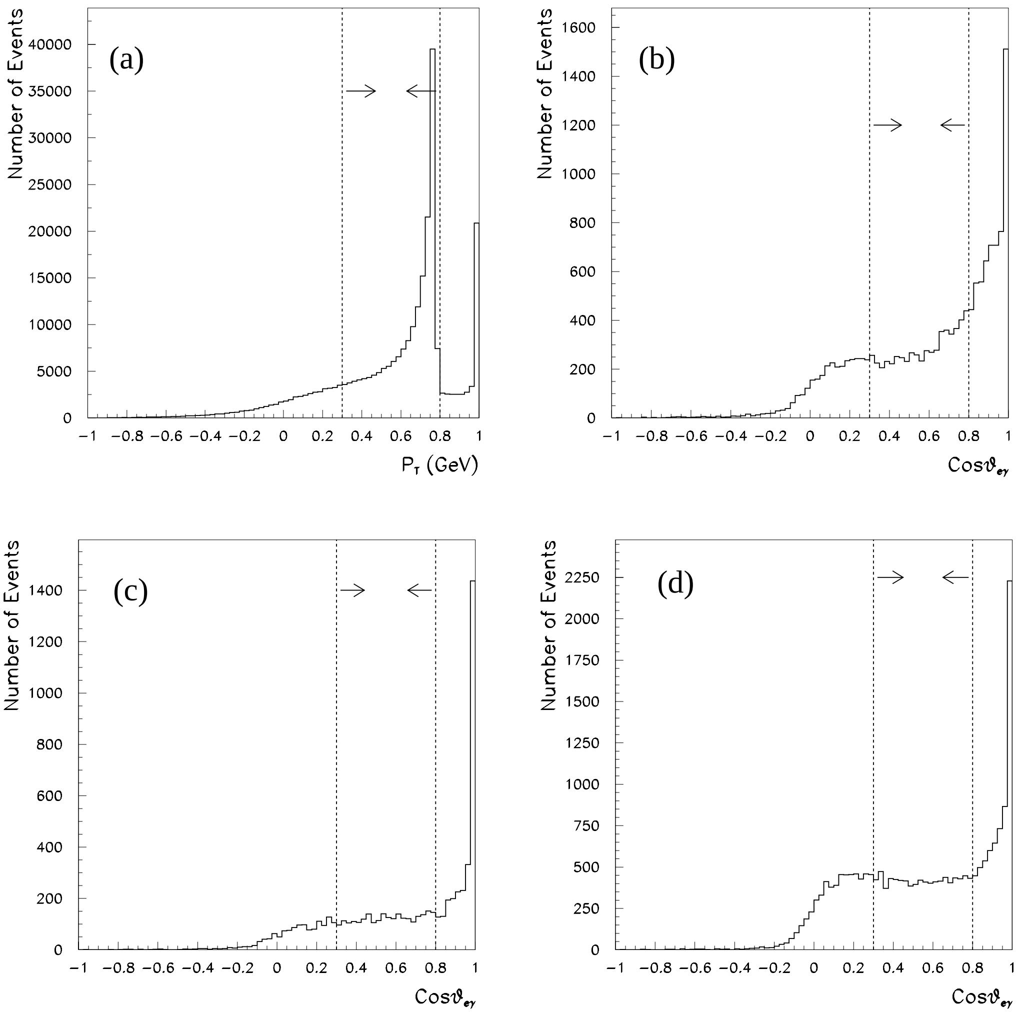

Figure 4.14: Distributions of the cosine of the angle between the signal track and any photon on the signal side of the event for (a) sample of simulated signal, (b) data control sample, (c) Bhabha control sample and (d) samples of simulated background events, not including Bhabhas. The events retained are indicated by the arrows in the region $0.3 < \cos\theta_{e\gamma} < 0.8$ between the dashed lines, where $\theta_{e\gamma}$ is the angle between the signal track and the photon.

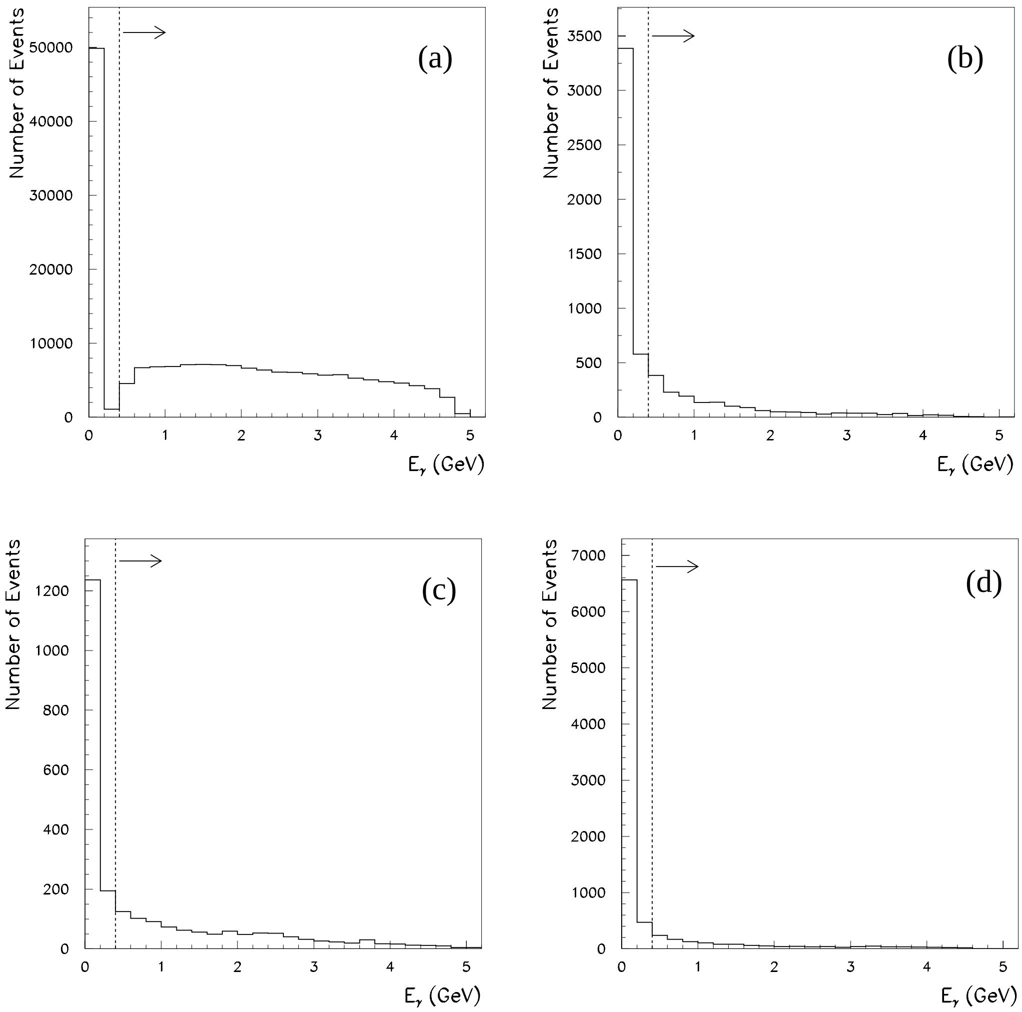

Figure 4.15: Distributions of the photon energy in the signal hemisphere for (a) sample of simulated signal, (b) data control sample, (c) Bhabha control sample and (d) samples of simulated background events, not including Bhabhas. The events retained are indicated by the arrow in the region $E_\gamma > 0.4$ GeV to the right of the dashed line, where E_γ is the energy of the photons in the signal hemisphere.

- For some events the number of photons on the signal side is greater than one. The signal hemisphere should only have one photon. Therefore events with only one photon in the signal hemisphere are retained.

The efficiencies resulting from the application of each the cut on the data and the sample of simulated signal is summarised in Table 4.6. The background is dominated by Bhabha events and SM τ-decays as the other types of background that were considered did not survive the cuts. The efficiencies are summarised in Table 4.7.

Table 4.6: Cut flow for the signal and the data control sample.

Cut	Cut Range	Signal	Signal Eff(%)	Data Control Sample	MC-samples + Bhabhas
preselection	-	211745	19.2	593401	580753
T	0.85 - 0.96	180375	16.4	251218	288127
E_{miss}	5 GeV	164850	15.0	56528	52394
$\cos\theta_{\text{miss}}$	0.4 - 0.988	143672	13.1	10321	10740
P_T	0.5 GeV	138078	12.6	8301	8329
Cuts on signal side					
$\cos\theta_{e\gamma}$	0.3 - 0.8	130575	11.9	5722	5737
E_γ	0.4 GeV	125436	11.4	1755	1799
N_γ	=1	124578	11.3	1019	1055

The fraction of signal events remaining after the cuts is 11.3$\%$. As discussed in Section 4.5 for signal events the invariant mass of the $e\gamma$-system must be equal to the τ-mass, i.e., 1.777 GeV, and its energy must equal the energy of the beam, i.e., 5.28 GeV. It is convenient to represent these two variables on a two dimensional plane of invariant mass ($M_{e\gamma}$) and energy ($E_{e\gamma}$) (Fig.4.3). This plane is used to specify the exact region where the $e\gamma$-signal is to be expected, the signal region, and also the side-band used for estimating the number of background events within the signal region. The method for defining the dimensions of these two regions and how the estimate is made is described in the next chapter.

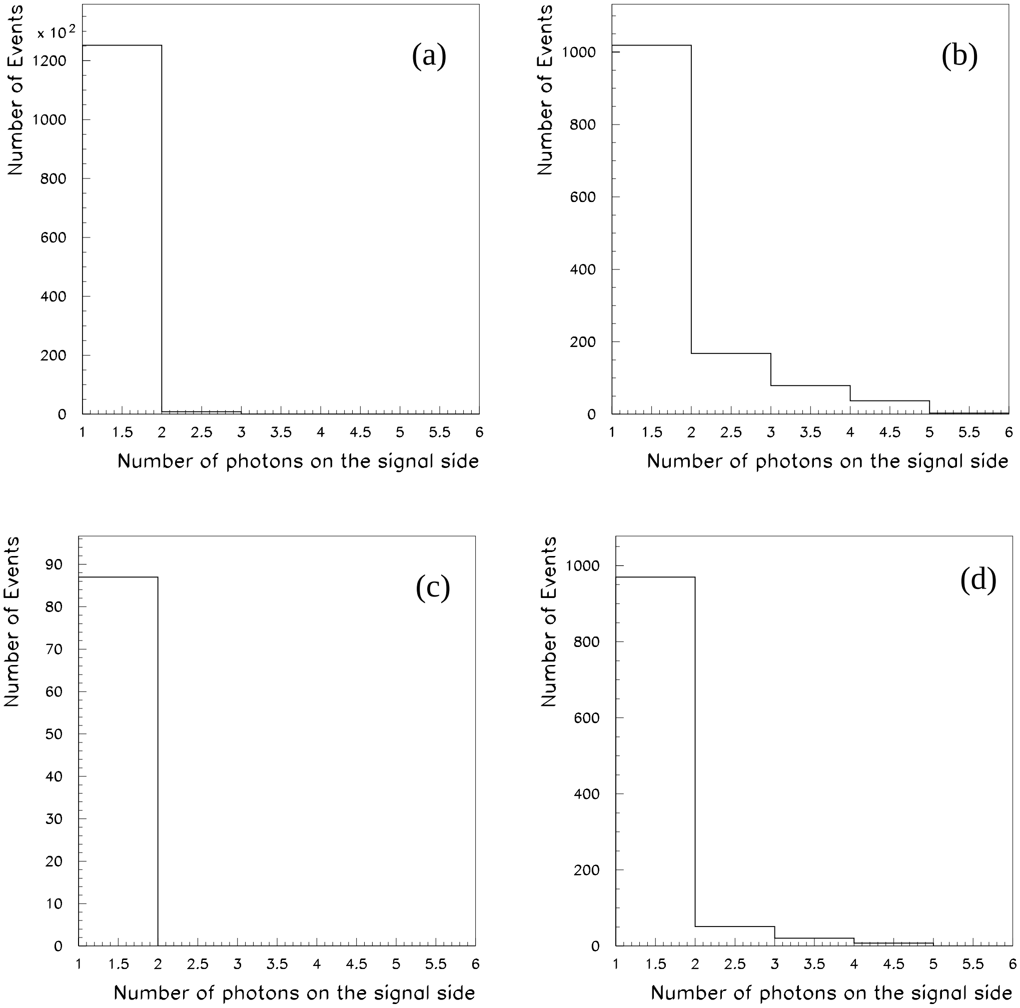

Figure 4.16: Distributions of the number of photons in the signal hemisphere for (a) sample of simulated signal, (b) data control sample, (c) Bhabha control sample and (d) samples of simulated background events, not including Bhabhas. The events retained are those events with a single photon.

Table 4.7: The number of events left after each cut on backgrounds; udsbar, ccbar, two-photon and di-muon. The samples have been luminosity weighted to 21.1fb^{-1}.

Cut	Cut Range	$\tau\tau$-All	Bhabha	uds	$c\overline{c}$	Two photon	$\mu^+\mu^-$
preselection	-	548356	29076	772	1535	211	803
T	0.85 - 0.96	275136	10347	648	1517	140	339
E_{miss}	5 GeV	45121	5477	534	1045	0	217
$\cos\theta_{\text{miss}}$	0.4 - 0.988	9696	714	134	196	0	0
P_T	0.5 GeV	7993	336	0	0	0	0
Cuts on signal side							
$\cos\theta_{e\gamma}$	0.3 - 0.8	5615	152	0	0	0	0
E_γ	0.4 GeV	1677	122	0	0	0	0
N_γ	=1	968	87	0	0	0	0

Chapter 5

Signal and background estimation

To determine if the data contain any $\tau \to e\gamma$ events it is necessary to subtract any backgrounds that are still present after the event selection process. In Chapter 4 a two dimensional plane of the invariant mass and the total energy of the $e\gamma$-candidate ($M_{e\gamma}$, $E_{e\gamma}$) was defined. On this plane (Fig. 4.3) the $e\gamma$-signal is concentrated in the region about the point specified by the τ-mass M_τ and the beam-energy E_{beam} (1.777 GeV, 5.28 GeV) in the CM. On the other hand the backgrounds are spread across the plane (Fig. 5.1). Therefore the region containing the $e\gamma$-signal also contains a number of background events b.

This chapter proceeds with a description of the method used to define the size of the region containing the concentration of the $e\gamma$-signal. This region will be called the signal box due to its shape. Then an estimate of the number of background events b remaining within this region is obtained. The procedure for estimating b requires us to define a second region called the sideband, surrounding the signal box.

The size of the signal box is determined according to criteria discussed in Section 5.3. Although b is estimated from the sideband using real data, a cross-check on b is also carried out using simulated background events. Statistical and systematic errors are estimated for ϵ and b. Finally the signal box for the full data set is unblinded to see if there is any evidence for the decay $\tau \to e\gamma$.

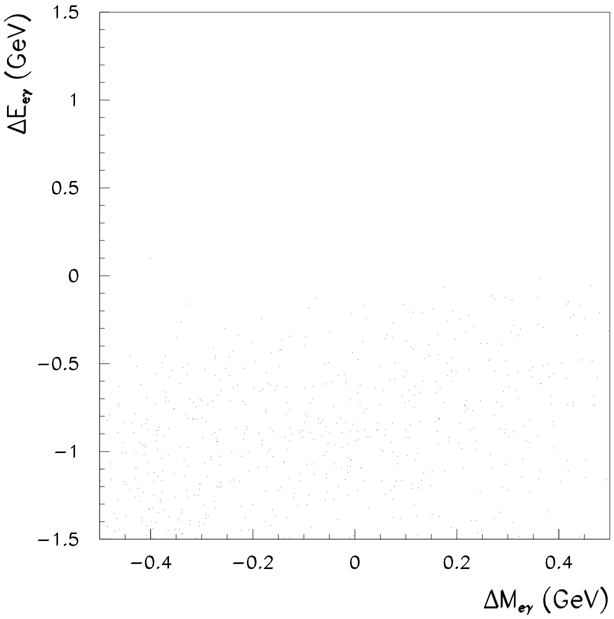

Figure 5.1: Two dimensional distribution (ΔM, ΔE) for the simulated background events. The events are spread across the part of the plane below the beam energy.

5.1 Procedure for defining the signal box and sideband

First for convenience the axes of the two dimensional plane ($M_{e\gamma}$, $E_{e\gamma}$) are transformed to the new kinematic variables ΔM and ΔE, where ΔM = $M_{e\gamma} - M_\tau$ and $\Delta E = E_{e\gamma} - E_{\text{beam}}$ (Fig. 5.2). The $e\gamma$-signal is now expected to be concentrated around $\Delta E = 0$, $\Delta M = 0$. However, the occurrence of initial (ISR) and final state radiation (FSR) from the beam particles, bremsstrahlung from the final state particles and measurement errors in the detector produces a tail in both the mass and energy distributions (Fig. 5.3). This causes the majority of the events to lie on a diagonal with respect to the two axes. Therefore it is difficult to define an optimal signal box in the (ΔM, ΔE) plane around the signal region in order to maximise the number of selected signal events (Fig. 5.2) contained within the box.

By rotating the ΔM, ΔE distribution to new axes η and ξ, the $e\gamma$-signal lies horizontally with respect to η and perpendicular to ξ (Fig. 5.4). The general transformation is,

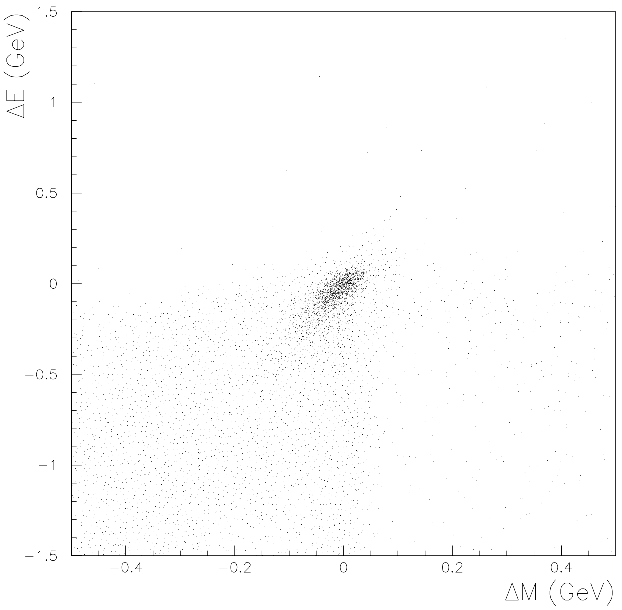

Figure 5.2: Two dimensional distribution (ΔM, ΔE) for the sample of simulated signal events. The majority of the $e\gamma$-signal is concentrated about $\Delta M = 0$, $\Delta E = 0$.

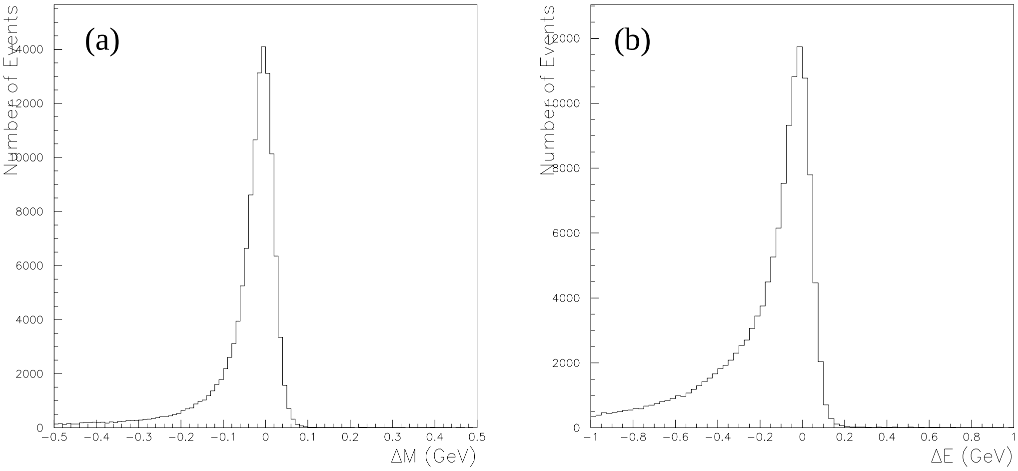

Figure 5.3: Distributions of (a) ΔM and (b) ΔE for the $e\gamma$-signal, showing the tail due to initial (ISR) and final state radiation (FSR), bremsstrahlung from the final state particles and measurement errors in the detector.

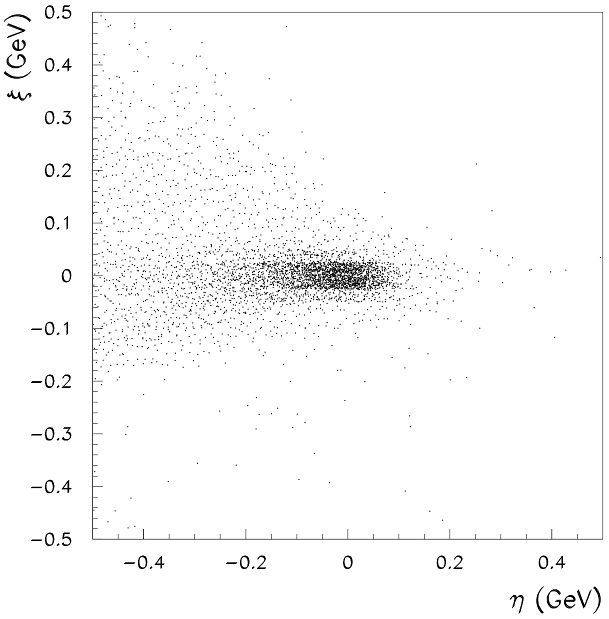

Figure 5.4: Distribution of the rotated η and ξ showing how a box would better fit the region where the signal is concentrated

$$\eta = \Delta\mathrm{M}\cos\theta + \Delta\mathrm{E}\sin\theta \quad \text{and} \quad \xi = -\Delta\mathrm{M}\sin\theta + \Delta\mathrm{E}\cos\theta. \tag{5.1}$$

with $\theta = 75°$. Now a rectangular shaped box better fits the concentration of $e\gamma$-signal events. The individual ξ-distribution for the $e\gamma$-signal is now more symmetric and approximates a Gaussian, while the contribution from the tail can still be seen in the individual η-distribution (Fig. 5.8).

On the two dimensional plane of η and ξ two regions are defined, an inner signal box ω_i and an outer sideband ω_o (Fig. 5.5). If the backgrounds are smooth and non-peaking throughout the region containing the sideband and the signal box, b can be estimated by extrapolating from the number of background events found in the sideband. The method for defining the exact size of the regions ω_o and the initial size of ω_i is as follows:

- The sideband ω_o must lie on a smooth non-peaking region of the individual η and ξ distributions for the data (Fig. 5.6), the regions are $-0.4 < \eta < 0.4$ and $-0.2 < \xi < 0.2$. As a cross-check the same distributions are shown for the combination of

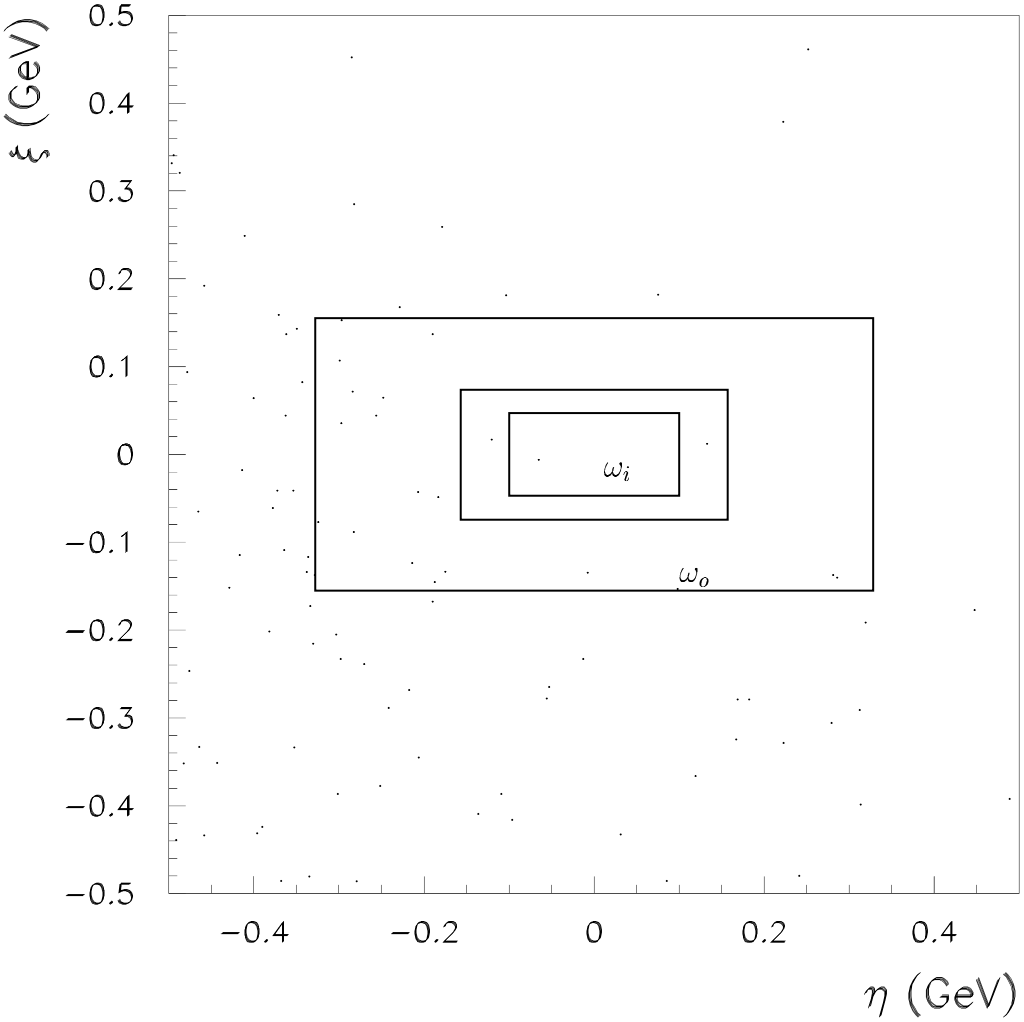

Figure 5.5: Distribution of η and ξ for the data control sample. The signal box ω_i and the sideband region ω_o are shown.

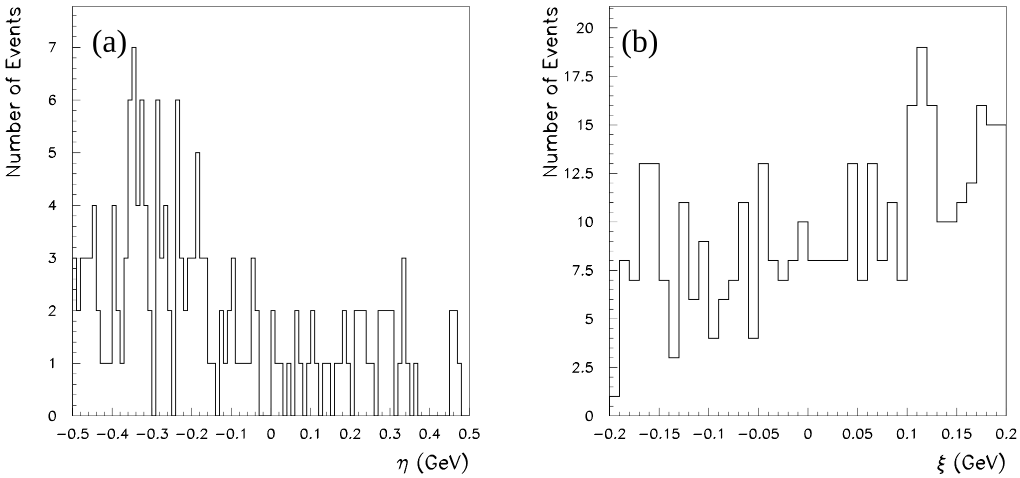

Figure 5.6: Distributions η and ξ for the data control sample.

the Bhabha control sample and a sample of simulated SM τ events (Fig. 5.7); these also exhibit similar smooth regions.

- The signal box ω_i is defined by fitting the individual η and ξ distributions for the simulated signal with a Gaussian function (Fig. 5.8); the mean and standard deviation for each fit is presented in Table 5.1; in order to centre ω_i and ω_o at the mean of the Gaussian functions the η, ξ-axes in Fig. 5.5 have been adjusted by the means of the fits; the dimensions of ω_i and ω_o are set in multiples n of the standard deviations σ_η, σ_ξ.

- The size of ω_i is optimised but it is not allowed to be larger than 6σ ($\pm 3\sigma$ the full width of the Gaussian) in either dimension.

- The sideband ω_o has an external and internal dimension, the size of the internal aperture must be large enough to accommodate ω_i; thus the size is set at 7σ ($\pm 3.5\sigma$) in both dimensions; the external dimensions are set at 14σ_η ($\pm 7\sigma_\eta$) and 11σ_ξ ($\pm 5.5\sigma_\xi$) respectively to remain in the smooth non-peaking regions of η and ξ.

At this stage the region ω_i has not been optimised. The optimisation is carried out by maximising the ratio $\epsilon/\sqrt{b}$. Estimating b is described in the next section.

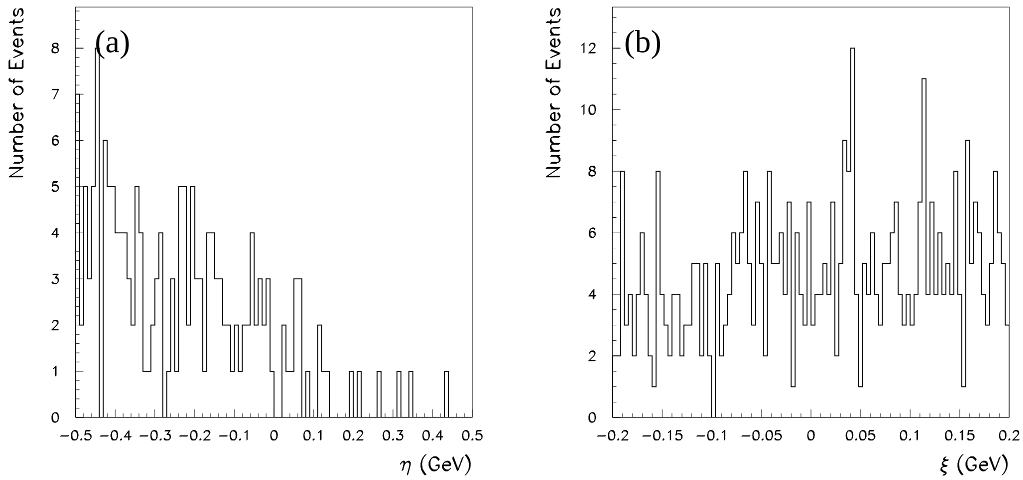

Figure 5.7: η and ξ-distributions for the combination of the sample of simulated SM τ events and Bhabha control sample.

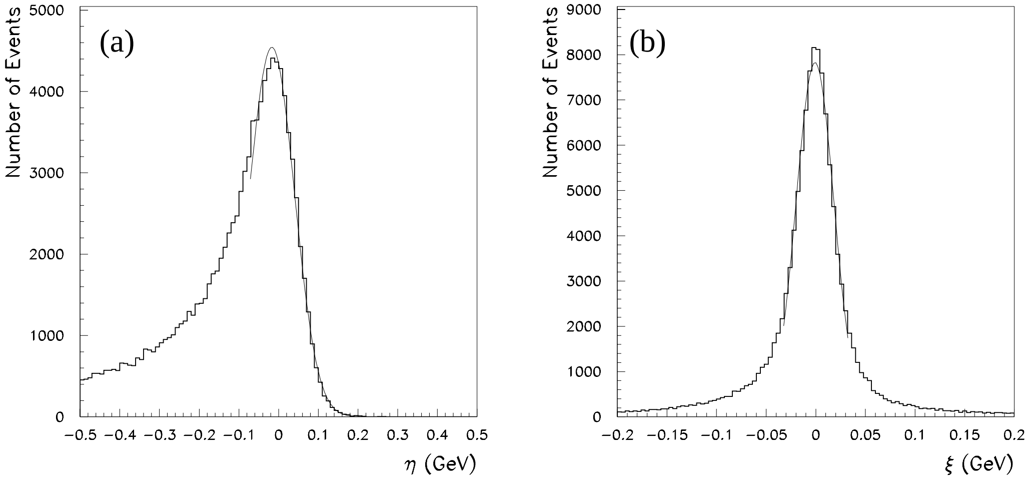

Figure 5.8: Distribution of (a) η and (b) ξ for the $e\gamma$-signal. The non-tail part of each distribution is fitted using a Gaussian function.

Table 5.1: The parameters obtained by fitting the non-radiative part of the η and ξ-distributions using a Gaussian function.

Parameters	mean (MeV)	standard deviation (MeV)
η	-17.3	57.1
ξ	-1.96	27.3

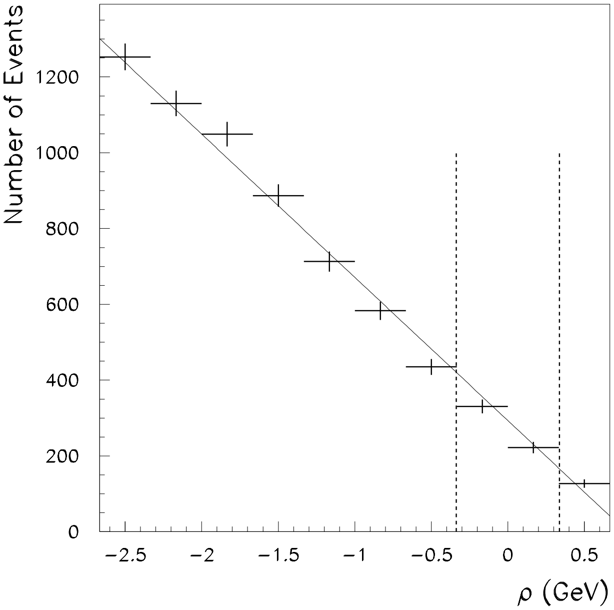

Figure 5.9: A distribution of ρ, where the dashed lines indicate the extreme corners of the signal box.

5.2 Method used to estimate the number of background events

In order to estimate the number of expected background events a function is fitted to the data. Initially the simplest shape is tried i.e. a plane. In this case it is assumed that η and ξ, across the sideband ω_o, follow a function of the form,

$$f_b(\eta, \xi; \vec{\theta}) = 1 + \theta_\eta \eta + \theta_\xi \xi. \tag{5.2}$$

This function is fitted to ω_o and the coefficients obtained from the fit are $\theta_\eta = -2.37 \pm 0.38$ and $\theta_\xi = -2.34 \pm 0.71$. To test whether the plane is appropriate the distribution of $\rho = \theta_\eta \eta + \theta_\xi \xi$, with θ_η and θ_ξ obtained from the fit is considered (Fig. 5.9). This distribution is modelled by a linear fit with χ^2 = 12 for 10 d.o.f. This gives reasonable agreement on both sides of the signal box and therefore conclude that it is sufficient.

The number of background events b in ω_i is therefore:

$$b = \nu_o \frac{\int_{\omega_i} f_b(\eta, \xi; \vec{\theta}) d\eta d\xi}{\int_{\omega_o} f_b(\eta, \xi; \vec{\theta}) d\eta d\xi}, \tag{5.3}$$

where ν_o is the expected number of events in ω_o. An estimate $\hat{b}$ for the number of background events b is:

$$\hat{b} = n_o \frac{\int_{\omega_i} f_b(\eta, \xi; \vec{\theta}) d\eta d\xi}{\int_{\omega_o} f_b(\eta, \xi; \vec{\theta}) d\eta d\xi} \tag{5.4}$$

where n_o is the observed number of events in ω_o and $\hat{\vec{\theta}}$ is the vector of estimated parameters ($\hat{\theta}_\eta, \hat{\theta}_\xi$) obtained from the fit.

The error on $\hat{b}$ is obtained using standard error propagation:

$$V[\hat{b}] = \left(\frac{\partial \hat{b}}{\partial n_o} \right)^2 V[n_o] + \sum_{i,j=\eta,\xi} \frac{\partial \hat{b}}{\partial \theta_i} \frac{\partial \hat{b}}{\partial \theta_j} \mathrm{cov}[\hat{\theta}_i \hat{\theta}_j] \tag{5.5}$$

$$\sigma_{\hat{b}} = \sqrt{V[\hat{b}]} \tag{5.6}$$

The error is determined numerically.

The next step is to optimise the size of the signal box and is described next.

5.3 Optimisation of the signal box

The signal box is determined by maximising the ratio of the signal efficiency ϵ to the square root of the expected number of background events b. The size of the box is expressed as a number of standard deviations, $n\ \sigma_\eta \times n\ \sigma_\xi$. The size of the signal box is varied in steps of 1σ in both dimensions (Fig. 5.10). The number of background events is evaluated using the full 124.4fb^{-1} of data. As a check b is also estimated using a combination of Bhabha control sample and the sample of simulated SM τ events (Fig. 5.11). Comparing the two distributions a maximum is estimated to be at $n = 3.5$ standard devi-

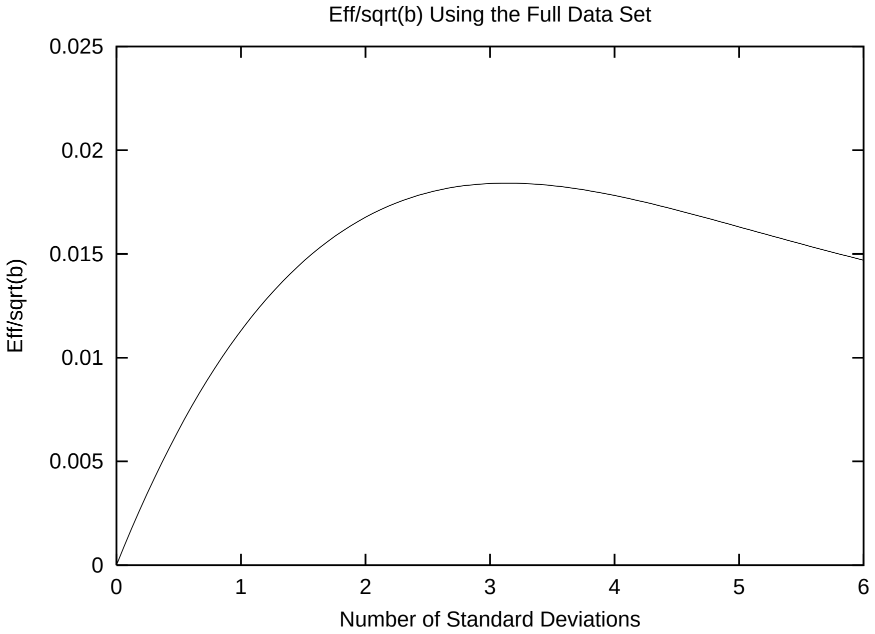

Figure 5.10: The ratio of the efficiency to the square root of the estimate of the number of background events using the 124.4fb^{-1} of data.

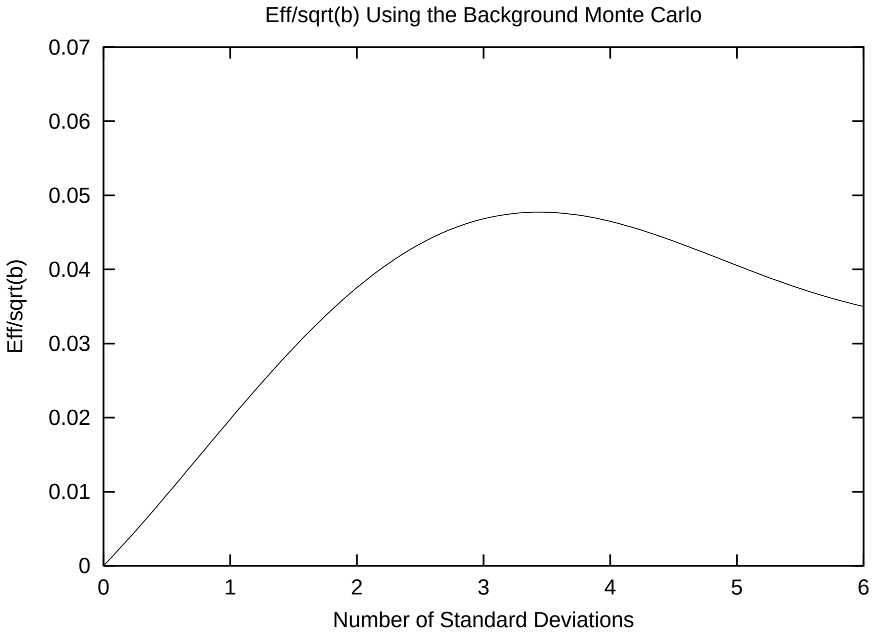

Figure 5.11: The ratio of the efficiency to the square root of the estimate of the number of background events using a combination of Bhabha control sample and sample of simulated SM τ events.

ations. For this size of the signal box the efficiency of selecting signal events is 5.8%.

5.4 Estimating b

Once the size of the sideband and signal box have been set then b can be determined. First b is evaluated for the 21.1 fb^{-1} data control sample and compared with the number actually observed in the signal box. Secondly as a cross-check on b the same method is applied to the combination of Bhabha control sample and the sample of simulated SM τ events . Lastly the procedure is applied to the full 124 fb^{-1} data set, whilst the signal box remains blind, to obtain the value of b used in calculating the final result.

The expected number of background events calculated for the data control sample (21.1 fb^{-1}) using the method described previously is 1.16 ± 0.2 (Fig. 5.5). This compares with the 1.0 event observed in the signal box.

The value of b calculated for the combination of SM τ-decays and Bhabha events that have been scaled to the luminosity of the data control sample is 2.1 ± 0.8 and is close to the scaled number of events, 1.2, found in the signal box for the same samples. These estimates are summarised in Table 5.2.

Table 5.2: Summary of the number of signal events and the estimated number of background events from the data control sample and the sample of simulated SM τ events plus the Bhabha control sample.

	Data control sample		Bhabha control sample + SM τ	
	Signal box	Sideband	Signal box	Sideband
Number of events	1.0	1.16±0.20	1.2	2.1±0.8

Once the estimate for the number of background events within the signal region has been checked and agrees with that found from the data control sample then a final estimate can be made using the full data set. This is given next.

5.4.1 Background estimate from full, blinded, data set

The full 124.4 fb^{-1} data set is then analysed to obtain the final estimate of the expected number of background events. The expected number of background events in the signal box, extrapolated from the sideband, is 8.27±0.67 (statistical error only) (Fig. 5.12). As a

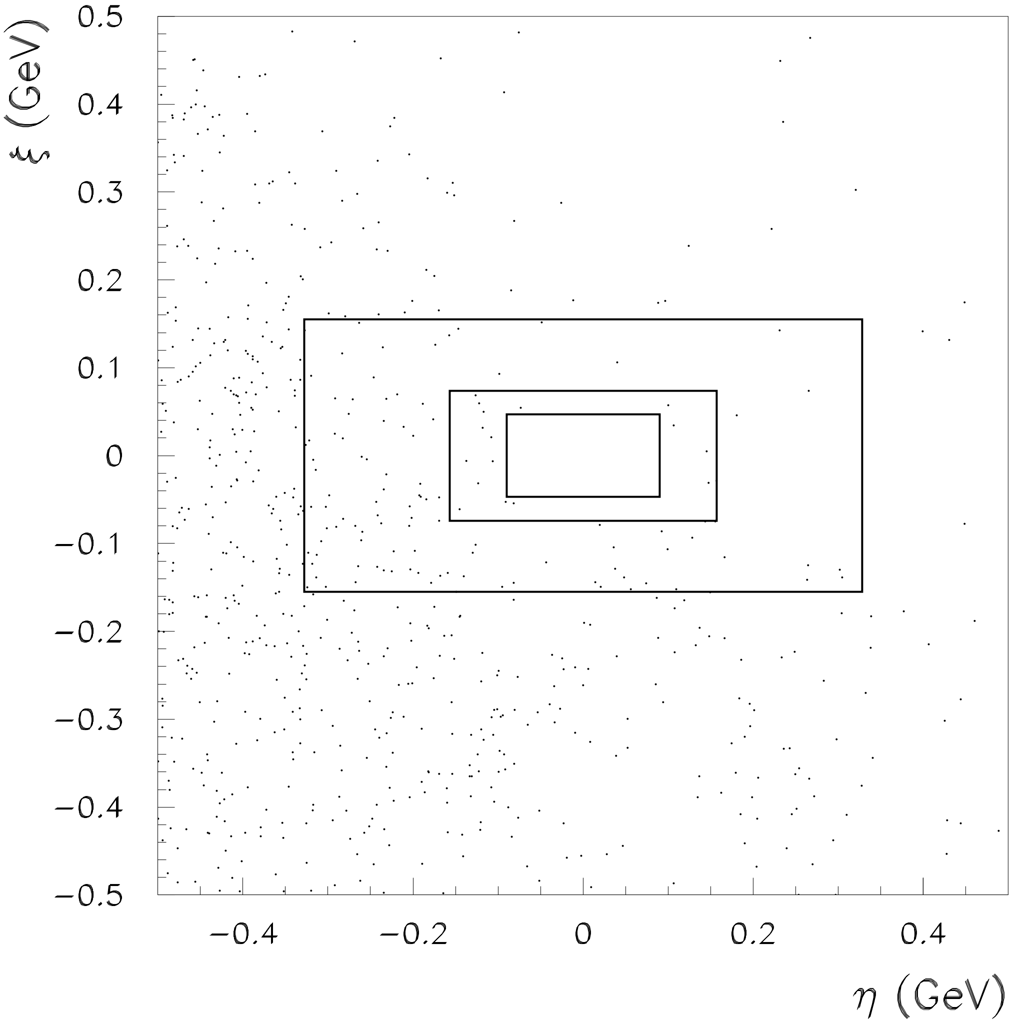

Figure 5.12: Distribution of the rotated η and ξ for 124 fb^{-1} of data. The signal box is "blinded" and the fit to the neighbouring region gives an estimated number of background events equal to 8.27.

check this estimate is compared with that found for the combined Bhabha control sample and SM τ events (luminosity scaled). Here $b = 12.41 \pm 4.72$ events estimated from the sideband and $b = 9.86$ events from the number of events found in the signal box.

The estimated number of background events from the full data set and the combination of the sample of simulated SM τ-events plus Bhabha control sample, scaled to the luminosity of the full data sample are summarised in Table 5.3.

Table 5.3: Summary of the estimated number of background events from the full data set and the sample of simulated SM τ events plus the Bhabha control sample.

	Data $124.4\,\text{fb}^{-1}$		Bhabha control sample + SM τ	
	Signal box	Sideband	Signal box	Sideband
Number of events	-	8.27±0.67	9.86	12.41±4.72

5.5 Systematic errors

The sources of systematic error [50] fall into two categories relating to uncertainties in the estimation of b and determination of the efficiency of detecting the signal. Since the data control sample is used to estimate the number of background events in the analysis and not samples of simulated background events, the only significant sources of systematic error that require estimation for b are: single photon selection, electron identification, luminosity, cross-section for the τ-pair production and the function used for the fit of the (η, ξ) plane. These are discussed individually and summarised in Table 5.4. Then the systematic error on the efficiency of detecting the signal is discussed.

5.5.1 Systematic errors on b

The criteria for the selection of neutrals is described in Section 4.6.2. A working group in the *BABAR* collaboration has studied the efficiency for selecting single photons and has assigned an error of 3.0% [51] which is taken as the systematic. This estimate is primarily related to distinguishing single photons from pi-zeros. As this uncertainty will have only a small influence on the final result a conservative estimate is used.

In Section 4.6.3 it is reported that the efficiency of the electron identification algorithm has a systematic error of 1.0% [49]. The determination of the luminosity is described in

Section 3.1 and an error of 1.2% is reported [52].

The generator used for producing the SM τ events is `KK2f` [44]. The systematic uncertainty is evaluated by summing in quadrature the errors on the individual branching fractions weighted by the relative fraction of the number of the events in a given channel with this decay mode. For the acceptance of the *BABAR* detector the cross-section is determined with an uncertainty of 2.2% and is assigned as a systematic error.

A further potential source of uncertainty in b stems from the hypothesis of a linear distribution for η and ξ. It is shown in section 5.2 that a plane is a good fit to the data therefore no extra systematic was assigned. Other functional forms were considered but the plane is found to adequate.

Table 5.4: Summary of the systematic errors on b for the single photon selection, electron identification and the determinations of the τ cross-section and luminosity.

Source	Error(%)
Single photon	3.0
Electron ID	1.0
cross-section	2.2
Luminosity	1.2
Total Error	4.03

The systematic errors on b from the photon selection, electron identification and the determinations of the τ cross-section and luminosity are summed in quadrature and the final systematic error on the estimation of the number of background events is 4.03%. The total number of background events expected in the 124.4fb^{-1} data sample is estimated to be 8.27±0.67(stat)±0.33(syst) (8.27±0.75).

5.5.2 Systematic errors on ϵ

There is an uncertainty in the efficiency of detecting the signal estimated from the sample of simulated signal events. In Chapter 4 cuts on the data for seven separate variables were introduced. In principle the result, be it a branching fraction or a limit, should not depend on the value of the boundaries of the cuts and comparisons between data and simulated events of the distributions of the respective variables ought to be in good agreement. If the comparisons show any differences then these can be used as a measure of the estimate of the systematic uncertainty.

Of the seven variables used for the cuts only the last three $cos\theta_{e\gamma}$, E_γ and N_γ will be used for the estimation of the systematic error. These three variables are used because the contribution from Bhabha events by this stage is small when compared with the number of standard model τ-decays, which is now the major source of background.

To illustrate how the systematic error is estimated take the cut on the variable $cos\theta_{e\gamma}$ as an example. Two distributions of this variable are generated, one for the data and the other for the simulated background events. These two distributions are generated after the cuts on the other six variables have been applied i.e. T, E_{miss}, $\cos\theta_{\mathrm{miss}}$, P_T, E_γ and N_γ. The two distributions are then compared and are presented in Fig. 5.13(a).

Distributions are then generated for E_γ in exactly the same way except the cuts are applied to the six variables T, E_{miss}, $\cos\theta_{\mathrm{miss}}$, P_T, $cos\theta_{e\gamma}$ and N_γ. These are presented in Fig. 5.13(b). Similarly distributions are generated for N_γ except the cuts are applied to the six variables T, E_{miss}, $\cos\theta_{\mathrm{miss}}$, P_T, $cos\theta_{e\gamma}$ and E_γ. These are presented in Fig. 5.13(c).

The systematic error is calculated by first finding the relative difference $\delta_i\,(i = 1,\,2,\,3)$ for each of the three variables being compared,

$$\delta_i = \frac{n_{s_i} - n_{d_i}}{n_{d_i}} \tag{5.7}$$

where n_s is the integral over the acceptance region of the sum of the samples of simulated events and n_d is the same integral for the data. The acceptance regions are $0.3 < cos\theta_{e\gamma} < 0.8,\ E_\gamma > 0.4\,\mathrm{GeV}$ and $N_\gamma = 1$, as specified in Chapter 4. The relative errors for each of the three variables and the values used in the calculations are given in Table 5.5.

The systematic uncertainty is estimated by summing the three individual relative errors δ_i,

$$\delta_{\mathrm{total}} = \sqrt{\sum \delta_i^2} \tag{5.8}$$

giving a value of 0.0431.

The next step in the analysis is to unblind the 124.4 fb^{-1} data sample and compare the

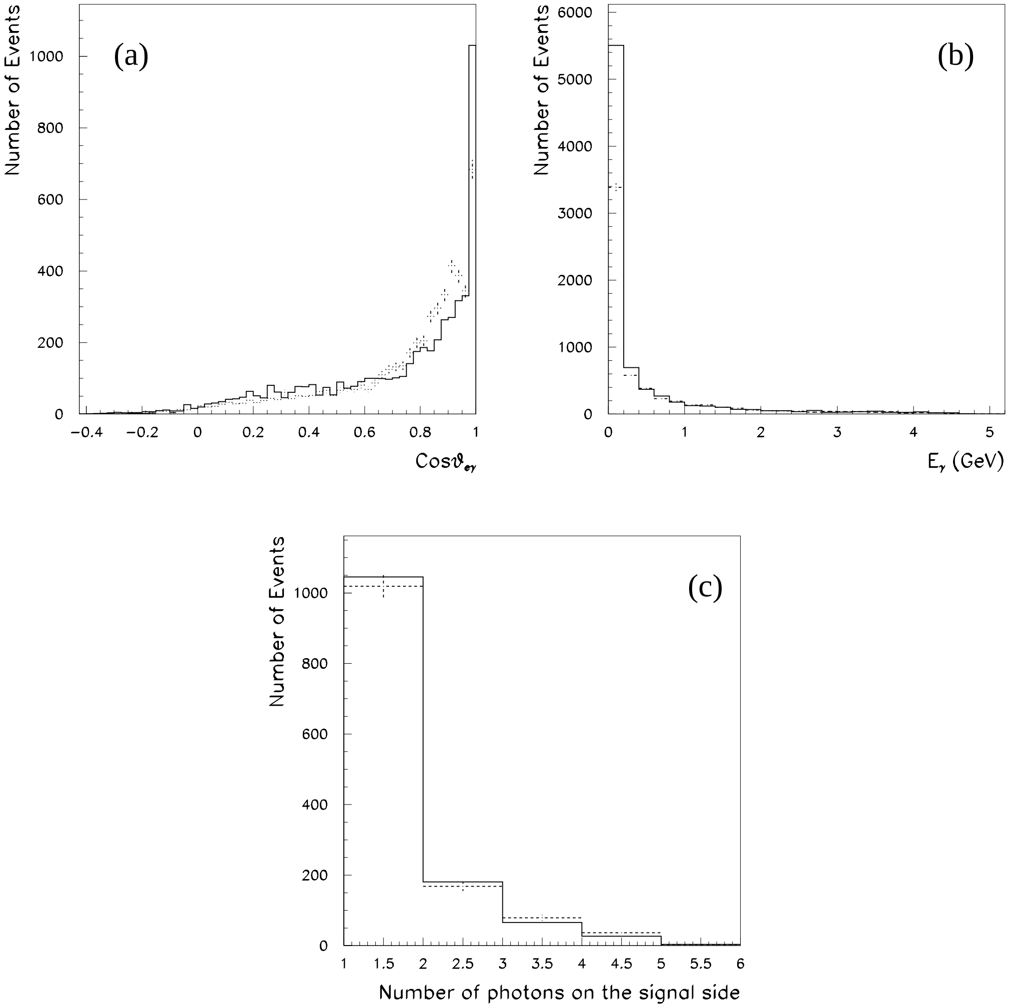

Figure 5.13: Distributions of (a) $cos\theta_{e\gamma}$, (b) E_γ, and (c) the number of photons on the signal side of the event N_γ. Each distribution has two parts; the data distribution is drawn with errors and is overlayed on a second distribution which is the sum of a mixture of samples of simulated events plus the Bhabha control sample (luminosity weighted).

Table 5.5: The table shows the values of the integrals, n_s and n_d, over the acceptance regions for the three variables $\cos(\theta_{e\gamma})$, E_γ and N_γ and their relative errors δ_i (equation 5.7). The samples have been luminosity weighted to the size of the data control sample (21.1fb^{-1}).

Variable	Acceptance region	n_{s_i}	n_{d_i}	δ_i
$\cos\theta_{e\gamma}$	0.3 - 0.8	5615	5493	0.0222
E_γ	$> 0.4\,\mathrm{GeV}$	1677	1659	0.011
N_γ	$= 1$	1055	1019	0.0353

number of events observed in the signal box with $\hat{b}$. This is presented in the next section.

5.6 Unblinded distribution for $\tau \to e\gamma$

Finally the signal box is unblinded and the resulting distribution (η, ξ) for the full 124.4 fb^{-1} data set is shown in Fig. 5.14. Five events are observed in the signal box compared with prediction of 8.27 background events. As there is no excess of events over the expected number of backgrounds there is no evidence for the decay mode $\tau \to e\gamma$. Therefore the branching ratio cannot be measured and thus an upper limit $\mathcal{B}_{\text{up}}$ is set. The method used to set the limit and its calculation is discussed in the next chapter.

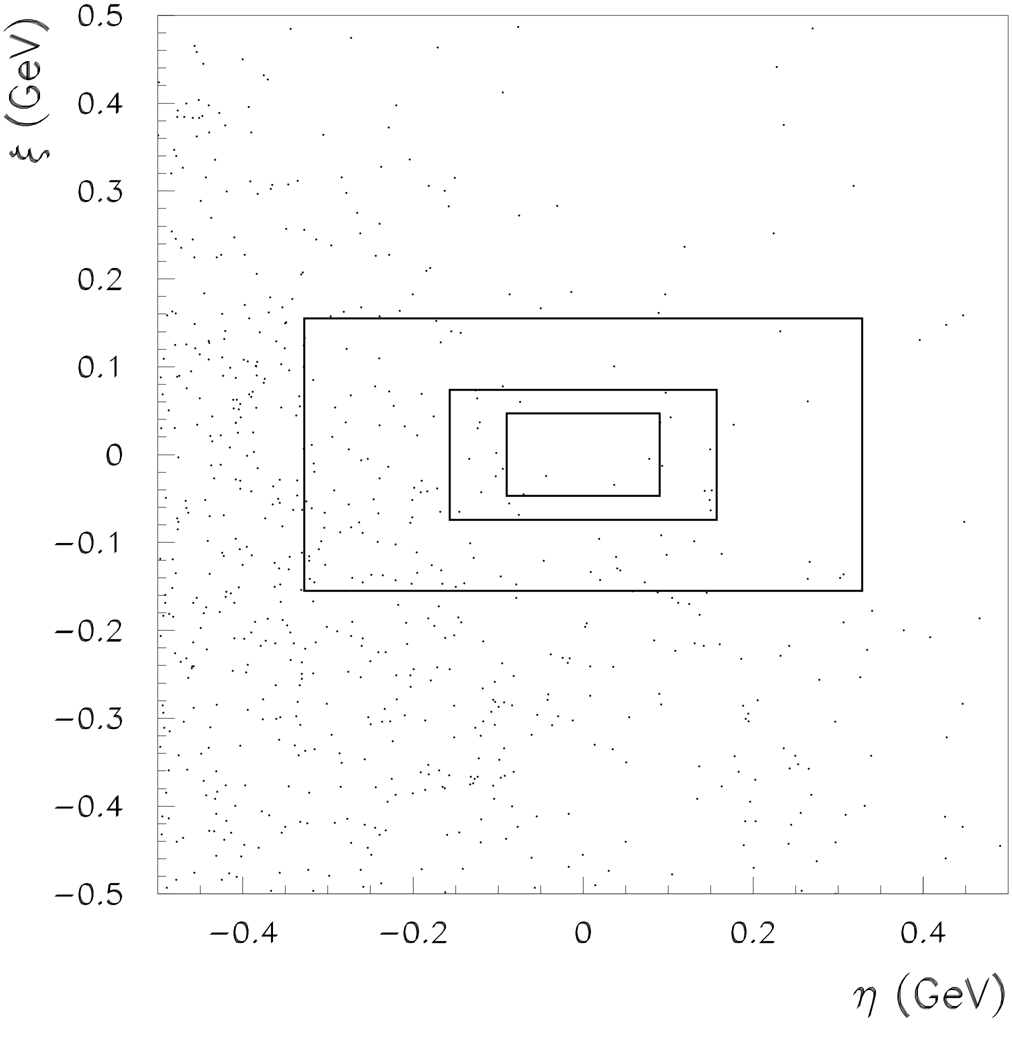

Figure 5.14: The unblinded distribution (η, ξ) for the full 124.4 fb^{-1} data set showing five events in the signal box.

Chapter 6

Setting the limit and conclusions

As there is no evidence for the decay mode $\tau \to e\gamma$ a 90% confidence level (CL) upper limit on its branching ratio is calculated. There is a debate about the method for setting limits and quoting confidence levels which, is illustrated by the number of workshops set up to discuss the issues [53–55]. Some of the methods proposed are discussed here followed by a description of the one adopted for this analysis. The limit set is compared to that previously published by the CLEO collaboration [3]. The BELLE collaboration have reported a preliminary limit that has yet to be published [56]. In conclusion the implications of not finding the decay $\tau \to e\gamma$ are discussed followed by suggestions of how to carry the analysis further.

6.1 Methods of setting upper limits on branching ratios

The upper limit for the branching ratio $\mathcal{B}_{\rm up}$ is related to $s_{\rm up}$ the upper limit on the expected number of signal events by the equation,

$$\mathcal{B}_{\rm up} = \frac{s_{\rm up}}{\epsilon N_\tau}. \tag{6.1}$$

Here ϵ is the efficiency of detecting the signal and N_τ is the number of τ-decays in the data set. The upper limit on the branching ratio is in effect a limit on s scaled by ϵN_τ; here ϵN_τ is referred to as the sensitivity $\mathcal{S}$.

The number of the events observed in the signal box n is assumed to be described by a Poisson probability distribution. The Poisson probability function is given by the formula,

$$P(n;\nu) = \frac{e^{-\nu}\nu^n}{n!}, \tag{6.2}$$

and has a mean $\langle n \rangle$ and standard deviation σ given by

$$\langle n \rangle = \nu, \quad \sigma = \sqrt{\nu}. \tag{6.3}$$

Now $n = n_s + n_b$ where n_s and n_b are the number of signal and background events respectively and are also Poisson variables. Thus the mean $\nu = s + b$ where s and b are the means of n_s and n_b respectively. Given n, we need to set a limit on s.

Calculating s_{up} will depend on whether b and $\mathcal{S}$ are known with certainty or if they have an error. Both of these situations are considered.

6.1.1 Upper limit without error on b and $\mathcal{S}$

The classical upper limit on s for a known number of background events b and sensitivity (without error) is the hypothetical value of s such that there is a probability of $1 - CL$ of observing $n \leqslant n_{\text{obs}}$ events, i.e.

$$1 - CL = P(n \leqslant n_{\text{obs}};\, s,\, b,\, \mathcal{S}). \tag{6.4}$$

Here $CL = 0.9$ (90% confidence level), n is the number of events in the signal box, n_{obs} is the number of events actually observed in the signal box. Eq. 6.4 is then solved to find s_{up}.

Another method of placing an upper limit on s is to use the liklihood function for the Poisson distributed n, i.e.

$$L(s) = \frac{(s+b)^n}{n!} e^{-(s+b)}. \tag{6.5}$$

The limit s_{up} is set where $\text{ln}L(s)$ has fallen from its maximum value by an amount dependent on the confidence level required, i.e.

$$\mathrm{ln}L(s) \geqslant \mathrm{ln}L_{\mathrm{max}} - \Delta\mathrm{ln}L. \tag{6.6}$$

For a 90% confidence level limit $\Delta\mathrm{ln}L = 1.355$ [7].

The liklihood function $L(n|s)$ can also be used in Bayes' theorem [57] to give the posterior probability for s given a number of observed events n,

$$p(s|n) = \frac{L(n|s)\pi_s(s)}{\int L(n|s')\pi_s(s')\,\mathrm{d}s} \tag{6.7}$$

where the prior probability $\pi_s(s)$ satisfies the conditions in Eq. 6.16.

The posterior probability $p(s|n)$ is then integrated over s for a confidence level CL,

$$\int_0^{s_{\mathrm{up}}} p(s|n)\,\mathrm{d}s = CL \tag{6.8}$$

This can be shown [58] to reduce to,

$$\frac{\exp(-s)\sum_{n=0}^{n=n_{\mathrm{obs}}} \frac{(b+s)^n}{n!}}{\sum_{n=0}^{n=n_{\mathrm{obs}}} \frac{b^n}{n!}} = 1 - CL, \tag{6.9}$$

which is solved for s. This is the upper limit s_{up} for a confidence level CL.

In contrast Feldman and Cousins [59] have devised a method which is a classical confidence interval construction but will also not give unphysical results for a small signal which had been the original motivation for the use of Bayesian intervals. In the Feldman and Cousins approach this is accomplished by modifying Neyman's original construction, the details of which can be found in reference [60].

If there is an error on b and $\mathcal{S}$ then these have to be taken into account when calculating s_{up} and this situation is discussed next.

6.1.2 Upper limit with errors on b and $\mathcal{S}$

If there is a systematic uncertainty in the signal efficiency ϵ or equivalently in the sensitivity factor $\mathcal{S}$, then this can be incorporated into the limit using a procedure proposed by Cousins and Highland [61]. If $\pi_{\mathcal{S}}(\mathcal{S})$ is the function of the estimate of the sensitivity $\mathcal{S}$, then equation 6.4 can be generalised to,

$$1 - CL = \int P(n \leqslant n_{\mathrm{obs}};\, s,\, b,\, \mathcal{S})\pi_{\mathcal{S}}(\mathcal{S})\,\mathrm{d}\mathcal{S}. \tag{6.10}$$

The function $\pi_{\mathcal{S}}(\mathcal{S})$ can be characterised by a Gaussian distribution with mean $\hat{\mathcal{S}}$ and error $\sigma_{\mathcal{S}}$, i.e.

$$\pi_{\mathcal{S}}(\mathcal{S}) = \frac{1}{\sqrt{2\pi}\hat{\mathcal{S}}} e^{(\mathcal{S}-\hat{\mathcal{S}})^2/2\sigma_{\mathcal{S}}^2}, \tag{6.11}$$

Similarly if the expected number of background events is uncertain and is also described by a Gaussian distribution, $\pi_b(b)$ then equation 6.10 becomes,

$$1 - CL = \int\int P(n \leqslant n_{\mathrm{obs}};\, s,\, b,\, \mathcal{S})\pi_{\mathcal{S}}(\mathcal{S})\pi_b(b)\,\mathrm{d}\mathcal{S}\,\mathrm{d}b. \tag{6.12}$$

Eq. 6.12 can be solved to find s_{up} using a method such as that of Barlow [62].

If the limit cannot be less than zero, which is the case for a branching ratio, then the general confidence interval can give unphysical results if the number of observed events is small. For example in Fig. 6.1 in the region around five observed events the classical confidence upper limit is negative. In this case a pseudo-likelihood function $L^{'}(\mathcal{B})$ [7] can be defined as,

$$L^{'}(s) = \int L(s,\, \mathcal{S},\, b)\pi_{\mathcal{S}}(\mathcal{S})\pi_b(b)\,\mathrm{d}\mathcal{S}\,\mathrm{db}. \tag{6.13}$$

The limit is set by using the same conditions as in Eq. 6.6.

Alternatively the likelihood function can be used directly in a Bayesian analysis with a uniform prior density [63]. Bayes theorem [57] which in terms of $s,\, b,\, \mathcal{S}$ and n is,

$$p(s,\, b,\, \mathcal{S}|n) = \frac{L(s,\, b,\, \mathcal{S})\pi_s(s)\pi_b(b)\pi_{\mathcal{S}}(\mathcal{S})}{\int L(s,\, b,\, \mathcal{S})\pi_s(s)\pi_b(b)\pi_{\mathcal{S}}(\mathcal{S})\,\mathrm{d}s\,\mathrm{d}b\,\mathrm{d}\mathcal{S}} \tag{6.14}$$

To find the pdf for s alone, we integrate over b and $\mathcal{S}$ which gives,

$$p(s|n) = \int p(s,\, b,\, \mathcal{S}|n)\,\mathrm{d}b\,\mathrm{d}\mathcal{S}. \tag{6.15}$$

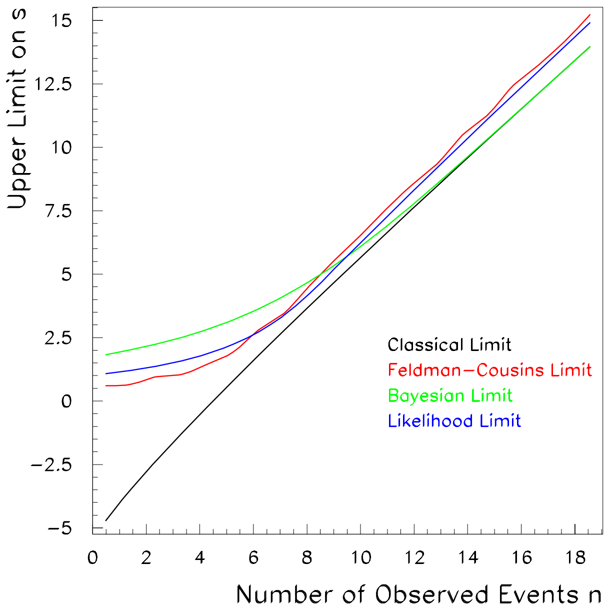

Figure 6.1: Upper limit on the number of signal events s_{up} for an observed number of events in the signal box in the range 0, 20 for the classical [57], Feldman-Cousins [59], Baysian [7] and likelihood [7] methods. All of the distributions assume an estimated number of background events equal to 8.27.

Here $p(s|n)$ is the probability of s given n, the integral in the denominator is the normalisation and $\pi_s(s)$ (the prior probability) is taken as flat to reflect the complete ignorance about s i.e.,

$$\pi_s(s) = \begin{cases} 1 & \text{if } s > 0, \\ 0 & \text{if } s \leqslant 0. \end{cases} \tag{6.16}$$

These various methods for calculating the upper limit on the number of signal events s_{up}, classical [57], Feldman-Cousins, Bayesian method with a flat prior [7] and likelihood [7], are illustrated in (Fig. 6.1). The limits are calculated for the range 0 to 20 for the number of events n observed in the signal box. The estimated number of background events for the full 124.4 fb^{-1} is $b = 8.27$. Barlow's numerical method due [62] based on the approach of Cousins and Highland [61] is used in this analysis to calculate s_{up}. This method is described next and the final limit is calculated.

The method uses a Monte Carlo (MC) technique [57] and begins by selecting a trial value for $\mathcal{B}_{\mathrm{up}}$. The distributions of the expected number of background events b and the sensitivity $\mathcal{S}$ are assumed to be Gaussian with uncertainties σ_b and $\sigma_{\mathcal{S}}$ respectively as previously with the likelihood method. Toy MC samples are produced and in each sample $\mathcal{S}$ and b are varied with their values being taken from their respective Gaussian distribution. Each sample defines the mean of a Poisson distribution from which a number of events n is generated. The branching fraction is varied iteratively for a large ensemble of the toy MC samples until the mean probability for $n \leqslant n_{\mathrm{obs}}$ is 0.1. This defines the 90% CL upper bound on $\mathcal{B}$.

This method gives essentially a conventional classical limit as their are no prior assumptions about $\mathcal{B}$ as in the Bayesian method. On the other hand the systematic errors on b and $\mathcal{S}$ are often subject to a belief on the part of the experimenter, which is a strictly Bayesian viewpoint. Perhaps the best description of the method is that it is a mixture of both classical and Bayesian ideas.

Using one million toy MC events, $b = 8.27$, $\sigma_b = 0.98$, $\mathcal{S} = 12.48 \times 10^6$ and $\sigma_{\mathcal{S}} = 0.627 \times 10^6$ the resulting limit calculated using the Barlow method is 9.3×10^{-8} at 90% C.L. The sensitivity is the product of the signal efficiency ϵ and the number of τ-events used and the uncertainty on $\mathcal{S}$ is calculated by summing, in quadrature, their systematic errors. This limit is significantly lower than the previously published limits and is discussed in the next section.

6.2 Discussion of the result

The upper limit that has been set for $\mathcal{B}(\tau \to e\gamma)$ is two orders of magnitude lower than the previously published result by the CLEO collaboration [3]. The BELLE collaboration have also reported a preliminary limit of 3.6×10^{-7} [56]. These results are summarised in Table 6.1.

The result presented here is consistent with the Standard Model without any modifications by other theories such as supersymmetry. It is four orders of magnitude larger than the upper limit on the branching ratio for the mode $\mu \to e\gamma$. The result constrains the parameter space relating to models that predict branching ratios for LFV processes higher than those calculated for the SM with neutrino oscillations. Taking the Ellis model (Chapter 2) for the supersymmetric seesaw matrix as an example, the branching ratios

Table 6.1: The limits set by the CLEO, BELLE and the preliminary result from the *BABAR* collaborations for the $\mathcal{B}(\tau \to e\gamma)$. The signal efficiency, luminosity, number of observed events n_{obs} and the expected number of background events b are also compared.

Collaboration	Signal efficiency(%)	Luminosity (fb^{-1})	n_{obs}	b	$\mathcal{B}_{\text{up}}$ (10^{-8})
CLEO	10.1	4.64	0	2.0	270
BELLE	6.5	87.1	-	20	38
This analysis (preliminary)	5.8	124.4	5	8.27	9.3

calculated for $\tau \to e\gamma$ depended on the assumed value of $\tan\beta$. It was shown that for a $\tan\beta = 30$ a branching ratio of $O(10^{-4})$ is predicted and for $\tan\beta = 10$ a branching ratio of $O(10^{-5})$. Thus the result reported here disallows some region of the spectrum of values for $\tan\beta$. As stated in section 2.3 the branching fraction scales as $tan^2\beta$. Therefore a limit of $O(10^{-7})$ to (10^{-8}) would correspondingly constrain $\tan\beta$ to values of 1 and 0.316 respectively.

The analysis can be improved in an obvious way by enlarging the data set which is now possible at *BABAR*. In the year from the autumn of 2003 to the summer of 2004 more data has been taken (run four) and the total available on-peak data is 205fb^{-1} with 16fb^{-1} off-peak. Using this amount of data would further reduce the limit by a factor of 0.5, assuming no evidence for signal was discovered and a similar signal efficiency and expected number of background events. The projected data set by the end of the *BABAR* experiment in its present form is $1.5\,ab^{-1}$. Therefore the expected limit assuming similar efficiencies would a be an order of magnitude lower. Upgrading the current *BABAR* experiment to a “Super B-Factory” is being considered and its final data set would be of the order of $30\,ab^{-1}$. This would lower the limit by two orders of magnitude from that set in this thesis.

The efficiency for detecting the $e\gamma$-signal is lower than that obtained by the CLEO collaboration even though their detector is very similar to the *BABAR* detector. There are two reasons for this, one is that the τ-filter described in section 4.6.4 is not optimal for finding τ-events with a 1-1 topology and the second is that the EMC in the CLEO detector has a better resolution. As a result of the work done in this analysis the collaboration has decided to re-write the τ-filter to make it more efficient. It is not clear why the EMC in the CLEO detector is superior and is still a subject of discussion.

Another improvement is to use the beam-energy substituted mass [64] when calculating the invariant mass of the $e\gamma$-system. In this analysis the $e\gamma$-system has to have an invariant mass equal to the τ-mass and a total energy equal to the beam energy. If the event has not been correctly reconstructed because the momentum of the electron or the energy of the photon are not accurately measured then this potential signal event could be lost, thus reducing the efficiency of detecting the signal. These events would become part of the tail in the invariant mass distribution (Fig. 5.6). This type of event could be recovered by compensating for the inaccurate measurement knowing that it had to have been produced at the energy of the beam. This is the essence of the beam-energy substituted mass. Applying this same idea to the events already in the signal box (Fig. 5.5) could also concentrate them more closely reducing the size of the signal box thus reducing the number of background events appearing in the box.

In Section 4.2 the point was made that the threshold energy for the production of τ-pairs is $3.53\,\mathrm{GeV}$ and therefore some of the pairs will not be produced at the beam energy of 10.58 GeV in the centre of mass due to initial state radiation (ISR). Therefore these events would also appear in the tail of the invariant mass distribution. If it were possible to measure the energy and momentum of the the photon produced in the ISR process and adding it to the electron then the event would move from the tail to the signal region of the distribution. The photon is often produced close to the beam and can go undetected. Thus it maybe implausible to compensate for loss of energy and momentum of the electron.

Is there a way of distinguishing between the two types of event, one that has been inaccurately measured and one that has not been produced at the beam energy? Can the photon produced in the ISR process be identified? These are open questions and would require separate studies, but they could improve the signal efficiency and reduce the backgrounds.

In conclusion the search of approximately 111 million τ-pairs for the lepton flavour violating decay $\tau \to e\gamma$ has been unsuccessful. An upper limit on the branching ratio for the decay process has been set and is lower than any limit reported in previously published analyses. The limit can be used to constrain a number of models such as supersymmetry. Improvements to the analysis have been presented and should make future searches more efficient.

.1 appendix A

The Author has made a significant contribution to the day to day running of the *BABAR* experiment and an account of this work is given below. As the experiment operates 24 hours a day, seven days a week, the Commissioner is on call continuously throughout the run making it a difficult and stressful service task. The Commissioner is at the fore-front of all the major problems and issues that arise with the EMC and is responsible for its smooth running so as to maximise data quality and minimise downtime resulting in the loss of data. The duties of the commissioner include:

- being the representative for the EMC at the daily operations meeting where representatives from all of the sub-systems report any problems or work that has been carried out in the previous 24 hours; running the weekly EMC operations meeting where all of the people who work on the EMC report problems and work carried out in the previous week and discuss work and plans for the future. There is also a weekly meeting of the EMC steering group where the Commissioner has to report to the senior management of the experiment;

- It is not always possible to gain immediate access to the detector to affect a repair if a problem is diagnosed with one of the channels; in this case the affected channel is isolated using software until the detector can be entered and repaired; typically the type of repair is the replacement of electronics boards;

- All power supplies and some of the readout electronics are external to the detector and faults can be easily dealt with by replacing the affected board in between periods of data taking;

- Re-calibrating the calorimeter when its configuration has been changed due to problems or repairs;

- A chiller system is used to be maintain the EMC at a constant temperature of $20 \pm 1^{\circ}\,C$ in all weather conditions. There are three separate chiller systems plus two backup systems; one system cools the electronics and two others cool the barrel and endcap of the calorimeter. The electronics chiller uses water as the refrigerant and the other two use fluorinert; the levels of all the refrigerants have to be checked periodically and topped up as necessary; the detector is also inspected to look for any possible leaks;

- Data quality is monitored by inspecting distributions that are generated automatically during each data taking period of approximately 1 - 2 hours; this has to be done at least daily or more often where possible and a data quality flag is set for each period.

The level of responsibility coupled with being continuously on call made this service task extremely difficult but enjoyable.

Bibliography

[1] M. L. Brooks *et al.*, Phys. Rev. Lett. **83**, 1521 (1999).

[2] M. Ahmed *et al.*, Phys. Rev. **D65**, 112002 (2002).

[3] CLEO Collaboration, Search for the neutrinoless τ decays: $\tau \to e\gamma$ and $\tau \to \mu\gamma$, 1996, CLNS 96/1428.

[4] Stanford linear Accelerator Center, Url: http://www.slac.stanford.edu/, 2004, hep-ph/0402035.

[5] An asymmetric B factory based on PEP, The conceptual design report for PEP-II (1991).

[6] PEP-II: An Asymmetric B Factory. Conceptual Design Report (1993).

[7] Particle Data Group, S. Eidelman *et al.*, Phys. Lett. **B592**, 1 (2004).

[8] N. Cabibbo, Phys. Rev. Lett. **10**, 531 (1963).

[9] M. Kobayashi and T. Maskawa, Prog. Theor. Phys. **49**, 652 (1973).

[10] J. Bahcall, *Neutrino Astrophysics* (Cambridge University Press, 1989).

[11] SNO, Q. R. Ahmad *et al.*, Phys. Rev. Lett **89**, 011302 (2002), nucl-ex/0204009.

[12] Super Kamiokande, Y. Fukuda *et al.*, Phys. Rev. Lett. **81**, 1562 (1998).

[13] Z. Maki *et al.*, Prog. Theor. Phys. **28**, 870 (1962).

[14] Y. N. M.C. Gonzalez-Garcia, hep-ph/0202058.

[15] R. Mohapatra, (2004), hep-ph/0402035.

[16] K. Eguchi *et al.*, Phys. Rev. Lett. **90**, 021802 (2003).

[17] M. Ahn *et al.*, Phys. Rev. Lett. **90**, 041801 (2003).

[18] M. Apollonio *et al.*, Phys. Lett. **B 420**, 397 (1998).

[19] F. Boehm *et al.*, Phys. Rev. Lett. **84**, 3764 (2000).

[20] Z. Xing, Int. J. Mod. Phys. **A 19**, 1 (2004).

[21] M. Gell-Mann *et al.*, in *Supergravity*, edited by P. van Niewwenhuizen and D. Freedman, North Holland, Amsterdam, 1979.

[22] T. Yanagida, Proceedings of the Workshop on the Unified Theory and Baryon number if the Universe, edited by O. Sawada and A. Sugamoto , 95 (KEK, 1979).

[23] A. Smirnov, Phys. Rev. D **48, 7**, 3264 (1993).

[24] Y. Kuno and Y. Okada, KEK preprint **99-69** (1999), hep-ph/9909265.

[25] F. Halzen and A. Martin, Quarks and Leptons; John Wiley and sons (1984).

[26] S. Petcov, Sov. J. Nucl. Phys. **25**, 340 (1977).

[27] S. Bilenky *et al.*, Phys. lett. **B67**, 309 (1977).

[28] T. Cheng and L.-F. Li, Phys. Rev. **D22**, 2860 (1980).

[29] M. Drees, An Introduction to Supersymmetry (1996), hep-ph/9611409.

[30] B. Lee and R. Shrock, Phys. Rev. D **16**, 1444 (1977).

[31] J. Bjorken *et al.*, Phys. Rev. D **48, 7**, 1474 (1993).

[32] R. Mohapatra and G. Senjanovic, Phys. Rev. D **23**, 165 (1981).

[33] R. Barbieri and L. J. Hall, Phys. Letts. **B338**, 212 (1994).

[34] R. Barbieri *et al.*, Nucl. Phys. **B445**, 219 (1995).

[35] J. Hisano *et al.*, Phys. Letts. **B391**, 341 (1997), hep-ph/0004061.

[36] F. Borzumati and A. Masiero, Phys. Rev. Lett. **57**, 961 (1986).

[37] J. Ellis *et al.*, CERN-TH/2002-126 , hep-ph/0206110.

[38] J. Hisano *et al.*, Phys. Letts. **B357**, 579 (1995).

[39] BaBar, B. Aubert *et al.*, Nucl. Instrum. Meth. **A479**, 1 (2002).

[40] D. Boutigny *et al.*, SLAC Report No. SLAC-R-0457, 1995 (unpublished).

[41] R. Seitz, Describing energy deposit in CsI crystals, 1996, SLAC-BABAR-NOTE-294.

[42] A. Ryd *et al.*, Trigger and filter documentation, BAD #194, Version 1, (*BABAR* internal analysis document), 2002.

[43] P. F. Harrison and H. R. Quinn, editors, *The BABAR physics book: Physics at an asymmetric B factory* (, 1997), Papers from workshop on physics at an asymmetric B factory (*BABAR* collaboration meeting), Rome, Italy, 11-14 Nov 1996, Princeton, NJ, 17-20 Mar 1997, Orsay, France, 16-19 Jun 1997 and Pasadena, CA, 22-24 Sep 1997.

[44] B. F. L. Ward, S. Jadach, and Z. Was, Nucl. Phys. Proc. Suppl. **116**, 73 (2003), hep-ph/0211132.

[45] P. Harrison, ’Blind Analyses’ in the Proceedings of the conference on the Advanced Statistical Techniques in Particle Physics; Editors, M. Whalley, L. Lyons and J. Stirling; IPPP/02/39 , 278 (2002).

[46] E. Barberio and Z. Was, Comput. Phys. Commun. **79**, 291 (1994).

[47] GEANT4 Collaboration, S. Agostinelli *et al.*, Nucl. Instrum. Meth. **A506**, 250 (2003).

[48] E. Varnes, Report of the tracking efficiency task force, BAD #324, Version 2, (*BABAR* internal analysis document), 2002.

[49] Electron identification analysis working group: Cut-based electron identification, BAD #90, Version 5, (*BABAR* internal analysis document), 2001.

[50] R. Barlow, ’Systematic Errors: Facts and Fictions’ in the Proceedings of the conference on the Advanced Techniques in Particle Physics; Editors, M. Whalley and L. Lyons; IPPP/02/39 , 134 (2002).

[51] M. T. Allen *et al.*, BAD #870, Version 3 (*BABAR* internal analysis document) (2004).

[52] O. Igonkina, A search for lepton flavor violating decays $\tau^- \to l^- l^+ l^-$, BAD #722, Version 11, (*BABAR* internal analysis document), s upporting document. BAD #761, Version 15, (*BABAR* internal analysis document), s ubmitted to PRL, 2003.

[53] Proceedings of the Workshop on Confidence Limits, CERN, Geneva, Switzerland 17-18 January 2000; Editors, F. James and L. Lyons; IPPP/02/39. CERN yellow report 2000-005. .

[54] Proceedings of the 2nd Workshop on Confidence Limits,FERMILAB, Chicago, 2000; http://conference.fnal.gov/c12k/. .

[55] Proceedings of the Conference on the Advanced Statistical Techniques in Particle Physics; Editors, M. Whalley, L. Lyons and J. Stirling; Durham, England 2002; IPPP/02/39 .

[56] K. Abe, ’Search for LFV decays at BELLE’ talk given at ICHEP04 (2004).

[57] G. Cowan, *Statistical Data Analysis*, Second ed. (Oxford University Press, Oxford UK, 1998).

[58] Particle Data Group, K. Hagiwara *et al.*, Phys. Rev. **D66**, 010001 (2002).

[59] G. J. Feldman and R. D. Cousins, Phys. Rev. **D57**, 3873 (1998).

[60] J. Neyman, Philos. Trans. R. Soc.; London **A236**, 333 (1937).

[61] R. D. Cousins and V. L. Highland, Nucl. Instrum. Meth. **A320**, 331 (1992).

[62] R. Barlow, Comput. Phys. Comm. **149**, 97 (2002).

[63] O. Helene, Nucl. Instrum **Methods 212**, 319 (1983).

[64] W. T. Ford, Choice of Kinematic Variables in B Meson Reconstruction-Take 3; BAD #53, Version 5 (*BABAR* internal analysis document) (2000).